Ab initio modelling of materials relevant to the nuclear fuel cycle

Nathaniel Gjoderum-Symons

School of Chemical and Process Engineering

University of Leeds

Submitted in accordance with the requirements for the degree of Doctor of Philosophy

March 12, 2019

The candidate confirms that the work submitted is his own and that appropriate credit has been given where reference has been made to the work of others.

Acknowledgements

Firstly, I would like to thank both my supervisors Dr Andrew Scott and Dr Robert Hammond, for their assistance and guidance throughout the course of my PhD studies.

Also, I would like to thank Trevor Hardcastle for his patience and willingness to help with any questions at whatever hour. Furthermore, thanks to Mike, James, Rob, Thoko, and Mo for providing me with interesting discussions and good laughs over the past few years.

I would also like to thank all my family and in particular my parents for their unconditional support, and for keeping me grounded throughout my work.

Finally, I would like to thank Louise, for always being there for me, through the highs and the lows, and for the cakes and coffees. Your help has been immeasurable, I couldn't have done it without you, thank you.

Abstract

Large amounts of highly active nuclear waste in the UK is currently under temporary storage in Highly Active Storage Tanks (HASTs) at Sellafield. Before it can be safely transported into long-term storage, there are some serious considerations that require thorough investigation. Barium-strontium nitrate crystals ($Ba_xSr_{1-x}(NO_3)_2$) can form in the waste sludge and settle at the bottom of the HASTs. These crystals may lead to corrosion hotspots and subsequent nuclear waste leakages. As such, a thorough investigation into the fundamental properties of this material is pertinent. Whilst there have been some experimental studies into this material, theoretical methods may offer a more in-depth, as well as practical, way to study such properties at an atomic level. This thesis therefore aimed to use *ab initio* computational methods to investigate the fundamental properties of the barium-strontium nitrate complex, including defects and thermodynamic properties. Furthermore, it aimed to develop a new force field of interatomic potentials.

Ab initio DFT calculations were performed to calculate the structural and elastic properties for ($Ba(NO_3)_2$, $Sr(NO_3)_2$, and $Ca(NO_3)_2$), using different functionals and methodologies. Benchmark calculations were also performed, which demonstrated the accuracy and precision of these methods in comparison to existing experimental data. The mechanical and thermodynamic properties of $Ba_xSr_{1-x}(NO_3)_2$ were also calculated along with point defects and lattice parameters, with

good agreement with the literature. Finally, using the previous calculations, a force field interatomic potential was created.

These studies demonstrate the ability of DFT to produce reliable results that are consistent with experimental data. This body of work therefore provides strong and rigorous foundations for which future work can be conducted to provide vital information relating to the safety of transporting nuclear waste into long-term storage in the UK.

Contents

List of Figures

List of Tables

Nomenclature

Acronyms

nn	nearest neighbour
BFGS	Broyden-Fletcher-Goldfarb-Shanno (geometry optimisation algorithm)
EOS	equation of state
ES	energy-strain
FCC	face centred cubic
GGA	generalised gradient approximation
GULP	General Utility Lattice Program
HAL	highly active liquor
HALES	Highly Active Liquor Evaporation and Storage
HAST	Highly Active Storage Tank
HLW	high-level waste
ICSD	Inorganic Crystal Structure Database
ILW	intermediate-level waste
KS	Kohn-Sham
LDA	local density approximation
LLW	low-level waste
MD	molecular dynamics
PBE	Perdew-Burke-Ernzerhof (parametrisation of GGA)
POCO	post-operational clean-out
PUREX	plutonium uranium redox extraction

SCF	self-consistent field
SS	stress-strain
TBP	tributyl phosphate
teU	tonnes equivalent uranium
THORP	Thermal Oxide Reprocessing Plant
WVP	Waste Vitrification Plant
ZM	zirconium molybdate

Symbols

α	polarisability	
ΔG	Gibbs free energy	eV
ΔH	mixing energy	eV
ΔS	mixing entropy	eV
ϵ	strain	
ϵ_0	permittivity of free space	
ϵ_F	Fermi level	
ϵ_v	valence-band maximum	
$\hat{H}$	Hamiltonian operator	
$\hat{T}$	kinetic energy operator	
$\hat{V}$	potential energy operator	
$\hbar$	reduced Planck's constant	
μ	chemical potential	eV
Ω	interaction parameter	
ϕ	torsion angle	
Ψ	many-body wavefunction	
ψ	many-electron wavefunction	
ρ	ionic radius	
σ	stress	
θ_0	equilibrium bond angle	

a_0	lattice constant	Å
B	bulk modulus	GPa
C_{Gk}	complex Fourier coefficient	
C_{mn}	elastic constant	GPa
E	total system energy	
e	charge of electron	
E_{coh}	cohesive energy	eV
E_{cut}	plane wave cutoff energy	
E_f	formation energy	eV
F	sum of squares	
f_{calc}	calculated quantity	
f_{obs}	observed quantity	
k	harmonic force constant	$\mathrm{eV\,Å^{-2}}$
k_2	spring constant	
k_4	spring constant	
k_b	bond-bending constant	
k_B	Boltzmann constant	$\mathrm{eV\,K^{-1}}$
k_s	bond-stretching constant	
k_t	torsion force constant	
M	mass of nuclei	
m_e	mass of electron	
$n(\mathbf{r})$	total electron density	
$n_0(\mathbf{r})$	ground state total electron density	
P	pressure	GPa
q	defect charge state	
q	partial atomic charge	
R	position of nuclei	
r	position of electron	
r_0	equilibrium bond length	

r_{ij}	distance between i and j	
T	absolute temperature	K
V	volume	m^3
V_{KS}	Kohn-Sham potential	
w	weighting factor	
x	molar fraction	
Y	shell charge	
Z	charge of nuclei	
$\mathbf{G}$	reciprocal lattice vector	
$\mathbf{k}$	wave vector	
$\mathbf{L}$	lattice vector	
A	area	m^2
F	force	N

Chapter 1

Introduction

1.1 Setting the scene

Currently, there are fifteen operational nuclear reactors in the UK, and several reactors at various stages of decommissioning. Sellafield is the nuclear site (in Cumbria) where decommissioning of spent nuclear waste is performed, which involves reprocessing, treatment, storage, and disposal of waste products. Although Sellafield currently stores highly active liquor (HAL) (the liquor resulting from the reprocessing procedure) in Highly Active Storage Tanks (HASTs), these are only a temporary storage solution. Eventually the HAL will need to be transported into a more suitable facility for long-term storage.

There are many issues that can arise with long-term storage of HAL, which require thorough investigation before transportation should be attempted. One such problem is the formation of a barium-strontium nitrate crystal in the waste sludge. This nitrate complex can settle within the HASTs and subsequently lead to corrosion hotspots and nuclear waste leakages. Therefore, before transportation to long-term storage can be attempted, a rigorous understanding of the fundamental properties of barium-strontium nitrate is needed, to ensure the HAL can be handled safely and appropriately.

1.2 Material investigation methods

There are many different ways to investigate a material and there are many different phenomena governing the characteristics. Before the recent development in computational techniques and power, experimental methods lead the way with observational science. With the development of computational methods over the last half-century, particularly in the last 20 years, computational power and computational methods have advanced dramatically. This has paved the way for a whole host of new methodologies and scientific possibilities.

Experimental studies have previously been performed on $Ba_xSr_{1-x}(NO_3)_2$, reporting signs of phase mixing at certain concentrations, and the likelihood of a miscibility gap. They discovered that single phase mixed crystals form within the range of $x < 0.3$ and $x > 0.6$. Furthermore, they have investigated the properties of co-precipitation and solubility of $Ba_xSr_{1-x}(NO_3)_2$. However, no *ab initio* techniques have been performed on divalent nitrates with particular reference to high level waste decommissioning. Density Functional Theory (DFT) could be an advantageous tool for investigating the fundamental properties of these nitrates, given its ability for a high degree of control over the material's form (compared to experimental work where crystals are likely to have imperfections). Furthermore, if DFT can accurately calculate the basic properties of materials and be shown to be consistent with experimental results, it can then be used to make predictions about systems, or environments, that are not feasible or safe to test experimentally.

In this body of work, *ab initio* DFT methods are used to investigate the characteristics of isomorphous and isostructural divalent metal nitrates, including barium-strontium nitrate. This will provide insight into the fundamental properties of this material and will subsequently be used to develop parameters to generate an interatomic potential for barium-strontium nitrates. This work will provide a strong foundation for further research to build upon, which is

necessary to help develop solutions for the issues relevant to HAL storage and post-operation clean out of nuclear waste in general.

1.3 Thesis aims

This chapter has briefly outlined the context for which this work was conducted and the nature of the problem with nuclear waste management. It has also briefly discussed the methods that have previously been used to investigate the material relevant to nuclear waste (barium-strontium nitrate) and outlined the relevance of using *ab initio* methods. Given this, this thesis has the following aims:

1. To synthesize existing experimental research that has investigated the properties of barium and strontium nitrate
2. To investigate the fundamental properties of barium and strontium nitrate using computational methods
3. To determine the reliability of computational methods through comparison to existing experimental results
4. To investigate cationic substitutional point defects within barium nitrate
5. To investigate the structural and thermodynamic properties of the mixed barium-strontium nitrate complex
6. To use the above findings to develop a new force field of interatomic potentials.

1.4 Thesis overview

Prior to addressing the specific aims of this thesis, a full background of the nuclear industry in the UK and the nuclear fuel cycle is given in Chapter 2, to provide

context to this body of work. To address the aims of this thesis, a literature review was conducted, as well as various calculations, which are reported in each subsequent chapter.

Chapter 3 relates to aim 1. A review of the experimental literature was conducted as well as a review of DFT and molecular dynamic calculations that have been performed on similar materials. This review highlighted the absence of research on divalent metal nitrates using *ab initio* methods, and highlighted the limitations of using experimental methods to understand the properties of these materials. This review informed the subsequent chapters.

Chapter 4 provides an overview of the computational theory behind the methods used throughout this body of work as well as a discussion of the limitations and approximations.

Chapter 5 relates to aims 2 and 3. The structural and elastic properties for $Ba(NO_3)_2$ and $Sr(NO_3)_2$ were calculated through *ab initio* methods, with in depth study of different functionals and also different methodologies for calculating the elastic properties. Benchmark calculations were also performed to develop a greater understanding of the accuracy and precision of the methods and compare the reliability and quality of the different results. Results from this chapter informed calculations in the following chapter.

Chapter 6 relates to aims 4 and 5. DFT point defect calculations were performed using the finite size scaling method. Furthermore, DFT solid solution calculations were undertaken, calculating Gibbs free energy of $Ba_xSr_{1-x}(NO_3)_2$ to determined the $T-x$ phase diagram.

Chapter 7 relates to aim 6. Using the *ab initio* results in this thesis, a interatomic force field was fitted with the inclusion of a shell model potential to make it more suitable for defect, and mixed phase, calculations. Suggestions for further improvements are discussed as well.

Chapter 8 contains the final discussion, which synthesises the findings from all of the calculations in the previous chapters to provide an overview of the

reliability of using density functional theory with regards to the properties of $Ba(NO_3)_2$ and $Sr(NO_3)_2$. This chapter discusses what the implications of these findings are and suggests further work that could be performed using the results.

Chapter 2

Scientific and technological background

2.1 Introduction

This chapter aims to present an overview of the scientific and technological background of this project. A brief overview of the nuclear fuel cycle is given, including a summary of nuclear fuel reprocessing. A detailed description of high level waste treatment in the UK is also given, along with a look into the challenges and solutions present.

2.2 The nuclear fuel cycle

An overview of the nuclear fuel cycle can be found in figure 2.1. The fuel cycle consists of two distinct phases. The first phase, known as the *front end*, starts at mining the fuel, through refining, conversion and enrichment, to creation of fuel pins and finally power generation in the nuclear reactors. The second phase, known as the *back end*, covers the processes applied to spent fuel, which undergoes reprocessing to extract and recover as much fuel as possible to reuse for further

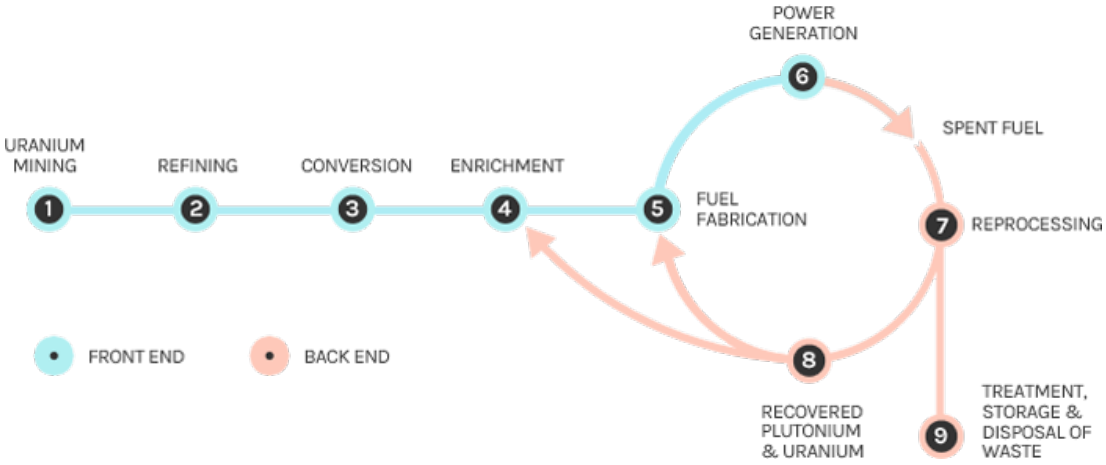

Figure 2.1: A schematic diagram of the nuclear fuel cycle (taken from [1]).

power generation, and the treatment, storage, and disposal of the nuclear waste.

In the UK in 1956, the first commercial nuclear power station was connected to the grid. Since then, there have been 51 commercial reactors built across 12 different sites. Currently, there are 15 operational nuclear reactors (generating approximately 21 % of the UK's electricity).

2.3 Reprocessing of spent nuclear fuel

Decommissioning of spent nuclear waste is performed at the Sellafield nuclear site in Cumbria, which was commissioned in 1956. Sellafield is the main site in the UK for dealing with nuclear waste and reprocessing, and it also deals with a large range of operations in which one of the main challenges is fully dealing with legacy waste from generation 1 reactors. Radioactive waste is typically categorised three ways; low-level waste (LLW), intermediate-level waste (ILW), and high-level waste (HLW), in which spent nuclear fuel is classed as HLW. The majority of ILW and HLW in UK is transported to Sellafield for treatment.

Sellafield also houses several nuclear reactors that are at various stages of decommissioning. Sellafield houses several departments such as the Thermal Oxide Reprocessing Plant (THORP), the Sellafield MOX Plant, the Highly Active

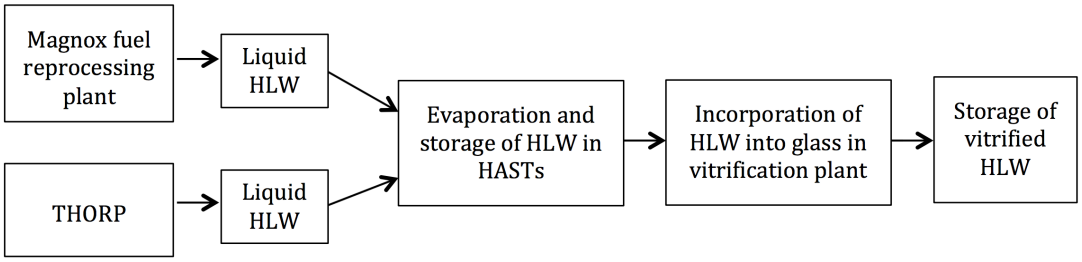

Figure 2.2: Liquid high-level waste (HLW) production and management at Sellafield [4].

Liquor Evaporation and Storage department (HALES), and the Waste Vitrification Plant (WVP).

2.4 HALES overview

The HALES facility accounts for more than 90 % of the on-site radioactivity at Sellafield [2] and broadly consists of two areas: storage and evaporation. The storage element comprises of a number of High Activity Storage Tanks (HAST) divided into *old side* (essentially quiescent) and *new side* (in active operations) [3]. HALES supports both the THORP and Magnox reprocessing operations by receiving their highly active liquid waste streams, known as raffinate, into buffer storage. The full procedure can be seen in figure 2.2.

Reprocessing is a chemical operation which is used to separate useful fuel for recycling from nuclear waste. Most spent nuclear fuel undergoes reprocessing to recover uranium and plutonium. The standard chemical method used today is known is PUREX (Plutonium Uranium Redox Extraction). During the initial stages, the nuclear fuel is chopped up and then dissolved in nitric acid (NO_3), removing the solids by filtration, and extracting the uranium and plutonium ions as $UO_2(NO_3)_2 \cdot 2\,TBP$ (tributyl phosphate) or similar complexes, respectively. The plutonium and uranium are separated through treatment with a kerosene

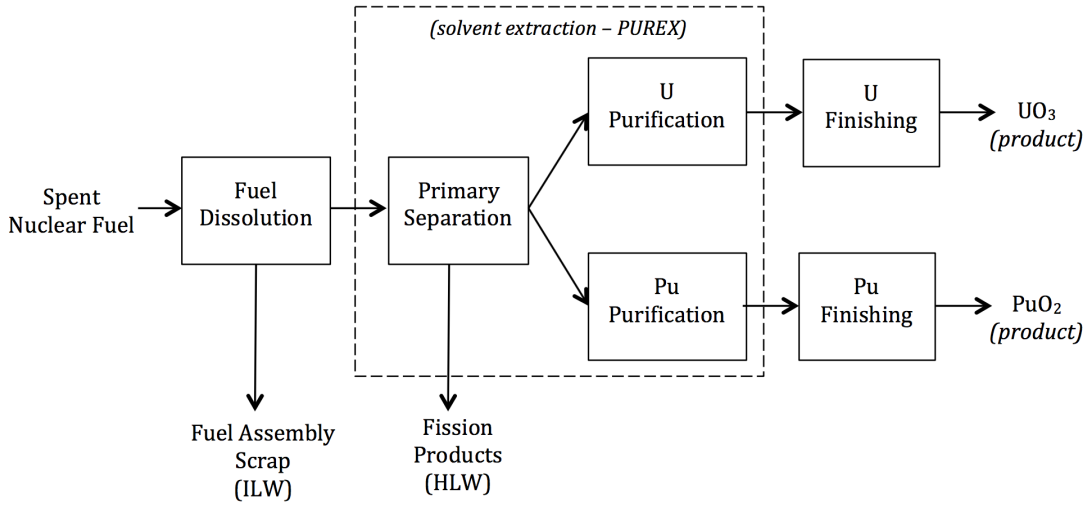

Figure 2.3: Spent nuclear fuel reprocessing procedure.

solution which converts plutonium to the +3 oxidation state and then passes into the aqueous state. The uranium is "back-extracted" into nitric acid so it can be extracted from the kerosene solution. Figure 2.3 shows the basic reprocessing procedure.

The raffinates contain fission products and waste actinides from the spent fuel. Following dissolution, the raffinates are transferred to evaporators in which they undergo a volume reduction of $30-60$ times through the distillation process (i.e. boiling up the liquor), the resultant concentrated liquor is known as Highly Active Liquor (HAL). The HAL is transferred into Highly Active Storage Tanks (HASTs), for temporary storage, prior to being transferred to the Waste Vitrification Plant for final immobilisation and storage [5]. During the vitrification process, the molten glass is poured into stainless steel containers ready for long term storage in a passive immobile safe form [3].

Sellafield has been storing HAL for more than 40 years and at the peak of operations there were 21 HASTs, with approximately $100\,\mathrm{m}^3$ per day throughput. See figure 2.4 for an image of the inside of a HAST under construction. On average, batch evaporator liquor contains 40–180 tonnes equivalent uranium (teU) and usually requires 5 weeks for the full evaporation process. The only legacy

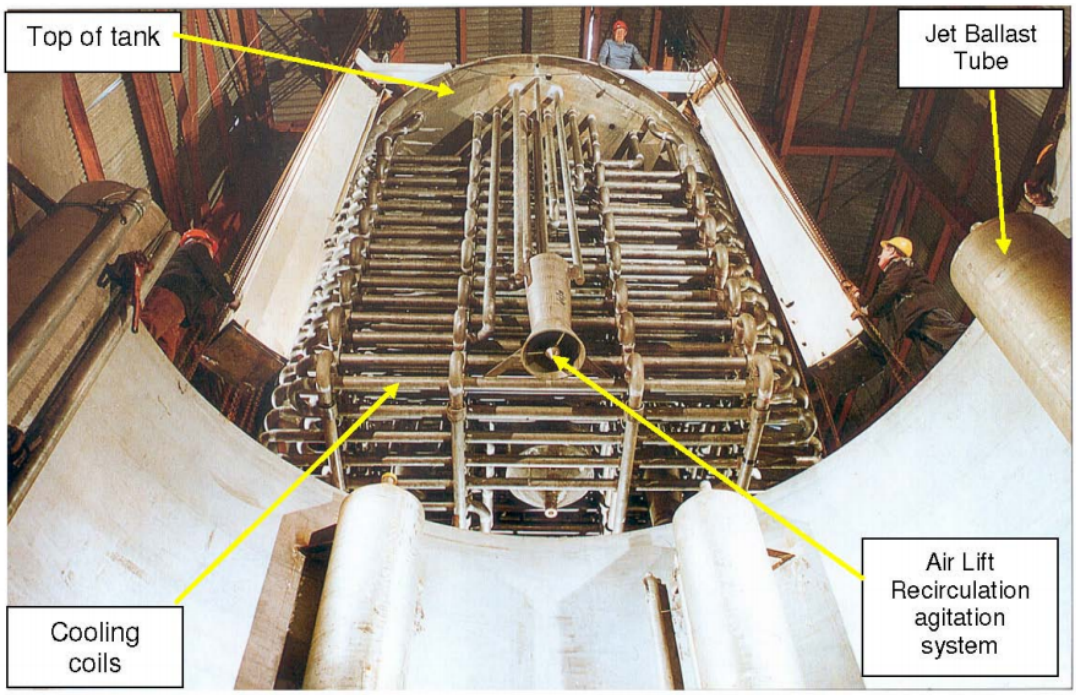

Figure 2.4: A HAST under construction (taken from [6]).

HAL left is now the 'Butex' HAL, which presents less risk in storage than recently produced HAL. Vitrification was originally scheduled for 2012, but instead oxide fuel derived from HAL was vitrified as it was considered more hazardous [3].

2.4.1 HASTs overview

Crystallization of decay products

Altogether, the HAL typically has $100\,g_{(metal)}/l$, with an activity of the order of $2 \times 10^{10}\,Bq\,ml^{-1}$ and a radioactive decay power output of approximately $5\,kW\,m^{-3}$ [5]. HAL is highly exothermic and therefore constant cooling and temperature monitoring is required. If there is sufficient heat generation in a HAST its contents could eventually boil which could lead to a significant release of radioactivity. At present Sellafield calculates that the contents of four HASTs has sufficient heat generation to enable boiling to occur [3].

During the dissolution stage, the fission products barium and strontium interact with HNO_3, leading to the formation of nitrates. These nitrates crystallise during the evaporation stage and in strongly acidic solutions, barium nitrate can co-precipitate with strontium nitrate to form a barium-strontium complex. The complex is dense and can settle at the bottom of the HASTs. Due to the highly active nature of strontium-90, this may lead to issues such as corrosion hotspots, which may subsequently lead to leakages. Previously, waterside corrosion has created pinholes in a number of cooling coils and small amounts of high level liquid waste escaped into the cooling system [6].

To combat sedimentation, the HASTs are equipped with airlifts and jet ballasts. The airlifts are used to keep the solids in suspension, whereas the jet ballasts are used to re-suspend any settling. However, there is still major concern about the effectiveness of these implements since it is difficult to replicate the HAL for testing or to measure any change within the HASTs.

Cooling is achieved by cooling jackets, as well as several internal, horizontal and vertical, cooling coils. The cooling coils circulate water, which removes heat via a cooling tower, using the flow rate to control the liquor temperature. The temperature is maintained between the lower crystallisation temperature and the upper operational limit requirements. In practice, a working limit is implemented for the liquor temperature to provide a margin of safety between operation temperature and maximum permitted temperatures [7].

Due to the highly radioactive nature of the nuclear waste, and therefore the requirement for safe, closed-circuit, treatment, there are a limited number of measurement methods and experimental techniques that can be used to provide insight into the characteristics and properties of the hazardous materials within the HASTs. This is one reason why computational methods have been adopted.

Other materials

The formation of zirconium molybdate (ZM) [$ZrMo_2O_7(OH)_2 \cdot 2\,H_2O$] from caesium phosphomolybdate, is another issue for the operators of the HASTs. ZM has a density of $3.4\,kg\,l^{-1}$ and similarly to the nitrate complex it settles rapidly. ZM has a much lower activity than strontium and therefore its decay heat is not considered an issue for HAL processing. However, ZM crystallises in a cubic morphology and can settle in a dense bed, which can cause issues with re-suspension. This additional settling can further aid the settling and formation of hotspots caused by strontium. ZM can also cause serious issues during post-operational clean-out (POCO), and therefore it is important to understand the properties in order to safely work with the waste [8]. However, this is beyond the scope of this thesis.

2.5 Post operation clean out

Ultimately, the HAL will need to be transferred out of the HASTs and treated for final storage. There are a number of issues that need to be addressed before it is possible to do so, such as the possible crystallisation of decay products and formation of corrosion hot spots, as previously mentioned.

It is currently proposed that the transfer of HAL will be carried out by repeated cycles of adding volumes of nitric acid or another reagent, agitation using installed systems, then discharging part of the HAST content (the effluent being termed as “flushings”). Initial flushings will be slightly diluted HAL, becoming more dilute as the HAST is washed out. This will steadily reduce the amount of HAL within the HASTs. It is expected that the wash-out process will recover ZM and unconverted caesium phosphomolybdate [9]. The flushings will subsequently be concentrated in an evaporator prior to vitrification.

In addition to crystallisation of decay products and formation of hotspots,

there is also concern around pipe blockages. The presence of large quantities of solids within the POCO flushings could cause issues during mobilisation and transfer to the vitrification plant. Therefore, before the POCO can commence, a thorough understanding of the issues is needed, to ensure safe management and storage of the nuclear waste.

2.6 Conclusions

In this chapter an overview of the nuclear fuel cycle, as well as nuclear fuel reprocessing and treatment of high-level waste has been given. Further detail of the current circumstance and obstacles to overcome within the HALES and HASTs have also been discussed, with particular focus on crystallisation of nuclear decay products and the potential threat they cause.

In general, there is a limited amount of specific research that has been performed on the solids that relates to the issues that are present at Sellafield. However, with the advancement of computational modelling techniques in recent years, *ab initio* and molecular dynamics calculations could be used to determine valuable information about the properties and characteristics of the solids within the HASTs. This will provide vital insight for the maintenance of the HASTs as well as influencing important POCO decisions, ensuring safe handling and treatment of the nuclear waste. These methods will be discussed in the subsequent chapters.

Although the issues highlighted in this chapter are radiation based, the fundamental properties behind the relevant materials need to be understood before specific radioactive effects can be considered. As such, the work carried out in this thesis focussed on the fundamental properties of the divalent metal nitrates, in which inclusion of the highly active strontium-90 atom, and other radioactive properties, are beyond the scope of this work.

Chapter 3

Literature review

3.1 Introduction

This chapter will review the experimental and computational studies that have been performed on divalent metal nitrates and specifically $Ba_xSr_{1-x}(NO_3)_2$. It will outline the research that is relevant to the industrial issues discussed in the previous chapter, as well as give a general understanding of the literature to date. Furthermore, it will describe experimental data that will inform calculations performed in the subsequent chapters.

It will be split into two main subsections;

1. Literature covering materials of interest ($Ba(NO_3)_2$, $Sr(NO_3)_2$, and $Ba_xSr_{1-x}(NO_3)_2$).

2. Literature covering computational work which shows how theoretical modelling can be of use to help with the HALES problem.

Table 3.1: Experimental lattice constants for barium nitrate ([a] Ref. [10] (room temperature), [b] Ref. [11], [c] Ref. [12], [d] Ref. [13], [e] Ref. [14] (room temperature), [f] Ref. [15]).

Space group	Lattice constant (Å)	Temp. (K)	Radiation	Sample type	R-value	ICSD code
$Pa3$	8.1184(2)	293	X-ray	single crystal	0.024	35495[a]
$P2_13$	8.126		neutron	single crystal	0.07	34902[b]
$Pa3$	8.126		X-ray	powder		52353[c]
$Pa3$	8.13		X-ray	powder		56087[d]
$Pa3$	8.11021(7)	293	neutron	powder	0.0659	95594[e]
$Pa3$	8.126		neutron	powder		109281[f]

3.2 Experimental studies

3.2.1 Pure nitrates

Many experimental studies have looked into calculating the structure and lattice parameters of $Ba(NO_3)_2$ and $Sr(NO_3)_2$. A summary of their work can be seen in tables 3.1 and 3.2. Whilst the neutron methods are arguably higher quality than X-ray studies, it is evident that they produce comparable results for both powder and single crystal samples of $Sr(NO_3)_2$ and of $Ba(NO_3)_2$, with regards to their lattice constants.

The elastic constants for both $Ba(NO_3)_2$ and $Sr(NO_3)_2$ have also been studied experimentally. See figures 3.1 and 3.2 for graphs of the elastic constants as a function of temperature. These graphs show that as temperature increases, the elastic constants decrease, and that between 100 and 300 K the relationship is almost linear.

3.2.2 Barium-strontium complex morphology

Large crystals of barium and strontium nitrate, (sizes greater than 60 mm × 60 mm × 70 mm) have been successfully grown via the temperature cooling method [18]. See figure 3.3 for a photograph of the crystals. Both crystals had the same

Table 3.2: Experimental lattice constants for strontium nitrate ([a] Ref. [10] (room temperature), [b] Ref. [16], [c] Ref. [12], [d] Ref. [13]).

Space group	Lattice constant (Å)	Temp. (K)	Radiation	Sample type	R-value	ICSD code
$Pa3$	7.7813(2)	Room	neutron	single crystal	0.024	35494[a]
$Pa3$	7.822(1)	173	X-ray	single crystal	0.0292	59391[b]
$Pa3$	7.826	Room	X-ray	powder		52532[c]
$Pa3$	7.83	Room	X-ray	powder		56088[d]

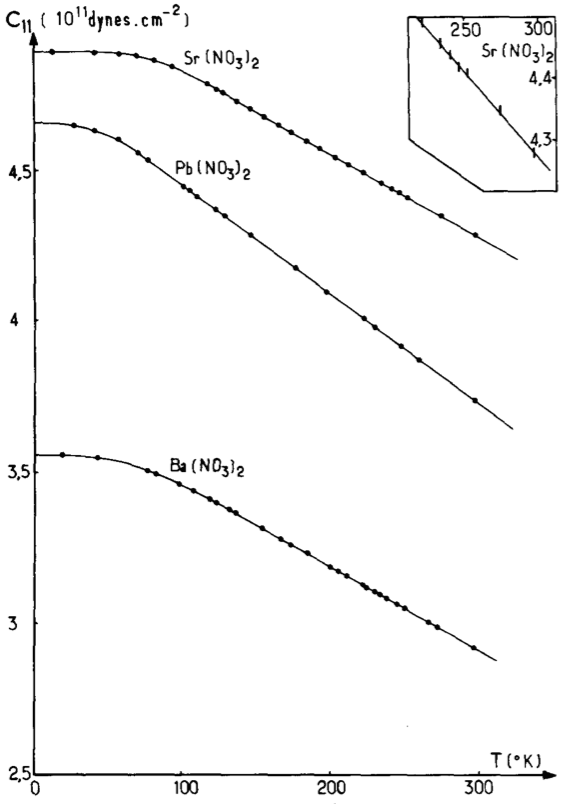

Figure 3.1: Temperature dependence of C_{11} for strontium, lead, and barium nitrates. Insert shows the amount of experimental error [17].

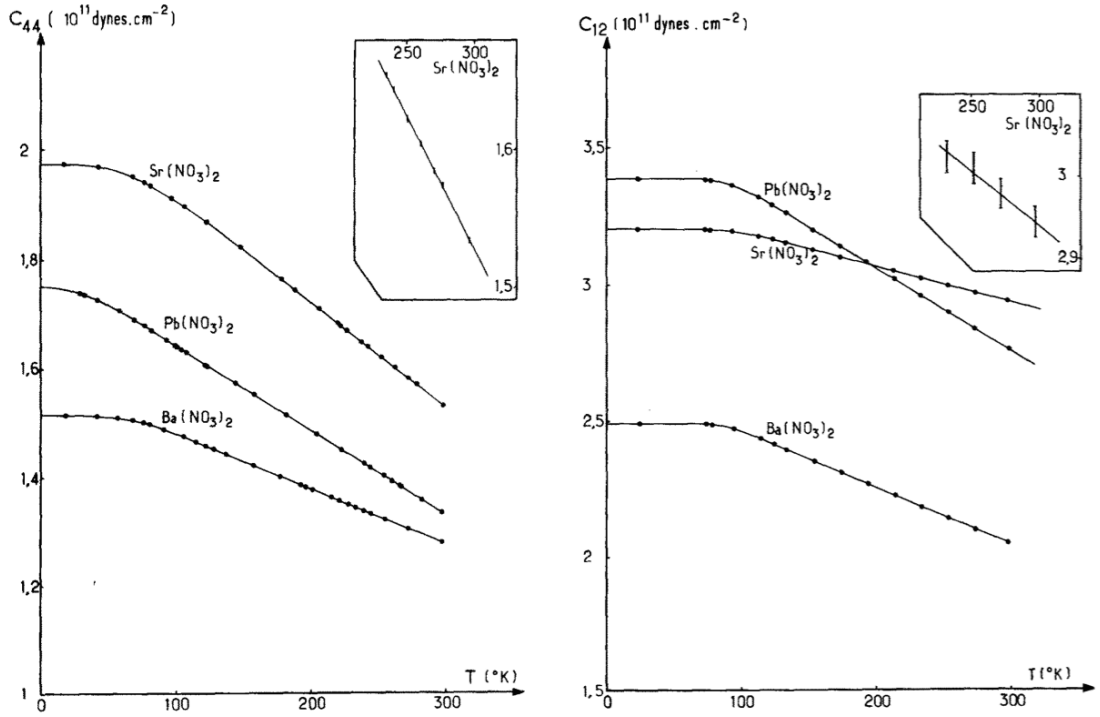

Figure 3.2: Temperature dependence of C_{44} and C_{12} for strontium, lead, and barium nitrates. Insert shows the amount of experimental error [17].

polyhedral morphology, typically with a dodecahedron shape bounded by the {100} and {111} faces. They report that barium ions appear to change the properties of their $Ba_xSr_{1-x}(NO_3)_2$ Raman shifter, simply suggesting that the barium ions degrade the crystal perfection.

A series of $Ba_xSr_{1-x}(NO_3)_2$ crystals were grown from aqueous solutions with varying initial Ba^{2+}:Sr^{2+} ratios to investigate the crystal growth and morphology of $Sr(NO_3)_2$, $Ba(NO_3)_2$ and $Ba_xSr_{1-x}(NO_3)_2$ crystals [19]. It was reported that $Ba(NO_3)_2$ crystals grown always showed an octahedral habit with {111} faces. They also showed that barium nitrate crystals precipitating from aqueous solutions had an octahedral shape, strontium nitrate crystals had a tetragon-trioctahedral shape, and crystals of their solid solution had irregular intermediate shapes of truncated octahedron. Figures 3.4 and 3.5 show the illustrations of the morphological changes on the crystals with regards to concentration.

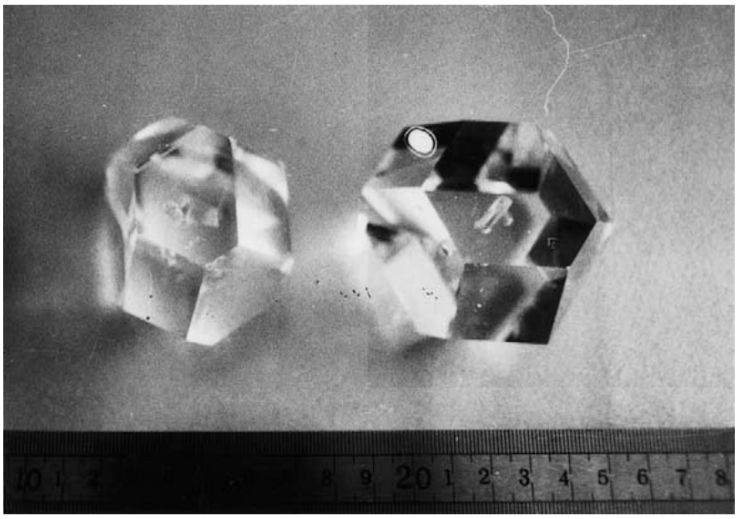

Figure 3.3: "Photograph of $Sr(NO_3)_2$ left and $Ba(NO_3)_2$ (right)" [18].

Since Ba^{2+} is larger than Sr^{2+} it can be expected that increasing the concentration of Ba^{2+} should affect the growth and morphology of the complex crystal. Figure 3.6a shows the relationship between lattice parameter a, and the solid mole fraction, $\chi_{Ba,s}$, of Ba^{2+}. The plot highlights that there is an almost linear relationship between the concentration of Ba^{2+} and lattice size, which is in good agreement with Vegard's law. This linear correlation has been further verified in more recent studies, see figure 3.6b [20]. In the limits of $\chi_{Ba,s}$, where you have pure $Sr(NO_3)_2$ ($\chi_{Ba,s} = 0\,\%$) and pure $Ba(NO_3)_2$ ($\chi_{Ba,s} = 100\,\%$), the lattice parameter is in good agreement with the lattice parameters quoted in literature for pure strontium nitrate and barium nitrate, 7.7813 Å and 8.1184 Å, respectively [10].

Another experimental study investigated the crystal growth, surface topology, and micromorphology of the surfaces of the mixed $Ba_xSr_{1-x}(NO_3)_2$ crystal complex, employing Atomic Force Microscopy [21]. The crystals were grown by slow evaporation of aqueous solutions. The temperatures in which the crystals were grown ranged from 25-35 °C and the size of the crystals ranged from 2–20 mm with polyhedral morphologies. They reported that the crystal growth is favoured

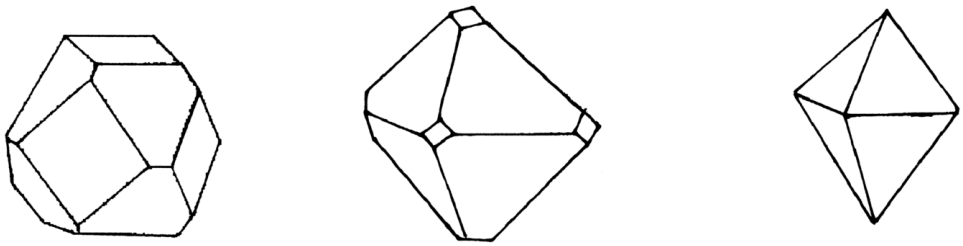

(a) $X_{Sr,s}$=1, {111}≈{100} (b) $X_{Ba,s}$>0.15, {111}>{100} (c) $X_{Ba,s}$=1, {111}

Figure 3.4: "Illustration of the morphological changes of the crystals grown through the spontaneous nucleation procedure (a)-(c) represent the different habits at different compositions of the crystals" (taken from [19]).

by two dimensional growth and the main factors governing the morphologies were the concentration of Ba^{2+}/Sr^{2+} ions in the solution, growth temperature, and the degree of supersaturation.

3.2.3 Lattice parameter vs. composition

Lattice parameter as a function of composition can be seen in figures 3.6a, and 3.6b. The linear equation describing the trends for 3.6a is

$$y = 0.3371x + 7.7813 \tag{3.1}$$

The lattice constant has been determined through powder X-ray diffraction (PXRD) patterns, using several reflections and applying least squares treatment [22]. Their results supported the view that the lattice constants loosely follow Vegard's law. Although the results show deviations on either side of the linear fit, they are within the "order of accuracy in the measurement of the lattice constants". Other studies also agree that $Ba_xSr_{1-x}(NO_3)_2$ lattice parameters follow Vegard's law [19].

Another study was only able to produce single phase mixed crystals in the range $x < 0.3$ and $x > 0.6$, stating that crystals grown within that range con-

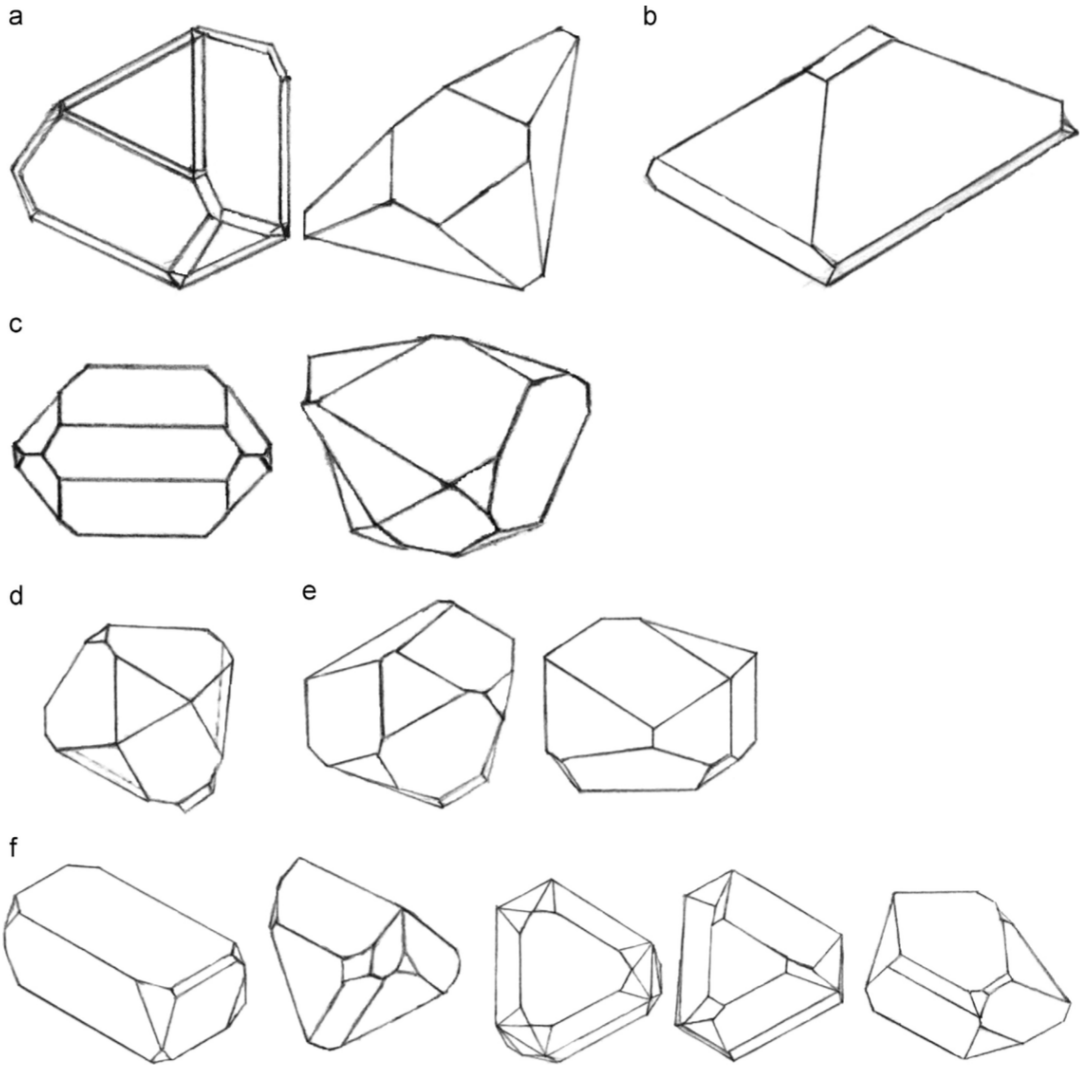

Figure 3.5: Crystal morphologies of $Ba_xSr_{1-x}(NO_3)_2$. (a) $x = 0.2$, (b) $x = 0.3$, (c) $x = 0.6$, (d) $x = 0.7$, (e) $x = 0.8$, and (f) $x = 0.9$ (taken from [21]).

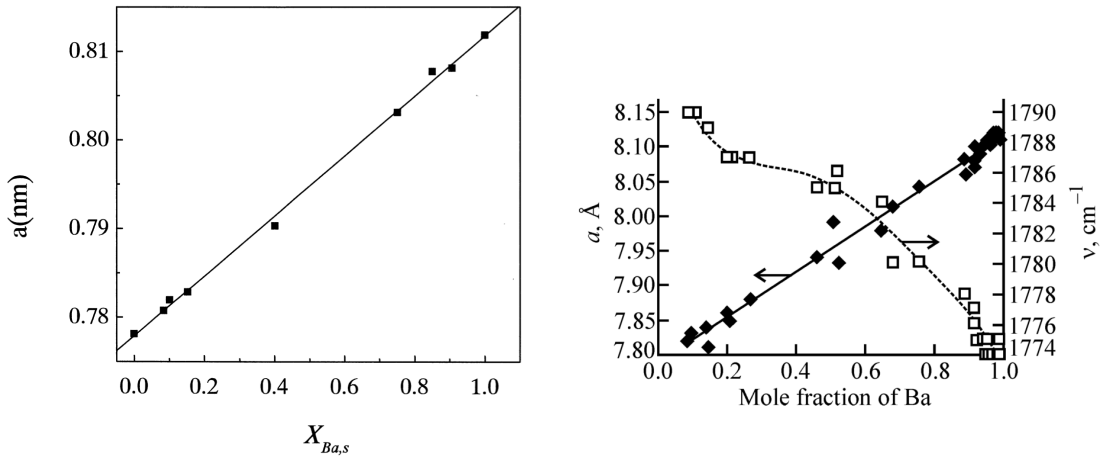

(a) (b)

Figure 3.6: (a) Lattice parameters of $Ba_xSr_{1-x}(NO_3)_2$ solid solution vs. the solid mole fraction of Ba^{2+} [19]. (b) Cubic unit cell parameter a and wavenumber of nitrate ion peak ν as functions of the chemical composition of the $Ba(NO_3)_2$-$Sr(NO_3)_2$ solid solution [20].

sisted of two phases, indicating a miscibility gap [22]. Where a miscibility gap defines a region within a phase diagram in which mixtures exist as two or more phases. Furthermore, within the same range ($0.3 < x < 0.6$) for $Ba_xSr_{1-x}(NO_3)_2$, all crystals grown in a separate study were said to have "no texture", further indicating the presence of the miscibility gap [20].

3.2.4 Solubility in water

In the interest of Raman laser application, the solubility and concentration distribution of $Ba(NO_3)_2$ and $Sr(NO_3)_2$ during the crystal growth and dissolution processes has been investigated [18]. The experimental setup involved using a saturated aqueous solution prepared by dissolving the chemical powder of $Ba(NO_3)_2$ (99.5 wt.%) and $Sr(NO_3)_2$ (99.5 wt.%) in de-ionized water. Single crystal growth was achieved by solvent evaporation and by decreasing the temperature. Nucleation and growth of $Ba_xSr_{1-x}(NO_3)_2$ was achieved by mixing the $Ba(NO_3)_2$ and $Sr(NO_3)_2$ raw materials, before dissolved in the de-ionised water. Their results

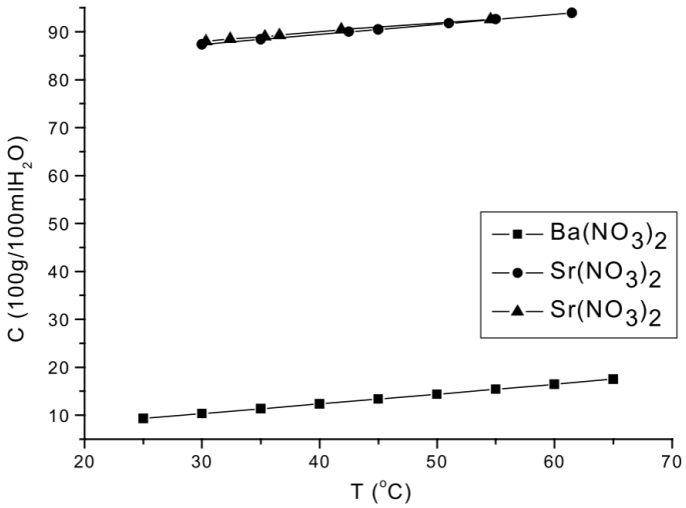

Figure 3.7: Solubility of $Sr(NO_3)_2$ and $Ba(NO_3)_2$ in H_2O as a function of temperature [18].

for the relationship between temperature and solubility can be seen in figure 3.7. From which the relationship of solubility C (g nitrate/100 g H_2O) and the temperature T (°C) are derived as

$$C = 0.22T + 81.17 \qquad \text{for } Sr(NO_3)_2 \tag{3.2}$$

$$C = 0.204T + 4.19 \qquad \text{for } Ba(NO_3)_2 \tag{3.3}$$

It can be seen that the solubility for both crystals increases with temperatures and that $Sr(NO_3)_2$ has a much higher solubility than $Ba(NO_3)_2$.

3.2.5 Solubility in HNO_3

A series of calculations have been performed to determine the solubility of $Ba(NO_3)_2$ and $Sr(NO_3)_2$ in HNO_3 solutions at 25, 50 and 90 °C, the results can be seen in table 3.3 [23]. The study also shows that in strongly acidic solutions $Ba(NO_3)_2$ coprecipitates with $Sr(NO_3)_2$. It was found that coprecipitation of $Sr(NO_3)_2$

Table 3.3: Solubility (M) of $Ba(NO_3)_2$ and $Sr(NO_3)_2$ in HNO_3 solutions at various temperatures (taken from [23]).

$[HNO_3]$, M	$Ba(NO_3)_2$			$Sr(NO_3)_2$		
	25°C	50°C	95°C	25°C	50°C	95°C
0	*0.39*	*0.62*	*1.07*	*3.40*	*3.47*	3.59
0.5	*0.20*	0.35	0.75	*2.75*	*3.15*	3.25
1	0.11	0.22	0.48	*2.50*	*2.82*	2.99
2	0.05	0.1	0.24	1.92	2.2	2.40
3	0.036	0.051	0.102	1.45	1.65	1.88
4	0.017	0.034	0.073	–	1.1	1.3
5	0.010	0.024	0.044	0.69	0.75	0.95
7	0.008	0.013	0.020	0.22	0.30	0.36
8	*0.007*	0.009	–	0.085	0.18	0.18
9	*0.005*	0.0062	0.011	–	0.057, *0.10*	0.11
12	*0.0007*	0.0010	0.0040	0.007	*0.0145*	0.025
14	*0.0002*	0.00043	0.00081	–	*0.0046*	0.005
16	–	0.00016	0.00026	–	–	0.001

with excess $Ba(NO_3)_2$ only occurs in water and sharply decreases with increased acidity, disappearing entirely in certain acid concentrations.

3.2.6 Coprecipitation of barium and strontium nitrate

Mishina *et al.* examined the molar solubilities of barium, strontium and lead nitrates, confirming formation of metastable adducts with nitric acid. Infrared spectroscopy and X-ray diffraction studies also indicated a conversion of the mixed salts into $(Ba,Sr)(NO_3)_2$ solid solution [24]. Figure 3.8 shows the formation of $(Ba,Sr)(NO_3)_2$ as a function of nitric acid concentration. Extensive research on the $Ba_xSr_{1-x}(NO_3)_2$ complex, investigating the effect of HNO_3 concentration on precipitation, has also been performed [20].

3.3 Computational studies

A three-body potential was developed and used to describe cohesive and anharmonic properties of barium, strontium and lead nitrates of fluorite structure [25]. Following this, a rigid ion model force field was derived by Hammond *et*

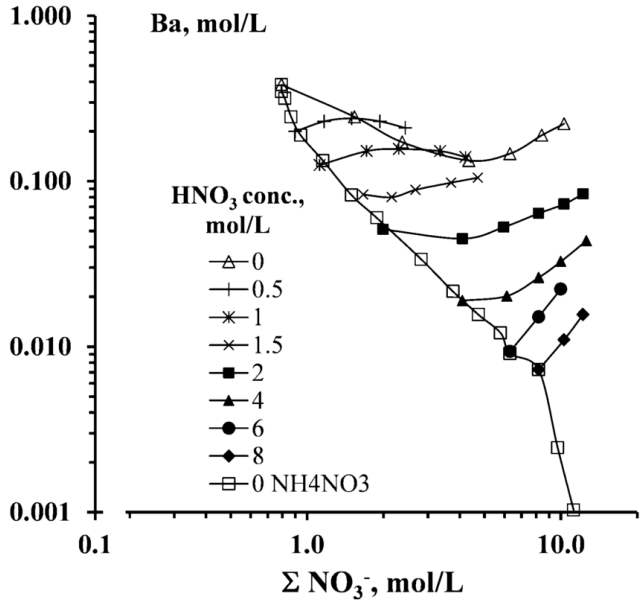

Figure 3.8: "Formation of $(Ba,Sr)(NO_3)_2$ solid solution during coprecipitation at different nitric acid concentration and Ba:Sr initial molar ratios" [24].

al. [26] for divalent nitrates. The NO_3^- parameters were adapted from a previous study by Mort *et al.* [27], who originally optimised the values for $Na(NO_3)$ and NH_4NO_3. Hammond *et al.* introduced a two body Buckingham potential for $M^{2+}-O^{2-}$ (where M = Ba, Sr, and Ca), optimising using empirical data of the crystal structure (lattice constant, interatomic spacing, and symmetry). The original NO_3^- potential values were used and only the $M^{2+}-O^{2-}$ were optimised for the new force field. They maintained a -1 charge on the overall anion, but used partial charges on the oxygen and nitrogen ions. Their lattice parameters for the fully relaxed crystal lattice for divalent species support findings from experimental crystal structures.

Rigid ion models have been shown to be inappropriate for defect calculations and solid solution work [28]. It is likely that the introduction of shell model potentials in the developed force field would improve the modelling of defects and solid solutions for nitrates. This may specifically be the case with regards to atom relaxation around point defects. The shell model has previously been used

to develop a successful force field for MgO and water surface calculations [29]. Therefore, a shell model of nitrates would help with fitting a water potential, which could be further adapted to perform solubility calculations.

A DFT study was performed using *ab initio* DFT to investigate the elastic and photoelastic properties of oxides and nitrates of alkaline-earth metals ($M(NO_3)_2$, MO, where M = Mg, Ca, Sr, Ba) [30]. They used a PBE functional in the CRYSTAL 14 software package [31], which uses atomic orbitals for their calculations rather than planewaves basis sets (these are described in detail in section 4.3.2). All their calculations were "performed without change in default settings of the CRYSTAL 14 software package", which undermines the reliability of the results somewhat, since it is unknown whether the default settings are appropriate for the system of interest.

3.4 Conclusions

In this chapter a review of the experimental, and computational, literature relevant to $Ba(NO_3)_2$, $Sr(NO_3)_2$, and $Ba_xSr_{1-x}(NO_3)_2$ has been given. The experimental work ranges from structural refinement of the crystals, to co-precipitation (and solubility) of $Ba(NO_3)_2$ in both water and HNO_3. These studies provide valuable information with regards to the HAST issues, but they provide limited insight into the physics of the crystal formation and the precise properties that govern them, such as defect formation energies and solid solution thermodynamics. This first step towards using classical computational methods to study $Ba_xSr_{1-x}(NO_3)_2$ was made by Hammond *et al.* [26] with their force-field, but it is possible still to further improve on their work by introducing further interatomic potentials. Furthermore, it is also possible to gather valuable insight into the electronic properties (as well as stability) of the divalent nitrates through the use of DFT.

Chapter 4

Computational theory

4.1 Introduction

This chapter will outline and describe the theory that underpins density functional theory. Starting from the original underlying theory it will then explain the implementation of the theory into computational methods. Following this, the methods and theory of interatomic potentials will be described, with particular reference to fitting and developing an all-atom force field.

4.1.1 Computational software

For the DFT calculations the CASTEP code [32] was used, which uses a plane wave basis set to perform electronic structure calculations. The following theory section will be therefore written accordingly. All work on interatomic potentials was performed using the General Utility Lattice Program (GULP) [33] is a molecular dynamics program that can calculate properties of bulk materials, of the order of thousands of atoms.

4.2 Density functional theory

4.2.1 The many-body problem

For a system of nuclei and electrons all physical quantities can be determined by solving the Schrödinger equation, which states that the many-body wavefunction ψ is an eigenstate of the Hamiltonian operator $\hat{H}$

$$\hat{H}\Psi = E\Psi \tag{4.1}$$

where E is the total energy of the system. The Hamiltonian operator for a many-particle system can be expressed as

$$\hat{H} = \hat{T}_e + \hat{V}_{ee} + \hat{T}_N + \hat{V}_{NN} + \hat{V}_{Ne} \tag{4.2}$$

where $\hat{V}$ is the potential energy operator, $\hat{T}$ is the kinetic energy operator, and e and N indicate electrons and nuclei, respectively. $\hat{H}$ can also be expressed explicitly as

$$\begin{aligned}\hat{H} = &-\sum_i \frac{\hbar^2}{2m_e}\nabla^2_{\mathbf{r}_i} + \frac{1}{2}\sum_{i\neq i'}\frac{e^2}{|\mathbf{r}_i - \mathbf{r}_{i'}|} - \sum_j \frac{\hbar^2}{2M_j}\nabla^2_{\mathbf{R}_i} \\ &+ \frac{1}{2}\sum_{j\neq j'}\frac{Z_j Z_{j'} e^2}{|\mathbf{R}_j - \mathbf{R}_{j'}|} - \sum_{i,j}\frac{Z_j e^2}{|\mathbf{r}_i - \mathbf{R}_j|}\end{aligned} \tag{4.3}$$

where $\mathbf{R}$ and $\mathbf{r}$ represent the coordinates of the nuclei and electrons, whereas M and m_e denote the mass of the nuclei and electrons, respectively. The $\hbar$ term is Planck's constant divided by 2π, and Z and e denote the charge of the nuclei and electrons, respectively.

The wavefunction of a molecule is a function of the coordinates of all the electrons and nuclei

$$\Psi(\mathbf{r}_1, \mathbf{r}_2, \ldots, \mathbf{r}_{N_{\text{electrons}}}, \mathbf{R}_1, \mathbf{R}_2, \ldots, \mathbf{R}_{N_{\text{nuclei}}}) \tag{4.4}$$

Due to their difference in mass, nuclei move significantly slower than electrons, so much so, that it is possible to consider electrons moving in a field of fixed nuclei. This allows us to neglect the nuclear kinetic energy term ($\hat{T}_N$) in the Hamiltonian and to consider the nuclei as a fixed external potential ($\hat{V}_{ext}$) acting on the electrons. This is known as the Born-Oppenheimer approximation [34]. Using this approximation we can write the time-independent, non-relativistic, Schrödinger equation as

$$\hat{H}_e\Psi(\mathbf{r}_1, \mathbf{r}_2, \ldots, \mathbf{r}_N) = E\Psi(\mathbf{r}_1, \mathbf{r}_2, \ldots, \mathbf{r}_N) \tag{4.5}$$

where the Hamiltonian is now expressed as

$$\hat{H} = \hat{T}_e + \hat{V}_{ee} + \hat{V}_{ext} \tag{4.6}$$

where $\hat{V}_{ext}$ is the potential acting on the electrons due to the nuclei. Again, this can be explicity expressed as

$$\hat{H} = -\frac{\hbar^2}{2m_e}\sum_i \nabla_i^2 + \sum_{i\neq j}\frac{1}{|\mathbf{r}_i - \mathbf{r}_j|} + \hat{V}_{ext} \tag{4.7}$$

Many attempts have been made to find an appropriate solution to the many-body Schrödinger equation.

4.2.2 The Hartree approximation

The Hartree approximation introduced the first step towards overcoming the many-body problem. This was achieved by considering individual electrons to be acting under an *effective potential* generated by all other electrons. In doing so the many-body problem is reduced to the solution of single-electron Schrödinger equations. The idea was that the total wavefunction could be expressed as a product of single-electron wave functions (assumed to be orthonormal) called

atomic orbitals where

$$\Psi(\mathbf{r}_1, \mathbf{r}_2, \ldots, \mathbf{r}_N) = \psi_1(\mathbf{r}_1)\psi_2(\mathbf{r}_2)\ldots\psi_N(\mathbf{r}_N). \tag{4.8}$$

This introduced the Hartree potential which replaces the electron-electron interaction term within the Hamiltonian, making the Schrödinger equation more manageable. However, the Hartree approximation neglects the fermionic properties of electrons and therefore does not satisfy *Pauli's exclusion principle* which states that no two identical fermions can occupy the same quantum state within a quantum system simultaneously. Or in other words, particles of half-integer spin must have antisymmetric wavefunctions. The implication of the exclusion principle requires that the many-body wavefunction must be antisymmetric with respect to the interchange of *any* two electron coordinates e.g.

$$\Psi(\mathbf{r}_1, \mathbf{r}_2, \ldots, \mathbf{r}_N) = -\Psi(\mathbf{r}_2, \mathbf{r}_1, \ldots, \mathbf{r}_N). \tag{4.9}$$

This particular shortcoming was amended by the Hartree-Fock method which introduced a way of describing a wavefunction that satisfies the principle of indistinguishability. This is done by building an antisymmetric solution through the introduction of the *Slater determinant*, which instructs how to build up a properly asymmeterized wavefunction as a product of one-electron wave functions.

$$\Psi(\mathbf{r}_1, \mathbf{r}_2, \ldots, \mathbf{r}_N) = \frac{1}{\sqrt{N!}} \begin{vmatrix} \psi_1(\mathbf{r}_1) & \psi_1(\mathbf{r}_2) & \ldots & \psi_1(\mathbf{r}_N) \\ \psi_2(\mathbf{r}_1) & \psi_2(\mathbf{r}_2) & \ldots & \psi_2(\mathbf{r}_N) \\ \ldots & \ldots & \ldots & \ldots \\ \psi_N(\mathbf{r}_1) & \psi_N(\mathbf{r}_2) & \ldots & \psi_N(\mathbf{r}_N) \end{vmatrix} \tag{4.10}$$

where the $1/\sqrt{N!}$ term is a normalisation constant.

The Coulomb energy of the electron system is diminished by initiation of the spatial separation of electrons which have the same spin. This reduction of

the Coulomb energy is known as the exchange energy (x). Whilst the electron exchange energy is taken into account within the Hartree-Fock method, the electronic correlation (c), the effect of an electron on all the others, is neglected. This electron correlation energy can be determined by calculating the difference between the exact energy and the Hartree-Fock solution energy.

4.2.3 Hohenberg-Kohn theorems

DFT proposes a novel solution to the issues that arise within the Hartree-Fock method. An alternative approach to overcoming the many-body problem began with the introduction of the Hohenberg-Kohn theorems [35], which are as follows

> **Theorem 1 :** For any system consisting of electrons moving under the influence of an external potential $V_{ext}(\mathbf{r})$, that potential, and hence the total energy, is determined uniquely by the ground state density (electron density) $n(\mathbf{r})$.

Corollary I: "Since the Hamiltonian is thus fully determined, except for a constant shift in the energy, it follows that the many-body wavefunctions for all states (ground and excited) are determined. *Therefore all properties of the system are completely determined given only the ground state density* $n_0(\boldsymbol{r})$" [36].

> **Theorem 2 :** The total energy of a system can always be expressed as a universal functional of the electron density, $E(n(\mathbf{r}))$, for any external potential $V_{ext}(\mathbf{r})$. The ground state energy located at $E(n_0(\mathbf{r}))$ is the global minimum of the functional $E(n(\mathbf{r}))$.

Corollary II: "The functional $E[n]$ alone is sufficient to determine the exact ground state energy and density. In general, excited states of the electrons must be determined by other means" [36].

In other words they demonstrated that the electron density can completely determine the total ground state energy (E) of a system of interacting particles.

4.2.4 The Kohn-Sham equations

Following on from the Hohenberg-Kohn theorems, Kohn and Sham introduced the Kohn-Sham ansatz which states that "the ground state of the original interacting system can be mapped into a referenced system of non-interacting electrons with the equivalent ground state density" [37]. Essentially, the Kohn-Sham method uses a Hamiltonian that is easier to solve in place of the original, complex interacting particle Hamiltonian. The Kohn-Sham Hamiltonian uses non-interacting electrons and assumes their density to be the same as in the true interacting system.

The single-particle density and the total densities of the system are described by

$$n_i(\mathbf{r}) = |\psi(\mathbf{r}_i)|^2 \tag{4.11}$$

and

$$n(\mathbf{r}) = \sum_{i}^{N} n_i(\mathbf{r}). \tag{4.12}$$

It is then possible to express the Kohn-Sham equation, which is similar to a single-electron Schrödinger equation, as

$$\left(-\frac{1}{2}\nabla^2 + V_{\mathrm{KS}}(\mathbf{r})\right)\psi_j(\mathbf{r}) = \epsilon_j\psi_j(\mathbf{r}) \tag{4.13}$$

where V_{KS} is the Kohn-Sham potential (sometimes referred to as the *effective* potential), which can be expressed as

$$V_{\mathrm{KS}}(\mathbf{r}) = V_{ext}(\mathbf{r}) + V_H(\mathbf{r}) + V_{xc}(\mathbf{r}) \tag{4.14}$$

where $V_{ext}(\mathbf{r})$ is the external potential, $V_H(\mathbf{r})$ is the Hartree potential

$$V_H = \int \frac{n(\mathbf{r}')}{|\mathbf{r} - \mathbf{r}'|} d\mathbf{r}' \tag{4.15}$$

and $V_{xc}(\mathbf{r})$ is the exchange-correlation potential, which can be written as

$$V_{xc}(\mathbf{r}) = \frac{\delta E_{xc}}{\delta n(\mathbf{r})}. \tag{4.16}$$

The functional E_{xc} represents the *exchange-correlation* (xc) energy, which is a composition of the exchange energy and the correlation energy ($E_{xc} = E_x + E_c$).

4.2.5 The exchange-correlation functional

All the awkward terms are grouped together in the E_{xc} term, which is unknown, and has no analytical expression. As such, for any actual application of the E_{xc} functional, approximations are required.

The local density approximation

The so-called *local density approximation* (LDA) is the simplest method for describing the exchange-correlation functional. It assumes that the electron density is uniform locally and is expressed as

$$E_{xc}^{\mathrm{LDA}}[n(\mathbf{r})] = \int n(\mathbf{r})\epsilon_{xc}(n(\mathbf{r}))d\mathbf{r} \tag{4.17}$$

where $\epsilon_{xc}(n)$ is the exchange-correlation energy density per electron in a homogeneous electron gas of density n. Although the LDA functional is arguably a crude approximation, it has been widely used in the literature and has been shown to be quite successful in producing good results for various systems although it is widely known to generally underestimate lattice parameters [38; 39].

The generalised gradient approximation

Unlike the LDA functional, *generalised gradient approximations* (GGA) are adapted to include, and account for, the gradient of the electron density. Generally, most GGA functionals contain the LDA functional with an additional correction term,

written as

$$\epsilon_{xc}^{\mathrm{GGA}}[n] = \int \epsilon_{xc}^{\mathrm{LDA}}[n] + \Delta\epsilon_{x/c}\left[\frac{|\Delta n(\mathbf{r})|}{n^{\frac{4}{3}}(\mathbf{r})}\right] \tag{4.18}$$

This can be further expressed as

$$E_{xc}^{\mathrm{GGA}}[n(\mathbf{r})] = \int n(\mathbf{r})\epsilon_{xc}[n(\mathbf{r})]F_{\mathrm{xc}}[n(\mathbf{r}), |\nabla n(\mathbf{r})|]d\mathbf{r} \tag{4.19}$$

where $F_{xc}[n(\mathbf{r}), \Delta n(\mathbf{r})]$ is referred to as the enhancement factor. There are many different approximations that exist such as the early GGA PW91 [40], which was followed by the GGA PBE [41], and the GGA WC [42].

4.3 Computational methods

4.3.1 Bloch's theorom and k-points

Bloch's theorem states that the wavefunction of an electron in a periodic potential may be written as a product of a periodic function $u(\mathbf{r})$ and a plane wave with wave vector $\mathbf{k}$ belonging to the reciprocal lattice,

$$\psi_k(\mathbf{r}) = e^{i\mathbf{k}.\mathbf{r}}u_k(\mathbf{r}) \tag{4.20}$$

where $u_k(\mathbf{r}+\mathbf{L}) = u_k(\mathbf{r})$, in which $\mathbf{L}$ is any lattice vector, and $e^{i\mathbf{k}.\mathbf{r}}$ is an arbitrary phase factor. This implies that

$$\begin{aligned}\psi_k(\mathbf{r}+\mathbf{L}) &= e^{i\mathbf{k}.(\mathbf{r}+\mathbf{L})}u_k(\mathbf{r}+\mathbf{L}) \\ &= e^{i\mathbf{k}.\mathbf{L}}\psi_k(\mathbf{r})\end{aligned} \tag{4.21}$$

therefore it suffices to only determine the wavefunction within the unit cell, because those outside only differ by the phase factor.

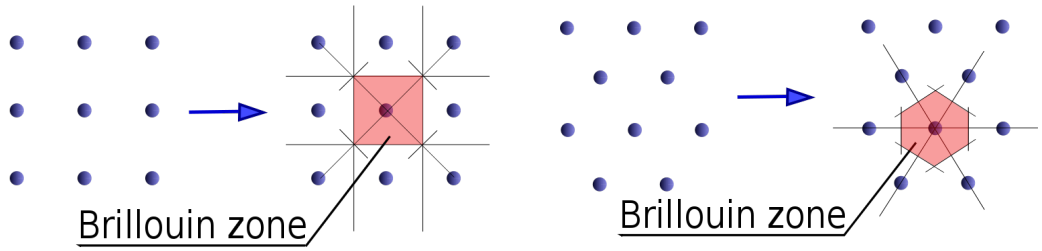

(a) (b)

Figure 4.1: Schematic diagram displaying the Brillouin zone for two different arrangements of atoms (taken from [43]).

4.3.2 Plane waves

Since $u_k(\mathbf{r})$ is a periodic function, it can be expanded in terms of a three dimensional Fourier series

$$u_k(\mathbf{r}) = \sum_G C_{Gk} e^{i\mathbf{G}.\mathbf{r}} \tag{4.22}$$

where C_{Gk} are complex Fourier coefficients and $e^{i\mathbf{G}.\mathbf{r}}$ is a plane wave travelling perpendicular to the reciprocal lattice vector $\mathbf{G}$ (which is defined such that $\mathbf{G}.\mathbf{L} = 2\pi m$). The coefficients become smaller as $|\mathbf{G}|^2$ becomes larger and since $\mathbf{G}$ is infinite is necessary to define a cutoff energy E_{cut} as

$$E_{\text{cut}} = \frac{\hbar^2}{2m}|\mathbf{G}|^2 \tag{4.23}$$

in which only plane waves within this cutoff are included. This will be referred to as the *plane wave cutoff energy*.

4.3.3 k-point sampling

Practically, k-points are used to determined the electron density at a particular point in the reciprocal lattice. Due to the repeating nature of crystals, it is only necessary to sample the reciprocal lattice in the Brillouin zone (see figure 4.1), this will provide enough information for the rest of the crystal. One way

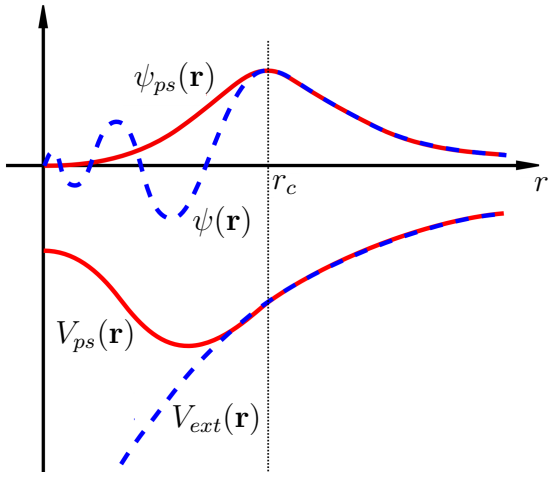

Figure 4.2: Schematic of wavefunction, pseudo-wavefunction, and pseudopotential, where r_c is the core radius, and $\psi_{ps}(\mathbf{r})$ and $V_{ps}(\mathbf{r})$ are the pseudo-wavefunction and pseudopotential, respectively (adapted from [45]).

to sample the electron density is to use a Monkhorst-Pack grid [44], which is an equally space grid of k-points with dimensions $M_x \times M_y \times M_z$. Similar to the plane wave cutoff energy, the k-point sampling needs to be carefully selected in order to get accurate results. How this is achieved is discussed in more detail in section 5.2.

4.3.4 Pseudopotentials

In order to reduce the number of calculations, and therefore computational resources, pseudopotentials are used to replicate the wavefunction of the electrons of an atom. For most calculations only the wavefunction of the outer electrons is required, since it is the outer electrons that determine the chemical properties of an atom. Instead of trying to calculate the wavefunction for all the individual atoms, a plane wave expansion is used, which satisfies the fit of the wavefunction outside the atomic radius and therefore represents all the wavefunctions of interest. See figure 4.2 for a schematic of the pseudopotential.

There are various different types of pseudopotenitals, such as ultra-soft pseudopotentials [46]. Is it also possible to omit pseudopotentials entirely, which is

the original method, performed by *all-electron* codes. Furthermore, there exist other ways for calculating the electronic structure within the framework of DFT such as the projector augmented-wave method (PAW) [47]. The merits of which have been compared with the pseudopotential methods here [48].

On-the-fly pseudopotentials

With regards to the CASTEP code, different atoms require different pseudopotentials and the pseudopotentials used for a particular calculation can either be selected from a library, or alternatively they can be generated *on-the-fly*. The advantage of using *on-the-fly* pseudopotentials is that there is a greater guarantee that the pseudopotential is up to date with current knowledge of the atoms, rather than a potentially outdated library.

4.3.5 Self-consistent field method

In practice, solving the Kohn-Sham equations requires that the total density $n(\mathbf{r})$ is consistent with the Kohn-Sham potential V_{KS}. This is achieved by choosing an initial estimate of the electron density, solving the Kohn-Sham equation for the change in density and then using the resulting wavefunction to derive a new charge density. This process is then repeated until a convergence threshold is satisfied, this is known as the self-consistent field (SCF) method.

4.3.6 Reproducibility of DFT calculations

The main solid-state DFT codes were evaluated against each other in a major study to provide a uniform benchmark of precision and reproducibility [49]. One of the main outcomes of this study was that all the DFT codes were successful in producing results of similar precision as advanced experimental techniques. The implications of this is that computational methods can be on par with experimental work [50].

4.4 Classical interatomic potentials

4.4.1 Introduction

This section briefly introduces molecular dynamic calculations, including the fundamental theory, as well as implementations. However, first the fundamental differences between DFT and classical forcefields will be explained, along with an explanation as to why it is necessary for this body of work.

As previously discussed, DFT is a powerful tool that can be used to calculate atomic forces from first principles. It calculates the electronic structure which is important, but also very computationally expensive, and so is limited by the number of atoms in the calculation. Classical molecular modelling instead uses interatomic forcefields to calculate the atomic forces and system energy. Since the electrons are not described in classical mechanics the calculations are less computationally expensive and therefore the system size can be considerably larger (100,000s of particles as opposed to 100s).

4.4.2 Theory

Development of a forcefield

Developing a force field requires evaluation of all the appropriate energy terms for every atom-atom interaction within the system. The total energy is expected to have contributions from both short and long range interactions, or namely, bonded and non-bonded interactions [51]. The energy contributions are defined as being additive, so that the total energy E_{total} can be expressed as the sum of all the contribution terms, such as

$$E_{\text{total}} = E_{\text{Coul}} + E_{\text{VDW}} + E_{\text{bond stretch}} + E_{\text{angle bend}} + E_{\text{torsion}}. \tag{4.24}$$

The first two terms are the Coulombic and van der Waals contributions, which account for the non-bonded interactions. The last three terms account for the energy contribution from the bonded interactions.

4.4.3 Bonded interactions

The contributions to the bonded, or local, energy are bond length, bond angle, and torsion. These can be written as

$$V_b(r_{ij}, \theta, \phi) = \frac{1}{2}k_s(r_{ij} - r_0)^2 + \frac{1}{2}k_b(\theta - \theta_0)^2 + k_t[1 - S\cos(n\phi)] \tag{4.25}$$

where k_s, k_b, and k_t are the bond-stretching, bond-bending, and torsional force constants, respectively. The equilibrium bond length is denoted as r_0, whereas the equilibrium bond angle is given as θ_0. Parameters S and n relate to the sign and phase of the torsion, respectively, and ϕ is the torsion angle. Finally, r_{ij} is the distance between atoms i and j.

4.4.4 Non-bonded dispersion and repulsion parameters

There are two contributions to the non-local energy

1. Van der Waals forces
2. Coulombic forces

and there are a number of ways of describing these forces. One way is to use the Lennard-Jones potential

$$V_{\mathrm{LJ}}(r_{ij}) = -\frac{A_{ij}}{r_{ij}^6} + \frac{B_{ij}}{r_{ij}^{12}}, \tag{4.26}$$

where A_{ij} and B_{ij} determine the strength of the attractive and repulsive forces, respectively. For a pair of atoms, the parameters A_{ij} and B_{ij} can be calculated

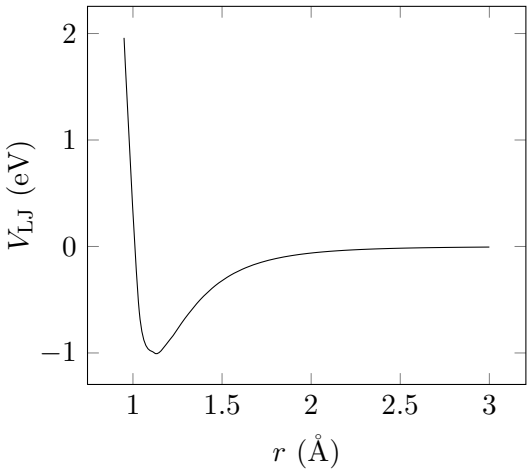

Figure 4.3: Lennard-Jones potential.

from a plot of the energy V_{ij} against distance r_{ij} (see figure 4.3). In a simplified case of two isolated atoms, if the parameters are known, then the Lennard-Jones potential could be used to determine, and govern, how non-bonded atoms respond to exterior forces.

Another way of describing both the Pauli repulsion energy as well as the Van der Waals energy, is to use the Coulomb-Buckingham potential in which interactions between non-bonded atoms i and j, can be described in terms of dispersion and repulsion interactions, and coulombic interactions, given as

$$V_{\mathrm{nb}}(r_{ij}) = -\frac{A_{ij}}{r_{ij}^6} + B_{ij} \exp\left(\frac{-r_{ij}}{\rho_{ij}}\right) + \frac{q_i q_j}{r_{ij}} \tag{4.27}$$

where r_{ij} is the separation between atoms i and j, and q_i and q_j are the partial atomic charges of atoms i and j, respectively, and A_{ij}, B_{ij} and ρ_{ij} are the unique parameters for the ion pair involved (see figure 4.4). These can be determined through empirical fitting or via *ab initio* calculations [52]. A pair of atoms i and j are usually considered non-bonded if they are in different molecules or are atoms in the same molecule separated by two or more atoms.

The Buckingham potential is usually *cut-off*, or *truncated*, at a certain distance to minimise the computational effort when calculating short-range interactions.

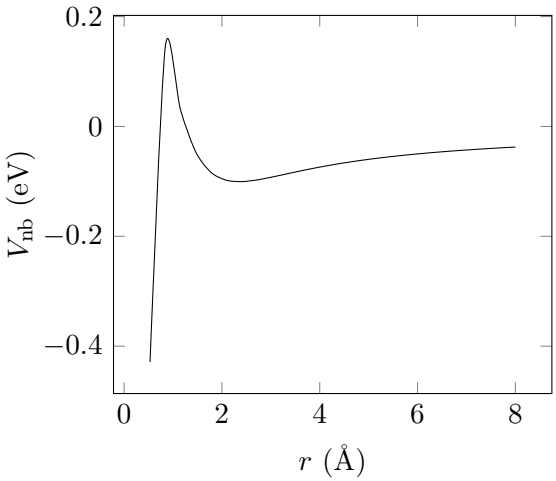

Figure 4.4: Coulomb-Buckingham potential.

The function is often varied as to approach zero at the truncation. This is to prevent drifts in energy, which can otherwise occur if the potential is far from zero at the cut-off.

The short-range interaction parameters are assumed to be related by combining rules of the form

$$A_{ij} = (A_{ii}A_{jj})^{1/2} \tag{4.28}$$

$$B_{ij} = (B_{ii}B_{jj})^{1/2}. \tag{4.29}$$

$$\rho_{ij} = (\rho_{ii} + \rho_{jj})^{1/2} \tag{4.30}$$

Substituting these rules into equation 4.27 shows that there are nine short-range parameters to determine as well as a charge quantity to be specified. It is possible to derive these quantities by a trial-and-error approach based on molecular dynamics simulations, as successfully shown by Lynden-Bell *et al.* [53].

4.4.5 Fitting

Once all the necessary interatomic potentials have been selected to describe the interactions of the material (or molecule) of interest, the parameters of these potentials need to be derived. There are two main ways to fit interatomic potentials; firstly, one can derive empirical potentials by trying to reproduce experimental data. Secondly, parameters can be determined by fitting to data from calculations, such as *ab initio* ones.

One quantity that measures how good a fit is, is the *sum of squares* (F), which is defined as

$$F = \sum_{i=1}^{N_{\text{obs}}} w_i (f_{\text{obs},i} - f_{\text{calc},i})^2 \tag{4.31}$$

where w is a weighting factor, and f_{obs} and f_{calc} are the observed and calculated quantities, respectively. The fitting process involves varying the potential parameters to minimise F, ideally to zero.

Due to the nature of the weighting factor, there is now an additional consideration that has no *official* procedure to follow. The weighting factor has an infinite number of possible solutions, therefore the choice of a sensible weighting factors is completely down to the user. That being said, there are still several criteria that help influence the choice. Firstly, the weight factor should be inversely proportional to the magnitude of the observable squared to ensure that irrespective of units, all values will be compared equally. Secondly, the reliability of the data should be carefully considered. For example, elastic constants are generally less reliable than crystal structures. The default method for minimising F is to use the BFGS algorithm [54] (which is also the default method in the geometry optimisation calculations in CASTEP).

Table 4.1: List of interatomic potential parameters published by Bush *et al.* [55].

				M^{x+}		O^{2-}			
	A/eV	ρ/Å	C/eV Å^{-6}	q (core) e	q (shell) e	q (core) e	q (shell) e	k_+/eV Å^{-2}	k/eV Å^{-2}
Li^+–O^{2-}	426.480	0.3000	0.0	1.0	—	0.513	−2.513	—	20.53
Na^+–O^{2-}	1271.504	0.3000	0.0	1.0	—	0.513	−2.513	—	20.53
K^+–O^{2-}	3587.570	0.3000	0.0	1.0	—	0.513	−2.513	—	20.53
Mg^{2+}–O^{2-}	2457.243	0.2610	0.0	1.580	0.420	0.513	−2.513	349.95	20.53
Ca^{2+}–O^{2-}	2272.741	0.2986	0.0	0.719	1.281	0.513	−2.513	34.05	20.53
Sr^{2+}–O^{2-}	1956.702	0.3252	0.0	0.169	1.831	0.513	−2.513	21.53	20.53
Ba^{2+}–O^{2-}	4818.416	0.3067	0.0	0.169	1.831	0.513	−2.513	34.05	20.53
Fe^{3+}–O^{2-}	3219.335	0.2641	0.0	1.971	1.029	0.513	−2.513	179.58	20.53
Ti^{4+}–O^{2-}	2088.107	0.2888	0.0	2.332	1.678	0.513	−2.513	253.60	20.53
Al^{3+}–O^{2-}	2409.505	0.2649	0.0	0.043	2.957	0.513	−2.513	403.98	20.53
Ga^{3+}–O^{2-}	2339.776	0.2742	0.0	3.0	—	0.513	−2.513	—	20.53
Y^{3+}–O^{2-}	1519.279	0.3291	0.0	3.0	—	0.513	−2.513	—	20.53
La^{3+}–O^{2-}	5436.827	0.2939	0.0	5.149	−2.149	0.513	−2.513	173.90	20.53
Pr^{3+}–O^{2-}	13431.118	0.2557	0.0	1.678	1.322	0.513	−2.513	302.36	20.53
Nd^{3+}–O^{2-}	13084.217	0.2550	0.0	1.678	1.322	0.513	−2.513	302.35	20.53
Gd^{3+}–O^{2-}	866.339	0.3770	0.0	−0.973	3.973	0.513	−2.513	299.96	20.53
Eu^{3+}–O^{2-}	847.868	0.3791	0.0	−0.991	3.991	0.513	−2.513	304.92	20.53
Tb^{3+}–O^{2-}	845.137	0.3750	0.0	−0.972	3.972	0.513	−2.513	299.98	20.53
Yb^{3+}–O^{2-}	−991029	0.3515	0.0	−0.278	−3.278	0.513	−2.513	308.91	20.53
O^{2-}–O^{2-}	25.41	0.6937	32.32	—	—	0.513	−2.513	—	20.53

4.4.6 Empirical vs. *ab initio* observables

Deriving force fields from *ab initio* calculations can provide several benefits; firstly, it is possible to guarantee there are no differences in temperature, pressure, variable uncertainties, or sample quality providing the *ab initio* data is treated appropriately. Secondly, the data calculated from first principle methods are free of statistical mechanical errors, such as zero point motion and thermal vibrations. Finally, there are more possibilities for obtaining data for systems that are not available from experimental studies.

4.4.7 Published interatomic potentials

There exists a database of published interatomic potentials, known as the *Database of published interatomic potential parameters*, maintained by University College London, (http://www.ucl.ac.uk/klmc/Potentials/), which, for the example of barium, has a list of potentials from: [55; 56; 57; 58]. A table of the results published by [55] can be see in table 4.1. When fitting new interatomic potentials, it is common practice to use a similar pre-existing potential to provide an initial

starting point and refit the parameters accordingly.

4.4.8 *Ab initio* molecular dynamics

As the name suggests, *ab initio* molecular dynamics (AIMD) unifies both molecular dynamics and density functional theory [59]. The classical dynamics of the interacting nuclei can be simulated by either of the following methods

1. *Ab initio* molecular dynamics
    - This method, whilst being very computationally demanding, is a very accurate method for studying the dynamics of interacting many-body systems. Each time the nuclei move, direct electronic structure calculations are performed, to determine the effective potential energy.
2. *Classical* molecular dynamics
    - Where the potential energy $E_{e,0}(\mathbf{r}_I)$ is approximated by a fixed functional form $V(\mathbf{r}_I)$ such that:

$$E_{e,0}(\mathbf{r}_I) \approx V(\mathbf{r}_I) \tag{4.32}$$

Whilst classical MD is much less computationally demanding than *ab initio* MD it is also less accurate. It does however, allow simulations of phenomena which occur over both long time-scales and large lengths.

4.5 DFT vs. classical methods

The strength of computational calculations over experimental methods is that computational work allows absolute control over the structure of interest (particularly when investigating the physics of defects), and all you to explore conditions

beyond what is possible experimentally. DFT calculations can be used to provide valuable insight into various properties of materials which are hard to probe experimentally. One of the main limitations however is that DFT calculations generally scale $O(n^3)$ with the number of atoms (n), and therefore quality calculations are limited to several hundreds atoms. Classic calculations, based on interatomic potentials, can be used to overcome the scaling issues. These calculations can be used for systems of up to millions of atoms, however the increase in scaling comes at a cost of reduced accuracy and the loss of electronic information, making it difficult to describe phenomena such as bond breaking/formation.

4.6 Conclusions

In this chapter, an overview of the underlying theory of density functional theory was presented alongside specific theory underpinning the application of DFT within the CASTEP code. Furthermore, the underlying theory of classical interatomic potentials has also been outlined and explained, including an overview of the relevant interatomic potentials to this particular body of work, as well as a description of the fitting procedure. Finally, a comparison of the two computational methods was given as well as a general discussion of the limitations and applicability of both the methods.

Chapter 5

Pure nitrates: DFT calculations

5.1 Introduction

The aim of this chapter is to use *ab initio* DFT calculations to determine the structural and elastic properties of $Ba(NO_3)_2$ and $Sr(NO_3)_2$. Before any calculations are performed the necessary convergence criteria are explained and determined. Following this, the fully relaxed crystal structures were calculated (using the PBE, WC, PW91, and LDA *xc* functionals) to determine the atomic arrangement and lattice constants. Using these relaxed structures, the bulk modulus was determined by calculating the electronic ground state energy as a function of unit cell volume and fitting the Birch-Murnaghan equation of state (EOS). Finally, the C_{11}, C_{12}, and C_{44} elastic constants were calculated by use of the stress-strain and energy-strain methods. These calculations will help compare different functionals to determine which is the most appropriate for further work. The relaxed structures will be used as the pure nitrates in the solid solution work of chapter 6. Finally, the results here will be used as observables for fitting interatomic potentials in chapter 7.

As mentioned in section 4.1.1, all DFT calculations were performed using the CASTEP code (version 7.0.1) and were conducted on the second phase Ad-

vanced Research Computing (ARC2) supercomputer at the University of Leeds. The unrelaxed initial crystal structures are imported from the Inorganic Crystal Structure Database (ICSD) [60]. Each file is taken from a published piece of work and has a unique ICSD number. Throughout this work when the initial structure is taken from the database it is referenced with the ICSD number, followed by a reference of the original paper, in the format of "ICSD xxxxx".

5.2 Convergences

Prior to performing any realistic DFT calculations, it is essential to determine the appropriate plane wave cutoff energy (E_{cut}) and k-point sampling (see section 4.3.1 for the underlying theory). With regards to the plane wave cutoff energy, since pseudopotentials are specific to individual atoms, the cutoff energy needs to be converged whenever a new type of atom is introduced into the calculation. Similarly, for the k-point sampling, different materials require different treatments, due to the dependence of cell size, symmetry, and electronic arrangement.

Convergence in this case refers to increasing the value of one of the parameters until the resulting change in the calculated ground state energy is within a predefined limit. Therefore, any further increase in said parameter will have a negligible effect on the final result. One reason for this is to try and limit the computational power required for the calculations, without compromising the quality of the results, since a greater cutoff energy and/or greater k-point sampling requires more computational power.

Single point ground state energy calculations were used for the initial convergences of plane wave cutoff energies and k-point spacing. However, it is crucial to ensure that these parameters are also fully converged with respect to the final property of interest. For example, with regards to calculating the bulk modulus, preliminary convergences of the plane wave and k-point spacing were performed to deduce initial values. These values were then used in the bulk modulus cal-

Table 5.1: ICSD and references for all initial structures used for geometry optimisation.

Material	ICSD code	Reference
$Ba(NO_3)_2$	35495	[10]
$Sr(NO_3)_2$	35494	[10]
$Pb(NO_3)_2$	62698	[62]
$Ca(NO_3)_2$	52351	[12]

culations, however, the bulk modulus calculations were repeated again with an increased cutoff energy and k-point grid size, to ensure that the change in the parameters did not alter the predicted result of interest.

5.2.1 Convergence procedure

The initial nitrate structures used for the calculations can be found in table 5.1. All convergence calculations were performed using the primitive cell and, other than the parameter being converged, all variables were fixed. The plane wave cutoff energy and k-point spacing are independent parameters, therefore one is fixed at a low value whilst the other is converged. For the preliminary convergences, the plane wave cutoff energy calculations started from 50 eV and were increased in increments of 50 eV until the change in the ground state energy converged within 0.1 eV. Likewise, for the k-point spacing, centred at the gamma point, the Monkhorst-Pack grid (n × n × n) was increased in increments of $n = 1$ until the calculated ground state energy converged within 0.1 eV. The convergence criteria of 0.1 eV is widely used for similar materials throughout the literature although it is not often justified in publications. In this body of work it is used only as a *preliminary* tolerance which will be further verified for all further calculations. For the solid solution work in chapter 6, results for $Ba(NO_3)_2$, $Sr(NO_3)_2$, and $Ba_xSr_{1-x}(NO_3)_2$ will be compared, therefore the cutoff energies and k-point spacings were selected to be consistent across all systems to help eliminate certain systematic errors [61].

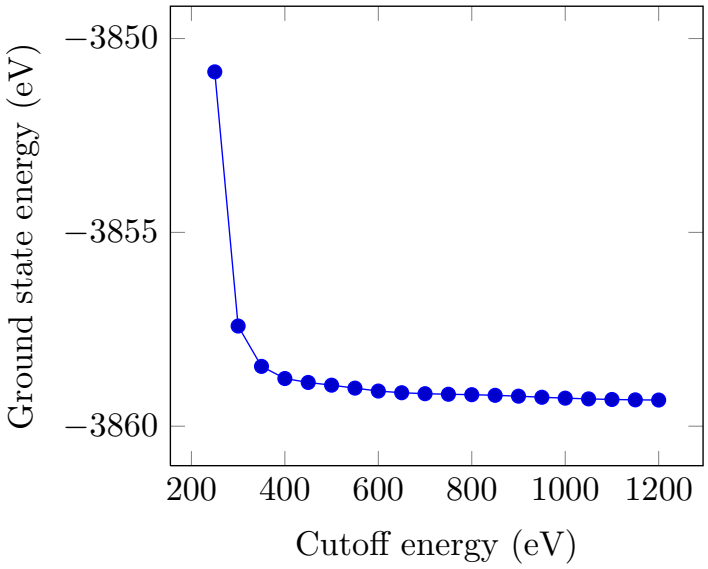

Figure 5.1: Change in electronic ground state energy as a function of plane wave cutoff energy for $Ba(NO_3)_2$.

5.2.2 Results

The results for the plane wave cutoff energy and k-point grid convergences, for $Ba(NO_3)_2$, $Sr(NO_3)_2$, and $Ba_xSr_{1-x}(NO_3)_2$, can be found is figures 5.1, 5.2, 5.3, 5.4, 5.5, and 5.6, respectively. The rest of the convergence results can be found in the appendix. The convergences for the individual structures of $Ba(NO_3)_2$, $Sr(NO_3)_2$ and $Ba_xSr_{1-x}(NO_3)_2$ were reasonably consistent, with a plane wave cutoff of 900 eV satisfying the 0.1 eV ground state energy criteria for all materials. Similarly, a k-point Monkhorst-Pack grid of $10 \times 10 \times 10$ (giving a $0.0123\,\text{Å}^{-1}$ k-point spacing for $Ba(NO_3)_2$) satisfied the 0.1 eV convergence tolerance for all nitrates of interest too. Using identical convergences has been shown to reduce particular errors when direct comparison are made between materials [61].

5.3 Structure refinement

Barium nitrate crystallises in a face centred cubic (FCC) system, within the T_h^6 group. A summary of the experimental studies investigating the $Ba(NO_3)_2$ and

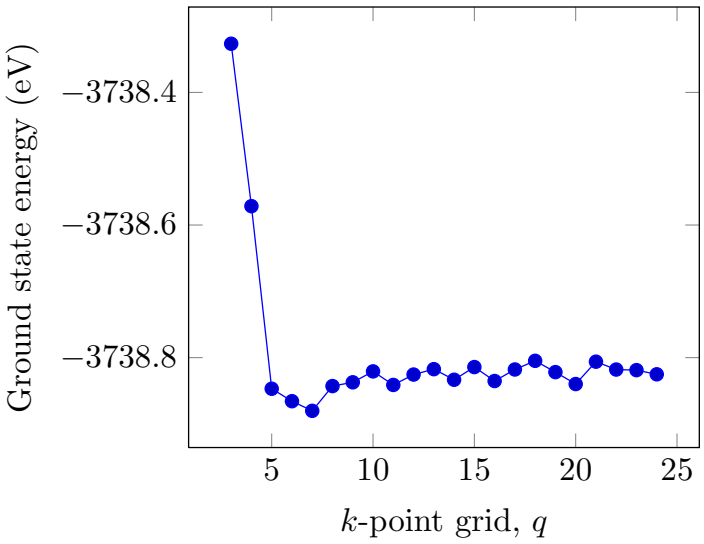

Figure 5.2: k-point sampling grid convergence for $Ba(NO_3)_2$.

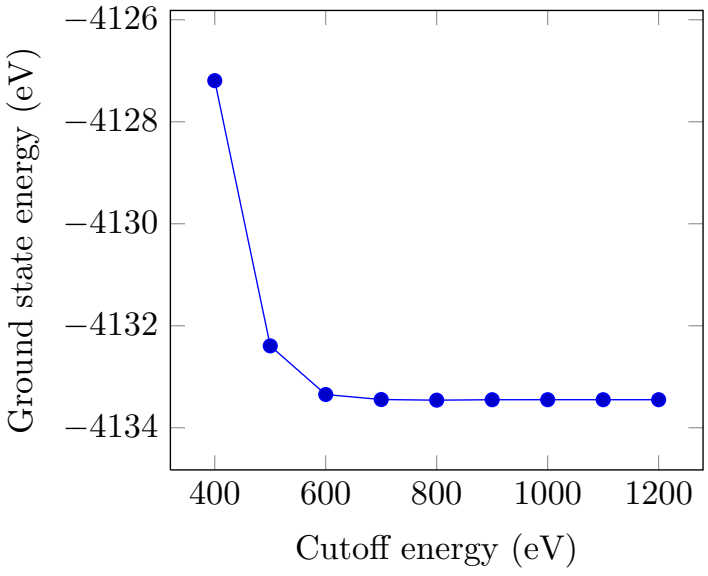

Figure 5.3: Change in electronic ground state energy as a function of plane wave cutoff energy for $Sr(NO_3)_2$.

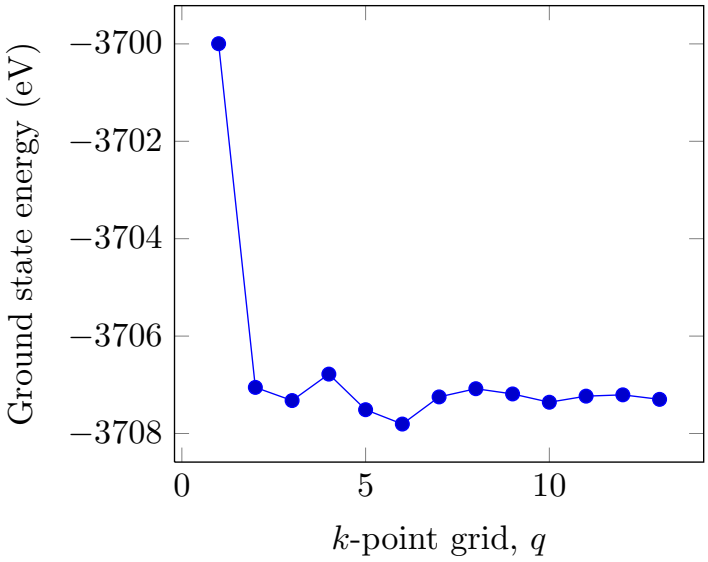

Figure 5.4: k-point sampling grid convergence for $Sr(NO_3)_2$.

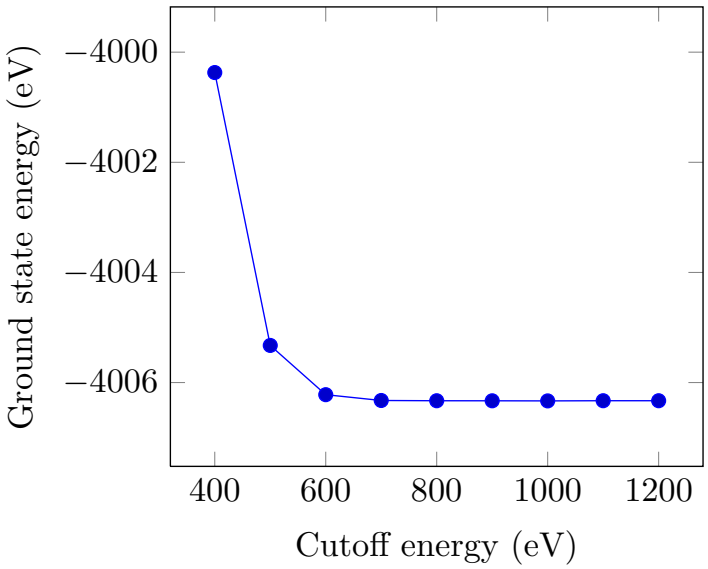

Figure 5.5: Change in electronic ground state energy as a function of plane wave cutoff energy for $Ba_xSr_{1-x}(NO_3)_2$.

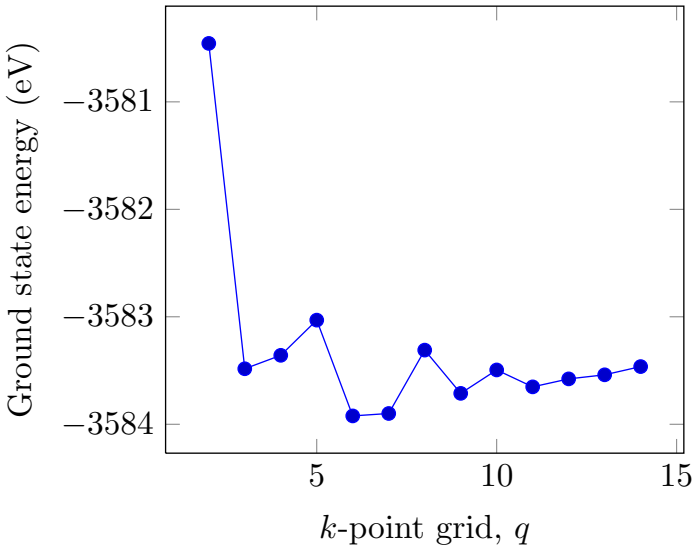

Figure 5.6: k-point sampling grid convergence for $Ba_xSr_{1-x}(NO_3)_2$.

$Sr(NO_3)_2$ structure can be found in table 3.1. Figure 5.7 shows a schematic diagram of a barium nitrate unit cell.

Before more advanced crystal properties can be calculated it is paramount to have an accurate, fully relaxed, starting structure. For example, if the lattice parameters of a crystal are underestimated, and therefore the atoms are too close together, the value of the elastic constants calculated from that particular structure will be overestimated. An incorrect starting structure will lead to incorrect advanced properties. Additionally, geometry optimisations are a useful tool to get a relatively, computationally cheap insight into how successfully functionals describe the structure of interest, how they compare to each other, and their level of agreement with any available data in the literature. Experimentally, structure refinement and lattice constants are likely the most investigated properties of $Ba(NO_3)_2$ and $Sr(NO_3)_2$ and arguably produce the most reliable results, with reports showing that uncertainty from experimental lattice constants, using X-ray diffraction, can reach 0.0001 Å [63; 64].

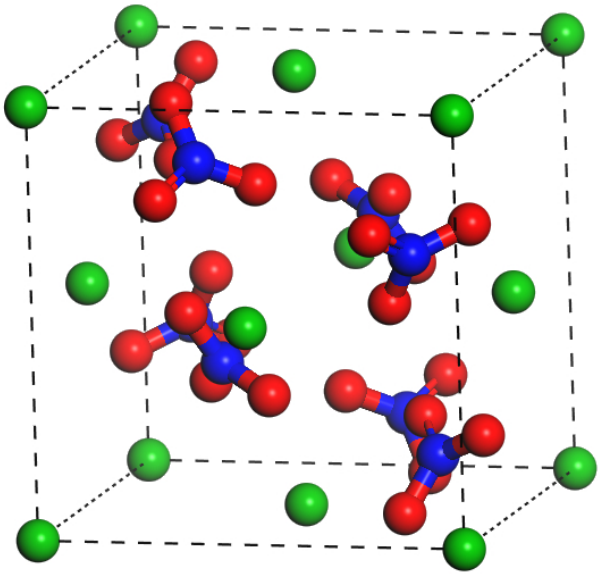

Figure 5.7: A schematic diagram of the barium nitrate unit cell. The green, blue and red atoms are barium, nitrogen, and oxygen, respectively. The bars signify covalent bonds between the relavant atoms.

5.3.1 Theory

Geometry optimisation (or structural relaxation) is a search for the lowest ground state energy a particular structure can have. It is achieved by performing a series of ground state energy calculations across varying atomic positions, until minimum enthalpy (zero force and stress) is found. There exists a range of different minimisation algorithms and the BFGS (Broyden-Fletcher-Goldfarb-Shanno) [54] method was used throughout this study.

Generally, finding an atomic arrangement in which the forces and stresses on the atoms are truly zero is impractical. Therefore, additional convergence criteria tolerances are used. These are the free energy per atom (eV), maximum atomic force (eV $Å^{-1}$), atomic displacement (Å), and maximum stress component (GPa) (the chosen tolerances can be found in table 5.2). The importance of selecting appropriate tolerances should not be overlooked. Therefore, additional calculations were performed to investigate the effect of further reducing the tolerances by up to an order of magnitude, however the change in the lattice parameter was

$< 0.1\,\%$ and considered to be negligible. The initial starting structures for the geometry optimisation calculations were taken from experimental results found in the literature (see table 5.1). Alternative initial starting positions were also tested to verify that the final, relaxed, structures are independent of the starting positions.

5.3.2 Exchange-correlation functionals

A selection of exchange-correlation functionals (PBE, LDA, WC, PW91, see section 4.2.5 for more about these) were used for the geometry optimisations, which will assist in determining how suitable a given functional is for further calculations in this study.

5.3.3 Methodology

The preliminary nitrate structures and their respective ICSD can be found in table 5.1. Both $Ba(NO_3)_2$ and $Sr(NO_3)_2$ have $Pa3$ symmetry. The geometry optimisation was performed without any imposed symmetry (also known as $P1$ symmetry) and all properties of the unit cell were allowed to relax (including cell lengths and angles). A plane wave cutoff energy of 900 eV as well as a $10 \times 10 \times 10$ Monkhorst-Pack grid sampling of the first Brillouin zone were used. Both the cutoff energy and k-point sampling were further increased in separate calculations to confirm that they have negligible effect on the final value of interest. The PBE, WC, and LDA exchange-correlation functionals were used as well as *on-the-fly* pseudopotentials. The geometry optimisation convergence thresholds used can be found in table 5.2.

5.3.4 Results

The calculated equilibrium lattice constants (a_0) of $Ba(NO_3)_2$, $Sr(NO_3)_2$, $Ca(NO_3)_2$, and $Pb(NO_3)_2$ are shown in table 5.3 (alongside available experimental data from

Table 5.2: Parameters for geometry optimisation calculations.

Parameter	Tolerance	Units
free energy per atom	4×10^{-6}	eV/atom
atomic force	1×10^{-2}	eV Å^{-1}
atomic displacement	4×10^{-4}	Å
maximum stress component	1×10^{-2}	GPa

the literature). As mentioned previously, various alternative initial atomic positions, without imposed symmetry, were used to ensure the final relaxed structure is independent of the starting structure. The final relaxed structures were all found to relax to a structure with $Pa3$ symmetry and all the predicted lattice constants were within 3 % of the experimental range. As you can see from the results, the LDA functional gave the smallest value of a_0, for all nitrates. Whereas the PBE functional gave the largest values for the lattice constants.

A selection of interatomic distances for $Ba(NO_3)_2$ and $Sr(NO_3)_2$ can be found in table 5.4. The LDA calculated a bond length of 1.252 Å for the N−O bonds, whereas the nearest neighbour, Ba−N, was 3.244 Å. (There are six nitrates within 3.244 Å distance, the next nearest is 4.814 Å, then 5.410 Å.) The O−N−O are 120°. WC gives 1.259 Å for the N−O bond and 3.331 Å for the near neighbouring Ba−N atoms.

$Ba(NO_3)_2$, $Sr(NO_3)_2$, $Ca(NO_3)_2$ and $Pb(NO_3)_2$ are isomorphic and the calculated lattice constants are consistent with the ionic radius of the cation [65; 66] which are

$$\rho_{Ca^{2+}}(1.12\,\text{Å}) < \rho_{Sr^{2+}}(1.27\,\text{Å}) < \rho_{Pb^{2+}}(1.32\,\text{Å}) < \rho_{Ba^{2+}}(1.43\,\text{Å}). \tag{5.1}$$

An overview of all the experimental data used in tables 5.3 can be found in table 3.1 and 3.2. Both single crystal and powder sample types have been used in the literature as well as X-ray and neutron radiation. Unfortunately, only half of the studies have provided information on the temperature of the experiment

and these were almost all done at 293 K. One study did calculate a_0 for $Sr(NO_3)_2$ at 173 K however, the value was still given to be within 0.001 % of the values calculated at room temperature. With only two points of reference it has not been possible to deduce any temperature effects on the lattice constants for the nitrates. With regards to the errors on the experimental lattice constants, it has been claimed that the uncertainty from X-ray diffraction can reach 0.0001 Å or even smaller [63; 64]. A more detailed discussion on the experimental literature can be found in chapter 3.

5.3.5 Discussion

As is consistent with DFT literature, for all nitrates, the LDA functional gave the smallest value of a_0, underestimating, relative to the experimental data, the lattice constants for $Ba(NO_3)_2$, $Sr(NO_3)_2$, $Ca(NO_3)_2$, and $Pb(NO_3)_2$ by up to 2.6 %, 3.7 %, 4.1 % 2.8 %, respectively. It is shown throughout the literature that LDA often under estimates the lattice parameters [38]. Since the LDA exchange functional assumes a uniform electron density throughout the structure, it is unsurprising that it does not necessarily provide an accurate description of the electron arrangement of a material that has both covalent and ionic bonds present, such as the nitrates of interest. The PBE functional gave the largest lattice constants for all nitrates, overestimating the experimental data of $Ba(NO_3)_2$, $Sr(NO_3)_2$, $Ca(NO_3)_2$, and $Pb(NO_3)_2$ by up to 2.1 %, 1.7 %, 1.7 % 1.8 %, respectively. The WC functional proved to be most consistent with experimental work, producing lattice parameters within 0.32 %, 0.76 %, 0.01 %, and 0.32 %, for $Ba(NO_3)_2$, $Sr(NO_3)_2$, $Ca(NO_3)_2$, and $Pb(NO_3)_2$, respectively. Furthermore, the relaxed structures were all found to have *Pa3* symmetry, which is in good agreement with the experimental literature (as shown in tables 3.1 and 3.2). These results show that *ab initio* DFT calculations describe the positional relationship between the atoms appropriately (regardless of whether a

LDA, GGA, WC, PW91 functional is used).

Reliability of experimental results

An important notion to bear in mind, when deciding upon the accuracy of *ab initio* calculations is whether experimental results are a reliable comparison. Arguably for simple structures in simple conditions the experimentally determined properties (like lattice parameters) will be good results to compare to. However, the range of published lattice parameters are from 0.25 % for barium and 0.4 % for strontium. In these cases it is justifiable to compare the DFT results to experimental results to determine which functional is the most appropriate.

5.4 Bulk modulus

The bulk modulus (B) describes a material's resistance to an applied uniform stress through the equation

$$B = V\frac{\delta^2 E(V)}{\delta V^2}\bigg|_{V=V_0} = -V\frac{\delta P}{\delta V}\bigg|_{V=V_0} \tag{5.2}$$

where $E(V)$ is the total ground state energy, P is the pressure, and V is the volume. Experimentally, B can be determined using powder diffraction under applied pressure, measuring the change in volume and then fitting a suitable equation of state (EOS). There exists a number of different EOSs, such as the Murnaghan, Rose-Vinet, and Poirier-Tarantola [69; 70; 71]. The relative merits have been discussed in detail by [72], who conclude that "for strains less than 30 %, it probably doesn't matter what equation of state you use". The maximum strain used in this study is ±3 % and a comparison of the different EOSs gave negligable difference in the final value. That being said, the third-order Birch-

Table 5.3: Calculated lattice parameters a_0 (Å) for $Ba(NO_3)_2$, $Sr(NO_3)_2$, $Ca(NO_3)_2$ and $Pb(NO_3)_2$, alongside available literature data. For experimental data the temperature (K) is given when available.

Material	Method	*xc* functional	a_0	Reference
$Ba(NO_3)_2$	DFT	PBE	8.277	
	DFT	WC	8.136	
	DFT	LDA	7.925	
	DFT	PW91	8.275	
	exp. (293 K)		8.1184(2)	[10]
	exp. (293 K)		8.11021(7)	[14]
	exp.		8.126	[11]
	exp.		8.126	[12]
	exp.		8.13	[13]
	exp.		8.126	[15]
	DFT†	PBE	8.370	[67]
$Sr(NO_3)_2$	DFT	PBE	7.911	
	DFT	WC	7.767	
	DFT	LDA	7.547	
	DFT	PW91	7.916	
	exp. (293 K)		7.7813(2)	[10]
	exp. (173 K)		7.822(1)	[16]
	exp.		7.826	[12]
	exp.		7.83	[13]
$Ca(NO_3)_2$	DFT	PBE	7.748	
	DFT	WC	7.616	
	DFT	LDA	7.318	
	exp.‡		7.6150	[12]
$Pb(NO_3)_2$	DFT	PBE	7.996	
	DFT	WC	7.834	
	DFT	LDA	7.648	
	DFT	PW91	7.979	
	exp.		7.8586(2)	[62]
	exp.		7.853	[17]

† Calculated with Quantum-Espresso software
‡ Naturally hydrated, included for completeness [68]

Table 5.4: Selected interatomic distances (Å) and angles (°). Experimental data taken from [10]. n is the number of equivalent values and t is the type of distance.

Atoms	t	n	xc functional	$Ba(NO_3)_2$	$Sr(NO_3)_2$
MO_{12} polyhedron					
M−O	a	6	PBE	2.935	2.760
			WC	2.882	2.703
			LDA	2.805	2.650
			exp.	2.8789 (6)	2.7153 (5)
M−O	b	6	PBE	2.999	2.886
			WC	2.947	2.828
			LDA	2.866	2.726
			exp.	2.9414 (6)	2.8381 (5)
Nitrate group					
N−O			PBE	1.271	1.263
			WC	1.259	1.257
			LDA	1.252	1.250
			exp.	1.2465 (6)	1.2467 (5)
O−O			PBE	2.201	2.188
			WC	2.180	2.178
			LDA	2.168	2.165
			exp.	2.1589 (12)	2.1594 (10)
O−N−O			PBE	120.00	120.00
			WC	120.00	120.00
			LDA	120.00	120.00
			exp.	120.00 (07)	120.00 (06)
Short N−N distances					
N−N		1	PBE	4.261	4.229
			WC	4.205	4.146
			LDA	4.097	4.032
			exp.	4.1794 (6)	4.1753 (6)
N−N		6	PBE	4.466	4.255
			WC	4.386	4.172
			LDA	4.272	4.080
			exp.	4.3803 (6)	4.1626 (6)

Murnaghan EOS [73] will be presented in this work

$$P(V) = \frac{3B_0}{2}\left[\left(\frac{V_0}{V}\right)^{\frac{7}{3}} - \left(\frac{V_0}{V}\right)^{\frac{5}{3}}\right]\left\{1 + \frac{3}{4}(B_0' - 4)\left[\left(\frac{V_0}{V}\right)^{\frac{2}{3}} - 1\right]\right\} \tag{5.3}$$

where P represents the pressure, V_0 the equilibrium volume, V is the strained volume, B_0 is the bulk modulus at zero pressure, and B_0' is the first derivative with respect to pressure,

$$B_0' = \left.\frac{\delta B_0}{\delta P}\right|_{V=V_0} = \left.\frac{\delta}{\delta P}\left(V\frac{\delta^2 E}{\delta V^2}\right)\right|_{V=V_0} \tag{5.4}$$

The internal energy $E(V)$ can be found by integration of the pressure to give

$$E(V) = E_0 + \frac{9V_0B_0}{16}\left\{\left[\left(\frac{V_0}{V}\right)^{\frac{2}{3}} - 1\right]^3 B_0' + \left[\left(\frac{V_0}{V}\right)^{\frac{2}{3}} - 1\right]^2\left[6 - 4\left(\frac{V_0}{V}\right)^{\frac{2}{3}}\right]\right\} \tag{5.5}$$

where E_0 is the equilibrium energy at zero pressure.

Computationally, B can be calculated in a similar fashion in which the lattice constants are adjusted across V_0 and the subsequent change in total energy are calculated. The data can then be fitted to equation 5.5 to get a value for B.

5.4.1 Methodology

The unstrained structure was taken from the geometry optimised calculations in section 5.3. a_0 denotes the unstrained lattice constant and for these set of calculations the lengths along all planes were set to be consistent with each other ($a = b = c$). A uniform strain was applied to a_0, ranging from $\pm$ 3% in steps of 0.5%. For each step a geometry optimisation calculation was performed with fixed lattice parameters and unit angles, but allowing internal atoms to fully relax. The electronic ground state energy (E) was then plotted against unit cell volume (V) and the Birch-Murnaghan EOS was fitted via equation 5.5.

The EOS has four unknown parameters (V_0, E_0, B_0, B') and so in order to fit the equation, a second order parabolic fit ($y = ax^2 + bx + c$) was first used. This provided analytic guesses for the unknown parameters, where

$$V_0 = -b/(2a). \tag{5.6}$$

Since the minimum volume is when $dE/dV = 0$, a preliminary guess for E_0 was therefore

$$E_0 = aV_0^2 + bV_0 + c \tag{5.7}$$

and from 5.2 we have

$$B = V_0 \frac{d^2E}{dV^2} \tag{5.8}$$

to provide an initial estimation for B. The initial estimation for B' was chosen to be 4 as it has been shown to lie between 3 and 5 for most real solids [74]. Least squares regression was then used to find the actual fit of the EOS to give the final values of V_0, E_0, B_0, and B'. In this context, the volume per formula unit is of interest, where the unit cell volume $V(a) = qa^3$ uniquely determines the lattice parameter a through a dimensionless constant q which depends on the crystal symmetry ($q = 1$, $q = 1/4$, and $q = 1/2$ for sc, fcc, and bcc lattices, respectively) [75]. Finally, it has been shown that the final values are dependent on the choice of V_0, E_0, B_0, and B' [76], therefore alternative values were also investigated to ensure the chosen values are appropriate.

5.4.2 Results

The bulk moduli of $Ba(NO_3)_2$ and $Sr(NO_3)_2$ were calculated using the PBE, WC and LDA functionals. Figures 5.8 and 5.9 show the change in ground state energy as a function of volume for $Ba(NO_3)_2$ and $Sr(NO_3)_2$ with a fitted Birch-Murnaghan EOS (equation 5.5), respectively. From these EOS fits, the bulk moduli were determined and these are given in table 5.5.

Table 5.5: Bulk modulus (B GPa) for $Ba(NO_3)_2$ and $Sr(NO_3)_2$, calculated using the Birch-Murnaghan EOS. Where a_0 is given in Å and temperature is given in K ([a] Ref. [65], [b] Ref. [77]).

Material	Method	Functional	a_0	B
$Ba(NO_3)_2$				
	DFT	PBE	8.277	27.29
	DFT	WC	8.136	28.03
	DFT	LDA	7.925	38.64
	exp.[a]			23.52
	exp.[b] (0 K)*			29
$Sr(NO_3)_2$				
	DFT	PBE	7.911	27.72
	DFT	WC	7.767	33.48
	DFT	LDA	7.547	45.89
	exp.[a]			33.66
	exp.[b] (0 K)*			38

* extrapolated from data

5.4.3 Discussion

Both the PBE and WC functionals produced values that were in reasonable agreement with the experimental results, particularly for $Ba(NO_3)_2$ where the values were within 10 % of the extrapolated 0 K values. However, the LDA functional overestimated the bulk modulus by up to 50 %, relative to the experimental values. This is because the LDA functional predicts a lower lattice constant compared to the PBE and WC functionals, therefore B calculated using the LDA functional bulk modulus is greater than the other two. Since the atoms are closer to each other they would give a greater resistance to a given strain compared with a unit cell with a larger lattice parameter. Likewise, the PBE functional predicted a smaller lattice parameter compared to the WC functional and therefore a larger value for B was calculated from the structure.

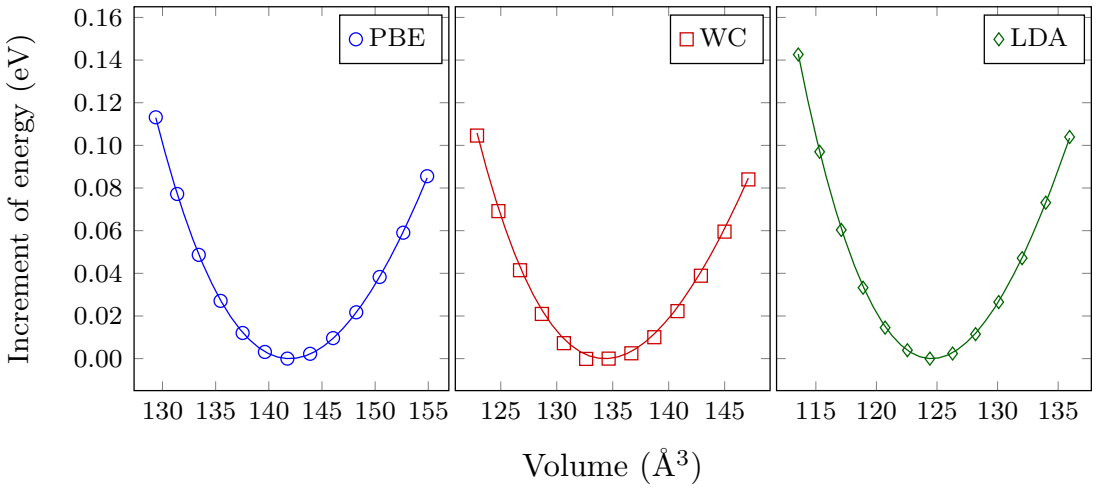

Figure 5.8: For $Ba(NO_3)_2$, the change in ground state energy, due to an applied strain, against unit cell volume. The markers are the calculated values, whereas as the solid lines represent the fitted EOS.

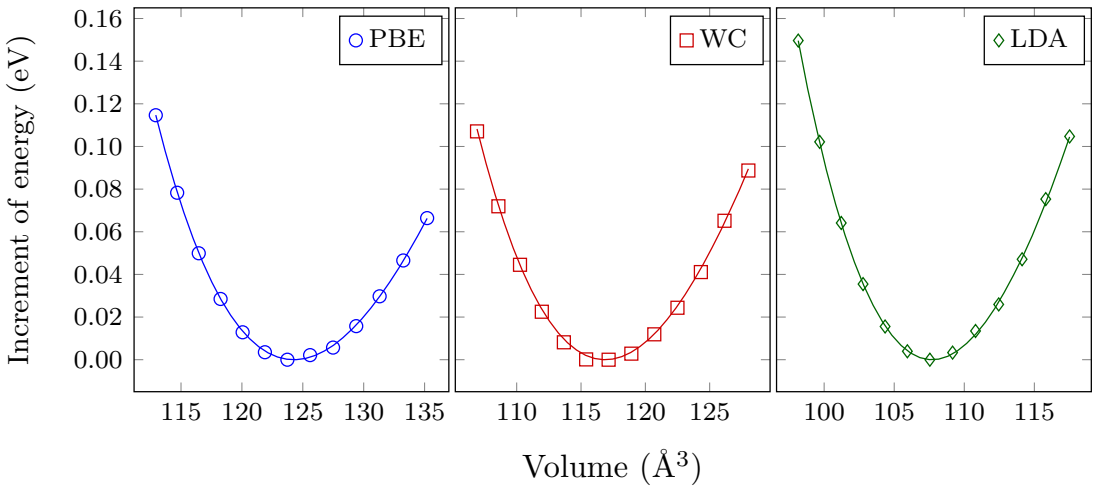

Figure 5.9: For $Sr(NO_3)_2$, the change in ground state energy, due to an applied strain, against unit cell volume. The markers are the calculated values, whereas as the solid lines represent the fitted EOS.

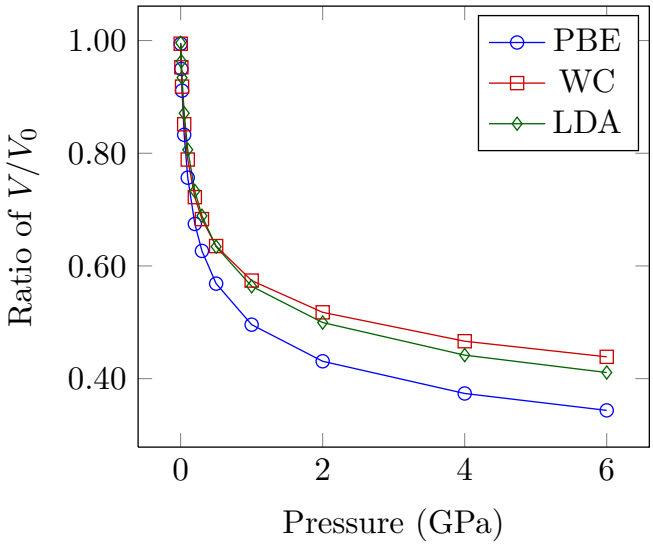

Figure 5.10: The variations about ratio of the normalized volume V/V_0 with the applied pressure for $Ba(NO_3)_2$.

5.4.4 Pressure dependence

Following on from the Birch-Murnaghan equation of state, the pressure P versus the normalised volume (V/V_0) can be obtained through the following thermodynamic relationship

$$P = -\frac{dE}{dV} = \frac{B_0}{B_0'}\left[\left(\frac{V}{V_0}\right)^{-B_0'} - 1\right], \tag{5.9}$$

where $B_0' = \frac{dB_0}{dp}$ and B_0 are the pressure derivative of the bulk modulus and zero pressure bulk modulus, respectively. The relationship of pressure as function of normalised volume can be seen in figures 5.10 and 5.11

5.5 Elastic constants

The stress-strain and energy-strain [78] have been applied extensively in the literature, however they have yet to be applied to $Ba(NO_3)_2$ or $Sr(NO_3)_2$. Barium nitrate crystallises in a face centred cubic system and therefore it has three elastic

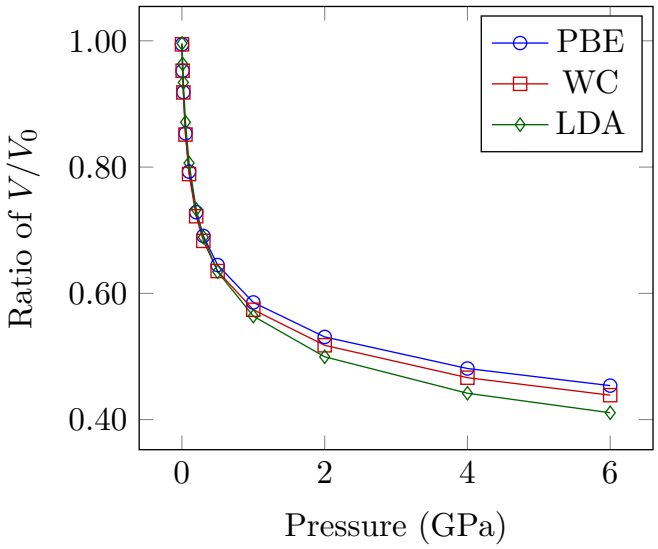

Figure 5.11: The variations about ratio of the normalized volume V/V_0 with the applied pressure for $Sr(NO_3)_2$.

constants, C_{11}, C_{12} and C_{44} [17].

5.5.1 Theory

Elastic constants are used to describe the response of materials to external forces. Experimentally, the elastic properties of a material can be determined by applying forces, which are described in terms of *stress* σ and determining displacements of atoms which are described in terms of *strain* ϵ.

Stress has components σ_{ij}, where the force can be applied along three directions (i) and on three faces (j). It is defined locally, so that $\sigma_{ij} = \sigma_{ij}(\mathrm{r})$ and there are two main types of stresses; *compression* and *shear*. Of these, there are three types of *compression stress* (σ_{xx}, σ_{yy}, σ_{zz}), where

$$\sigma_{xx} = \frac{F_x}{A_x} \tag{5.10}$$

and F_x and A_x are the force and the area in the x direction, respectively. There are also six types of *shear stress* (σ_{xy}, σ_{xz}, σ_{yx}, σ_{yz}, σ_{zx}, σ_{zy}). The shear stress of

force acting in the y direction on an area in the x direction is given by

$$\sigma_{yx} = \frac{F_y}{A_x}. \tag{5.11}$$

Similarly to stress, strain has *compression strain* (ϵ_{xx}, ϵ_{yy}, ϵ_{zz})

$$\epsilon_{xx} = \frac{du_x}{dx} \tag{5.12}$$

as well as *shear strain* (ϵ_{xy}, ϵ_{xz}, ϵ_{yx}, ϵ_{yz}, ϵ_{zx}, ϵ_{zy})

$$\epsilon_{yx} = \frac{du_y}{dx} \ . \tag{5.13}$$

Elastic constants (C) are used to relate the strain and stress in a linear fashion, where

$$\sigma_{ij} = \sum_{ij} C_{ijkl}\epsilon_{kl} \ . \tag{5.14}$$

In its most general form, the matrix C has $3 \times 3 \times 3 \times 3 = 81$ components. However, due to the symmetrical form of σ_{ij} and ϵ_{ij} only 36 elastic constants are required. These constants are denoted by C_{mn}, where indices m and n are defined as $1 = xx$, $2 = yy$, and $3 = zz$ for the compression components and as $4 = yz$, $5 = zx$, and $6 = xy$ for the shear components. In full we have the matrix

equation

$$\begin{array}{c} \\ \begin{pmatrix} \sigma_{xx} \\ \sigma_{yy} \\ \sigma_{zz} \\ \hdashline \sigma_{yz} \\ \sigma_{zx} \\ \sigma_{xy} \end{pmatrix} \\ \text{stress} \end{array} = \begin{array}{c} \overbrace{\qquad\qquad}^{\text{compression}} \quad \overbrace{\qquad\qquad}^{\text{mixed}} \\ \left(\begin{array}{ccc:ccc} C_{11} & C_{12} & C_{13} & C_{14} & C_{15} & C_{16} \\ C_{21} & C_{22} & C_{23} & C_{24} & C_{25} & C_{26} \\ C_{31} & C_{32} & C_{33} & C_{34} & C_{35} & C_{36} \\ \hdashline C_{41} & C_{42} & C_{43} & C_{44} & C_{45} & C_{46} \\ C_{51} & C_{52} & C_{53} & C_{54} & C_{55} & C_{56} \\ C_{61} & C_{62} & C_{63} & C_{64} & C_{65} & C_{66} \end{array}\right) \\ \text{mixed} \qquad\qquad \text{shear} \end{array} \begin{array}{c} \\ \begin{pmatrix} \epsilon_{xx} \\ \epsilon_{yy} \\ \epsilon_{zz} \\ \hdashline \epsilon_{yz} \\ \epsilon_{zx} \\ \epsilon_{xy} \end{pmatrix} \\ \text{strain} \end{array} \begin{array}{l} \\ \text{compression} \\ \\ \\ \\ \text{shear} \\ \\ \end{array} \tag{5.15}$$

where all 36 elastic constants are independent. However, in cubic crystals, x, y and z are identical by symmetry therefore $C_{11} = C_{22} = C_{33}$, $C_{12} = C_{21} = C_{23} = C_{32} = C_{13} = C_{31}$, and $C_{44} = C_{55} = C_{66}$. Furthermore, the off diagonal shear components are zero, i.e. $C_{45} = C_{54} = C_{56} = C_{65} = C_{46} = C_{64} = 0$, and mixed compression/shear coupling does not occur, i.e. $C_{14} = C_{41} = ... = 0$. The cubic elasticity matrix now has the form

$$\begin{array}{c} \\ \begin{pmatrix} \sigma_{xx} \\ \sigma_{yy} \\ \sigma_{zz} \\ \hdashline \sigma_{yz} \\ \sigma_{zx} \\ \sigma_{xy} \end{pmatrix} \\ \text{stress} \end{array} = \begin{array}{c} \overbrace{\qquad\qquad}^{\text{compression}} \quad \overbrace{\qquad\qquad}^{\text{mixed}} \\ \left(\begin{array}{ccc:ccc} C_{11} & C_{12} & C_{12} & & & \\ C_{12} & C_{11} & C_{12} & & 0 & \\ C_{12} & C_{12} & C_{11} & & & \\ \hdashline & & & C_{44} & 0 & 0 \\ & 0 & & 0 & C_{44} & 0 \\ & & & 0 & 0 & C_{44} \end{array}\right) \\ \text{mixed} \qquad\qquad \text{shear} \end{array} \begin{array}{c} \\ \begin{pmatrix} \epsilon_{xx} \\ \epsilon_{yy} \\ \epsilon_{zz} \\ \hdashline \epsilon_{yz} \\ \epsilon_{zx} \\ \epsilon_{xy} \end{pmatrix} \\ \text{strain} \end{array} \begin{array}{l} \\ \text{compression} \\ \\ \\ \\ \text{shear} \\ \\ \end{array} \tag{5.16}$$

For a cubic crystal, like barium nitrate, there are only three independent elastic constants (C_{11}, C_{12}, C_{44}), see figure 5.12. C_{11} is the *longitudinal compression*

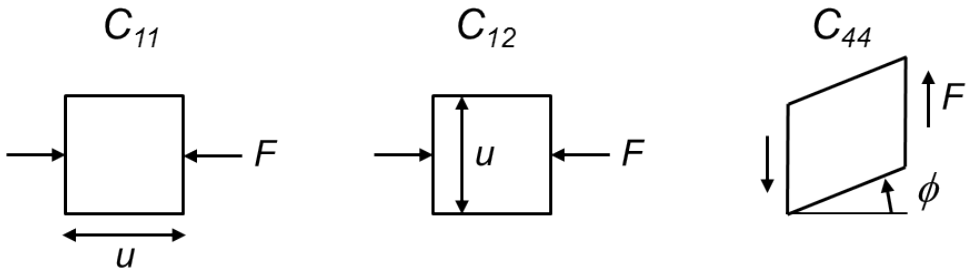

Figure 5.12: The elastic constants for a fcc structure.

(Young's modulus),

$$C_{11} = \frac{\sigma_{xx}}{\epsilon_{xx}} = \frac{F/A}{u/L}$$

C_{12} is the *transverse expansion*,

$$C_{12} = \frac{\sigma_{xx}}{\epsilon_{yy}}$$

and C_{44} is the *shear modulus*,

$$C_{44} = \frac{\sigma_{xy}}{\epsilon_{yy}} = \frac{F/A}{\phi}.$$

A simple test to see whether the elastic constants for cubic materials are mechanically stable is if the conditions

$$B > 0,$$

$$C_{11} - C_{12} > 0,$$

$$C_{44} > 0,$$

are all satisfied.

5.5.2 Temperature dependence

Elastic constants are temperature dependent and therefore consideration is required when comparing computational results with experimental data. Figure

3.1 and 3.2 show the temperature dependence of barium nitrate for a range of 4–300 K. Typically, phonon zero-point and thermal effects that are usually present in experimental data are absent for theoretical DFT calculations. A proposed way around this is to extrapolate experimental data to zero temperature and then subtract the zero-point contribution, yielding a value that is directly comparable to calculated *ab initio* results [74]. The extrapolated values of C_{11}, C_{12} and C_{44} are 36, 25 and 15 GPa, respectively. All experimental data referenced in this work have the temperature given when possible.

5.5.3 The energy-strain method

The first approach outlined in this study is the *energy-strain* method. This has been used successfully to calculate the elastic constants of a large range of materials, such as Ni_3Al [79] and Al−Li compounds [80]. The elastic constants for a cubic structure can be determined by applying two independent volume conserving strains and, as the name suggests, calculating the energy as a function of specific lattice strains (typically ±5 %). A benefit of using a volume conserving strain to determine the elastic constants using DFT is that it reduces errors that may arise from differences in volume.

To calculate $C_{11}-C_{12}$, for a cubic structure, the volume-conserving orthorhombic strain tensor is used,

$$\epsilon = \begin{pmatrix} 1+\delta & 0 & 0 \\ 0 & 1-\delta & 0 \\ 0 & 0 & 1+\frac{\delta^2}{1-\delta^2} \end{pmatrix} \tag{5.17}$$

which comprises a dimensionless relative strain δ, leading to the changes

$$a = a_0(1+\delta),$$

$$b = b_0(1-\delta),$$
$$c = c_0(1+\frac{\delta^2}{1-\delta^2})$$

where a_0, b_0, and c_0 are the lattice parameters for the unstrained cell. The angles remain unchanged, $\alpha = \beta = \gamma = 90°$. The change in the total energy from the unstrained value can be expressed as

$$E(\delta) = E(-\delta) = E(0) + (C_{11} - C_{12})V\delta^2 + O[\delta^4] \tag{5.18}$$

where $E(0)$ is the energy of the unstrained lattice and V is the volume of the unit cell (Note: there are no pressure terms because $\Delta V = 0$.). $C_{11} - C_{12}$ can be determined by taking the differential of $E(\delta)$ against δ^2, calculated via a line of best fit, using the following relationship from equation 5.18,

$$C_{11} - C_{12} = \frac{1}{V}\frac{dE(\delta)}{d\delta^2}. \tag{5.19}$$

To determine the two elastic constants the bulk modulus also needs to be calculated (this is typically done using an equation of state). Equation 5.19 can be solved simultaneously with

$$B = \frac{1}{3}(C_{11} + 2C_{12}) \tag{5.20}$$

to calculate both C_{11} and C_{12}.

For C_{44}, the volume conserving monoclinic strain tensor is used,

$$\epsilon = \begin{pmatrix} 1 & \frac{1}{2}\delta^2 & 0 \\ \frac{1}{2}\delta^2 & 1 & 0 \\ 0 & 0 & 1+\frac{\delta^2}{4-\delta^2} \end{pmatrix} \tag{5.21}$$

which produces the following changes to the lattice parameters and angles

$$a = b = \sqrt{a_0^2 + a_0^2 \frac{\delta^2}{4}}, \tag{5.22}$$

$$c = a_0 \left(1 + \frac{\delta^2}{4 - \delta^2}\right), \tag{5.23}$$

$$\gamma = \arccos\left(\frac{4\delta}{4 + \delta^2}\right). \tag{5.24}$$

Similarly to $C_{11} - C_{12}$, C_{44} is determined by calculating the ground state energy against δ^2 using the relationship

$$E(\delta) = E(-\delta) = E(0) + \frac{1}{2} C_{44} V \delta^2 + O[\delta^4]. \tag{5.25}$$

The relationship between $E(\delta)$ and δ^2 can then be plotted, in which the elastic constant is simply

$$C_{44} = \frac{2}{V} \frac{dE(\delta)}{d\delta^2}. \tag{5.26}$$

The energy-strain calculation procedure

The cutoff energy and k-point spacing used are the same used throughout this study. The initial, unstrained, structure is the geometry optimised structure determined from section 5.3 (in which the results from a given functional are used for the same functional only).

The procedure for calculating the elastic constants using the energy-strain method is as follows: Using P1 symmetry (since applying a strain will break the original symmetry) perform geometry relaxation calculations with fixed lattice constants and angles. Apply the strain (δ) to the system (using equation 5.17 for $C_{11} - C_{12}$ and equation 5.21 for C_{44}), where $\delta = 0.00, 0.01, \ldots, 0.05$. Plot a graph of the difference between strained and unstrained ground state energy

$(E(\delta) - E(0))$ against the applied strain squared (δ^2). Then apply a linear fit, in which the differential $(dE(\delta)/d\delta^2)$ can be substituted into equation 5.19 to calculate $C_{11} - C_{12}$ (or equation 5.26 to calculate C_{44} if using the monoclinic strain tensor).

5.5.4 The stress-strain method

Rather than calculating the ground state electronic energy as a function of strain, it is also possible to use the fundamental stress-strain relationship

$$\sigma = C\epsilon$$

to calculate C as a function of stress. DFT calculations can be used to determine the stress on a system and therefore it is possible to apply a strain, calculate the resulting stress and determine the gradient between the two to get the elastic constant. For a cubic structure, the strain tensor

$$\epsilon = \begin{pmatrix} 1+\delta & 0 & 0 \\ 0 & 1 & \frac{1}{2}\delta \\ 0 & \frac{1}{2}\delta & 1 \end{pmatrix} \tag{5.27}$$

contains all the appropriate strains on a cubic system to allow all three elastic constants (C_{11}, C_{12} and C_{44}) to be determined. The values of strains typically used are δ = -0.003, -0.001, 0.001, 0.003. Therefore, in total 5 relaxation calculations are required; one for the original structure and one for each of the 4 strains applied to the structure. The strain gives the following changes to the lattice constants

$$a = a_0(1+\delta);$$

$$b = c = \sqrt{a_0^2 + a_0^2\frac{\delta^2}{4}};$$

$$\gamma = \arccos\left(\frac{4\delta}{4+\delta^2}\right).$$

The value of stress is plotted against the value of strain for each elastic constant. Where the gradient is simply the elastic constant

$$\frac{d\sigma}{d\epsilon} = C. \tag{5.28}$$

The stress-strain calculation procedure

The procedure for calculating the elastic constants using the stress strain-method is as follows: Apply strain from equation 5.27 with δ = -0.003, -0.001, 0.001, 0.003. Using P1 symmetry (since applying a strain will break the original symmetry) perform geometry optimisation calculations with fixed lattice parameters and angles. Obtain the stress tensor results from the DFT calculations. Plot strain (δ) against stress (ϵ) for C_{11}, C_{12}, C_{44}. Apply a linear fit in which the gradient is the elastic constant (see equation 5.28).

5.5.5 Benchmarking

To increase confidence in the methods described within this section, benchmarking calculations were performed for various structures found within the literature (both experimental and theoretical studies) to investigate consistency and reproducibility. The materials selected for this were Al, Ni_3Al, MgO, and BaO. The elastic constants for a selection of materials can can be found in table 5.6. All the materials chosen have a cubic structure. The plane wave and k-point convergences can be found in Appendix A. The approach used for these convergences are the same used for the nitrates, outlined in section 5.2.

MgO was chosen for the large range of literature available, both experimental and from DFT, performed with both the LDA and PBE functional. The lattice parameter calculated using the PBE functional was within 0.35 % of the

PBE results in the literature and 0.8 % of the available experimental data. The elastic constants in this study with the energy-strain and stress-strain methods are within 2 %, 3 %, and 3 %, for the C_{11}, C_{12}, and C_{44} elastic constants. The strain-stress results in this study compared to the stress-strain data in the literature are within 4 %, 4.1 %, and 5 %, for C_{11}, C_{12}, and C_{44}, respectively. The LDA functional has similar agreements compared to other studies using the LDA functional. Available experimental data for the elastic constants of MgO has also been included, with the temperature and lattice constants given when available. Data for the temperatures of 80 K and 298 K are available. However, the data was deemed insufficient to allow a meaningful attempt to extrapolate the data to 0 K (furthermore, the inclusion of a zero-point energy correction has also been neglected). Nonetheless, to get a *feel* for the difference between the experimental data and DFT calculations a comparison of all the data in this study and the experimental data at 80 K was made and all the *ab initio* values are within 8.5 %, 4.5 %, and 8.6 %, for the C_{11}, C_{12}, and C_{44} elastic constants. In this particular case, the stress-strain method with the PBE functional had the least agreement with the experimental data for all given elastic constants. The LDA functional, for all studies considered, estimated values closer the experimental data for MgO, than the PBE functional.

Extensive step by step calculations of the elastic constants of Ni_3Al have been published using the energy-volume method [79]. Unfortunately, the DFT code and convergence tolerances and method of wavefunction description is not available, so a detailed comparison of their energy-strain results and the energy-strain results performed in this study is not possible. However, the lattice constant calculated in this study is within 0.2 % of theirs, are within 8 %, 5 %, and 1.5 %, for C_{11}, C_{12}, and C_{44}, respectively. The stress-strain and energy-strain calculations performed in this study used the same structures, plane wave cutoff energies, and k-point sampling, where the only variable is the method used. The percent differences for C_{11}, C_{12}, and C_{44} elastic constants are within 2.5 %, 5.5 %, and

2.5 %, respectively.

Due to the lack of literature for BaO only the stress-strain method with the PBE method was conducted. The interatomic potentials were fitted with the experimental data so it is expected to be consistent. However it is interesting to note the disagreement with the C_{44} which differs by 26 % (in this instance the stress-strain PBE data seemingly estimates the experimental value perfectly). a_0 was within 1.4 % whereas C_{11}, C_{12}, and C_{44} where within 5.2 %, 13.5 %, and 8.7 %, respectively.

Finally, Al was also investigated due to the large amount of available data in the literature, with a particular interest to see how the LDA functional compares with the PBE functional. As is consistent with general expectations, the PBE functional estimates a greater lattice constant compared with the LDA. Unfortunately, the experimental elastic constant results were not presented with the lattice constants used. However, values were extrapolated to 0 K by both authors of the respective studies and are included here. The two sets of extrapolated data for Al at 0 K differ by up to 15 %, 9.5 %, and 2.5 %, for C_{11}, C_{12}, and C_{44}, respectively. The method of extrapolation and whether or not any sort of corrections or whether any metallic phenomena of Al occur or were included were not stated in the studies. However the aim of this discussion is just to consider the level of consistencies between studies on what is an arguably simple structure.

The practice of benchmarking within this study has highlighted a number of considerations that provide insight into the reliability and quality of DFT calculations. The reproducibility of DFT data has been touched upon. Despite the large number of different assumptions, within different codes, and the different ways these codes perform DFT calculations, results can still be relatively consistent.

Table 5.6: The elastic constants (GPa) for a selection of materials, where a_0 (Å) is the lattice constant, and *SS* and *ES* indicate the stress-strain and energy-strain methods, respectively. For DFT calculations, the *xc* functionals are given in parentheses. For experimental data, the temperature (K) is given when available.

Material	Method	a_0	C_{11}	C_{12}	C_{44}	Ref.
Al						
	SS (PBE)	4.035	117.5	58.6	39.2	
	(PBE)		110.2	54.8	30.4	[81]
	(PBE)		110.5	58.0	31.1	[82]
	SS (LDA)	3.976	132.1	62.1	43.1	
	(LDA)	3.95	124	65.2	45.5	[83]
	(LDA)	3.99	121±2	63±1	33±5	[84]
	(LDA)	4.05	100±3	50±2	31±1	[84]
	exp. (0 K)*		123	70.8	30.9	[85]
	exp. (293.2 K)		112.9	66.5	27.83	[85]
	exp. (0 K)†		114.3	61.9	31.6	[86]
	exp. (300 K)		106.8	60.7	28.2	[86]
MgO						
	SS (PBE)	4.245	269.5	89.5	143.3	
	ES (PBE)	4.245	274.0	86.9	143.7	
	SS (PBE)‡	4.231	276	86	149	[87]
	SS (PBE)‡	4.251	279.9	90.9	136.7	[88]
	ES (GGA)**	4.237	279	93	146	[89]
	SS (LDA)	4.204	272.1	85.6	148.6	
	ES (LDA)	4.204	277.1	83.1	149.1	
	SS (LDA)	4.231	291	92	156	[87]
	SS (LDA)	4.251	291	91	139	[90]
	exp. (298 K)		297.1	95.4	156.1	[91]
	exp. (80 K)		298.7	85.6	156.7	[92]
	exp. (300 K)		289.3	87.7	154.8	[92]
	exp.	4.213	294	93	155	[87]
BaO						
	SS (PBE)	5.610	119.6	42.3	36.6	
	exp.	5.534	124.4-126.1	48.69-50.03	33.68	[93]
	MD††	5.54	126.30	49.20	49.40	[94]
Ni_3Al						
	SS (PBE)	3.576	260.9	140.9	127.43	
	ES (PBE)	3.576	255.1	148.9	130.48	
	ES	3.569	243.1	155.9	131.9	[79]

* Extrapolated from measurements between 773 K and 63 K
† Extrapolated from measurements carried out down to 4 K
‡ DFT calcualtions performed using VASP
** Specific type of GGA not specified
†† Molecular dynamics (MD)

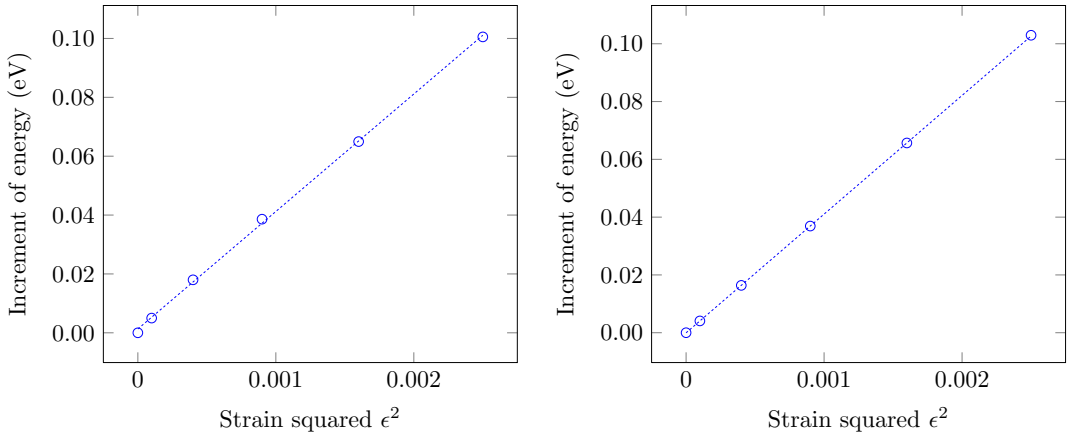

(a) $C_{11} - C_{12}$ (b) C_{44}

Figure 5.13: Calculated energy as a function of applied strain squared, for $C_{11} - C_{12}$ and C_{44}, for $Ba(NO_3)_2$.

5.5.6 Results: barium and strontium nitrate

The unstrained starting structure for the elastic constants calculations are the refined structures shown in table 5.3, all with $Pa3$ symmetry, and lattice constants (a_0) of 8.277 Å, 8.136 Å, and 7.925 Å for the PBE, WC, and LDA functionals, respectively. Identical plane wave cutoff energies and k-point grid spacings were used throughout all calculations.

The $Ba(NO_3)_2$ energy-strain results for $C_{11} - C_{12}$ and C_{44} can be found in figures 5.13a and 5.13b, respectively. Whereas, the equivalent results for $Sr(NO_3)_2$ are shown in figures 5.14a and 5.14b. Graphs of the stress-strain results for $Ba(NO_3)_2$ and $Sr(NO_3)_2$ can be seen in figures 5.15 and 5.16, respectively. Similarly to the energy-strain method, deviations from the linear fits can be seen for all stress-strain graphs, however, they also all fall within the convergence tolerances of the relaxation calculations.

The calculated elastic constants for $Ba(NO_3)_2$ and $Sr(NO_3)_2$ can be seen in table 5.7, alongside experimental data from the literature [77], in which the elastic constants were calculated via the ultrasonic pulse superposition method. For both $Ba(NO_3)_2$ and $Sr(NO_3)_2$, the energy-strain and stress-strain results are compared

by first considering the difference between $C_{11} - C_{12}$ for the two methods. With regards to $Ba(NO_3)_2$, the difference is within 28.5 %, whereas for $Sr(NO_3)_2$ the difference is within 25 %. These are rather large, however when using B (taken from 5.4) to separate C_{11} and C_{12} for the energy-strain results and then comparing them to the stress-strain method individually produces differences of 1.5 % and 11 % for C_{11} and C_{12}, respectively, for $Ba(NO_3)_2$. As for $Sr(NO_3)_2$, the differences are 5.2 % and 6.2 % for C_{11} and C_{12}, respectively. Similarly to the benchmark calculations in section 5.5.5, the energy-strain and stress-strain results are in good agreement.

The experimental data available ranged from 300 K to approximately 30 K (see figures 3.1 and 3.2). It is clear to see from the graphs that the extrapolation is a rather crude one. However, the figures do highlight the effect temperature has on the elastic constants, showing that they are inversely related to temperature: the elastic constants increase by approximately 23 %, 21 %, and 17.5 % for C_{11}, C_{12}, and C_{44}, respectively, for $Ba(NO_3)_2$ from 294 K to 0 K. Whereas for $Sr(NO_3)_2$, the increases are approximately 15 %, 13 %, and 19.5 %, for C_{11}, C_{12}, and C_{44}, respectively.

5.5.7 Discussion

A useful quirk of both methods is that the elastic constants are determined from linear fits, which therefore provides preliminary reassurance that the calculations have performed as expected. In figure 5.13a, slight deviations from the line of best fit exists, although the differences are within the tolerances of the relaxation calculations and therefore to be expected.

Contrary to what one may expect, it is interesting to note that the elastic constant estimations are seemingly uncorrelated to the size of lattice constants used, with respect to comparison of the functionals used. Whether or not this is due to the precision, accuracy, or errors, or whether this simply highlights the

differences of the functionals used, has yet to be deduced.

Regardless of the discrepancies of the lattice parameters when comparing lattice parameters and functionals, the elastic properties of $Sr(NO_3)_2$ to $Ba(NO_3)_2$ do reflect the behaviour of the ionic radii

$$\rho_{Sr^{2+}}(1.27\,\text{Å}) < \rho_{Ba^{2+}}(1.43\,\text{Å}) \tag{5.29}$$

in that on a whole, all of the elastic constant estimations for strontium nitrate are larger than their barium nitrate equivalents. The only exception being WC C_{12} which appears to overestimate C_{12} for $Ba(NO_3)_2$ (if one were to expect the value to be between the PBE and LDA estimates) and to underestimate the C_{12} for $Sr(NO_3)_2$ (again, with regards to what one may expect comparing it to the LDA and PBE estimates). Experimental studies show that the thermoelastic properties between $Ba(NO_3)_2$, $Sr(NO_3)_2$, and $Pb(NO_3)_2$ are influenced more by the cationic radius than the electronic structure of the cation [77].

One would expect the elastic constants to be a function of lattice constant, with a smaller lattice constant producing a larger elastic constant. Since the lattice constant increases from LDA to WC to PBE, it may be expected that the elastic constants follow in inverse trend, with LDA estimating the largest value and PBE the smallest. The prediction is satisfied when considering just PBE and LDA, however, C_{12} for WC does not follow this relation.

Michard *et al.* investigated Cauchy's relationship, $\Delta = C_{12} - C_{44}$, and compared the value of Δ for barium, strontium, and lead nitrate [17]. A *weak* value for barium nitrate was deduced, ($\Delta = 13.6$ GPa, 7.8 GPa, and 14.3 GPa for $Sr(NO_3)_2$, $Ba(NO_3)_2$, and $Pb(NO_3)_2$, respectively) with the suggestion that the larger unit cell, and therefore longer $NO_3^- - NO_3^-$ distance, is the reason for the relatively low Δ value. Using the stress-strain in this study, for $Ba(NO_3)_2$ for PBE, WC, and LDA, Δ is 12.33 GPa, 16.69 GPa and 17.24 GPa, respectively. Whereas for $Sr(NO_3)_2$, Δ is 12.42 GPa, 7.28 GPa and 12.89 GPa, respectively. These values

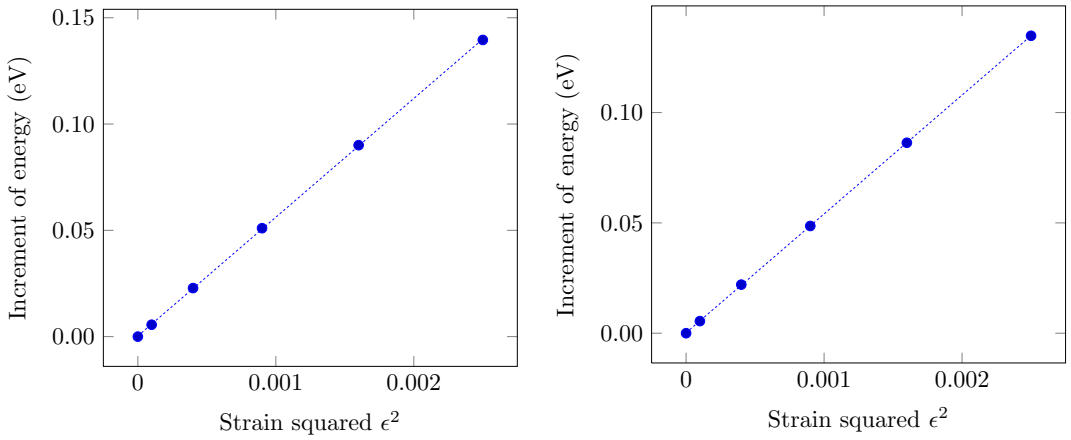

(a) $C_{11} - C_{12}$ (b) C_{44}

Figure 5.14: Calculated energy as a function of applied strain squared, for $C_{11} - C_{12}$ and C_{44}, for $Sr(NO_3)_2$.

are not consistent with the *weak* $Ba(NO_3)_2$ Δ findings within the literature.

5.6 Conclusions

In this chapter *ab initio* relaxation calculations were performed to determine the crystal structure of $Ba(NO_3)_2$, $Sr(NO_3)_2$, $Ca(NO_3)_2$, and $Pb(NO_3)_2$, using the PBE, WC, and LDA functionals. The results were compared alongside data within the literature and the refined structures of $Ba(NO_3)_2$ and $Sr(NO_3)_2$ were then used for *ab initio* bulk modulus and elastic constants calculations. The results of which, were show to be in good agreement with experimental results from the literature. It has been shown that *ab initio* DFT calculations can determine the structure of divalent nitrates that are in agreement with computational results. Furthermore, DFT calculations have calculated the elastic moduli of said divalent nitrates with agreeable results to experimental methods. This shows that DFT is a reliable tool for similar calculations but for mixed nitrates (such as $Ba_xSr_{1-x}(NO_3)_2$), which will be the focus of the following chapter.

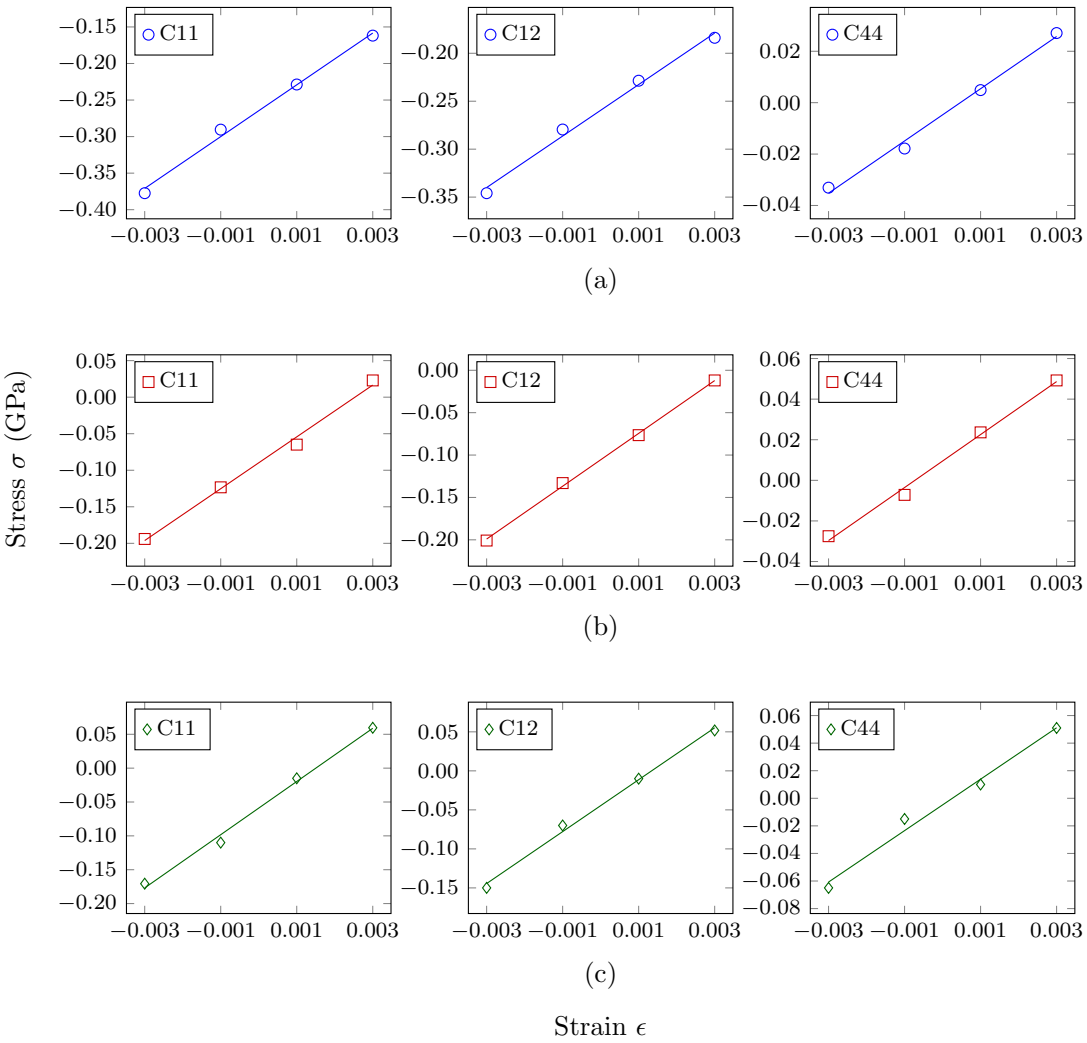

Figure 5.15: The C_{11}, C_{12}, and C_{44} of $Ba(NO_3)_2$ elastic constants calculated using the stress-strain method. Where (a) is the GGA PBE functional, (b) the GGA WC functional, and (c) is the LDA functional.

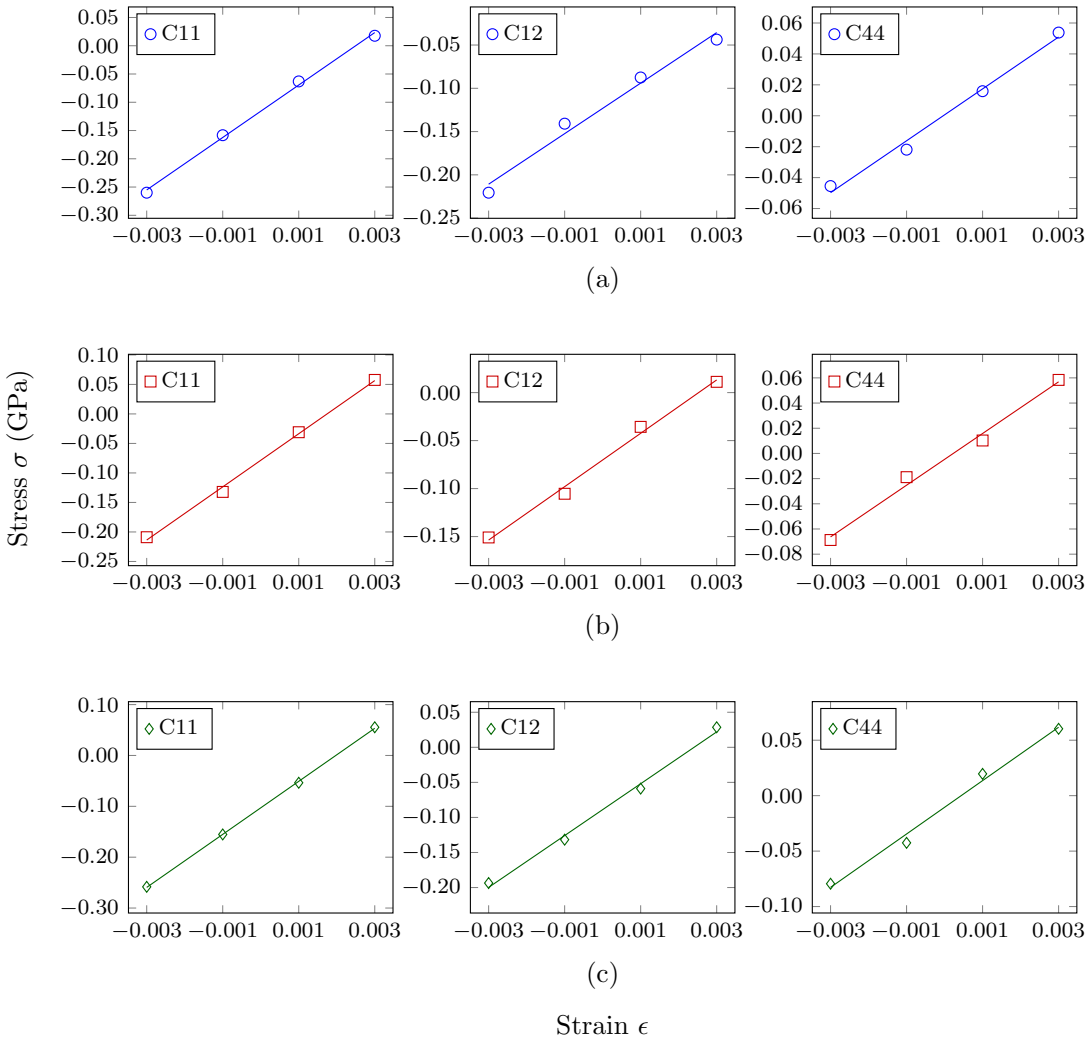

Figure 5.16: The C_{11}, C_{12}, and C_{44} of $Sr(NO_3)_2$ elastic constants calculated using the stress-strain method. Where (a) is the GGA PBE functional, (b) the GGA WC functional, and (c) is the LDA functional.

Table 5.7: Calculated elastic moduli (GPa) for $Ba(NO_3)_2$ and $Sr(NO_3)_2$, using the energy-strain (ES) and stress-strain (SS) methods, alongside experimental data for both 293 K and 0 K (extrapolated). Where a_0 is given in Å ([a] Ref. [65], [b] Ref. [77]).

Material	Method	Functional	a_0	C_{11}	C_{12}	C_{44}	B
$Ba(NO_3)_2$							
	ES	PBE	8.277	34.94	23.93	11.60	27.26†
	SS	PBE	8.277	35.42	26.85	10.16	29.71‡
	SS	WC	8.136	35.46	31.16	13.92	32.59‡
	SS	LDA	7.925	39.29	33.15	18.62	35.20‡
	exp.[a] (0 K)*			36	25	15	29
	exp.[a] (298 K)		8.11	29.21	20.57	12.82	
	exp.[b] (293 K)			29.25	20.65	12.77	23.52
$Sr(NO_3)_2$							
	ES	PBE	7.911	44.02	31.00	15.20	29.52†
	SS	PBE	7.911	46.40	29.20	16.78	34.93‡
	SS	WC	7.767	45.03	27.81	20.53	33.55‡
	SS	LDA	7.547	52.14	36.96	24.07	42.02‡
	exp.[a] (0 K)*			49	33	19	38
	exp.[a] (298 K)			42.81	29.46	15.84	
	exp.[b] (293 K)		7.7798	42.55	29.21	15.90	33.66

* extrapolated from data range 4-300 K
† calculated using EOS from equation 5.5
‡ calculated from C_{11} and C_{12} from equation 5.20

Chapter 6

Solid solutions

6.1 Introduction

This chapter covers all the DFT calculations relative to the $Ba_xSr_{1-x}(NO_3)_2$ complex, as well as including $Ba_xCa_{1-x}(NO_3)_2$ for comparison. The cohesive energy for $Ba(NO_3)_2$, $Sr(NO_3)_2$, and $Ca(NO_3)_2$ were first calculated. Then the formation energy of various point defects within the barium nitrate structure were calculated. The effect of the composition of $Ba_xSr_{1-x}(NO_3)_2$ on the lattice parameter, and atomic position, were also investigated. This was done using the unit cell at concentrations of $x = 0.25$ ranging from $0 - 1$. Following this, the thermodynamics of the complex were investigated with properties such as Gibbs free energy and mixing enthalpy calculated, leading to the $T-x$ phase diagram.

6.2 Cohesive energy

The cohesive energy (also known as the atomisation energy) of a crystal is defined as the energy required to separate a crystal at equilibrium into neutral free atoms at rest, at infinite separation, with the same electronic configuration, at 0 K [86]. To clarify the difference, the cohesive *enthalpy* includes the additional energy to

Table 6.1: Taken from the CRC handbook, thermodynamic properties of ions and neutral species in aqueous solution [96].

Species	$\Delta_f H^\circ$ (kJ mol^{-1})	$\Delta_f G^\circ$ (kJ mol^{-1})	S° (kJ mol^{-1} K^{-1})	C_p (kJ mol^{-1} K^{-1})
Ba^{2+}	-537.6	-560.8	9.6	
Sr^{2+}	-545.8	-559.5	-32.6	
NO_3^-	-207.4	111.3	146.4	-86.6
$Ba(NO_3)_2$	-942.4	-783.3	302.5	
$Sr(NO_3)_2$	-960.5	-782.0	260.2	

convert the materials of interest at desired temperatures, such as 298 K. Finally, lattice potential energy of an ionic solid is the total energy required to separate a solid to form independent gaseous ions. It is important to be careful when defining reference states and comparing experimental to *ab initio* data, as it has been shown that there has been much confusion between cohesive energy and enthalpy throughout the literature, particularly when comparisons are made between empirical and *ab initio* studies [95].

The results presented in this chapter will all be of the cohesive energy, but they will be compared with experimental data accordingly (table 6.1 shows published experimental enthalpies for the nitrates of interest). The cohesive energy E_{coh} can be expressed as

$$E_{\text{coh}} = E_{\text{solid}} - \sum_{\text{A}} E_{\text{A}}^{\text{isolated}} \tag{6.1}$$

where E_{solid} is the energy of the solid material and $E_{\text{A}}^{\text{isolated}}$ is the energy of an individual atom A at ground state. Calculating a material's cohesive energy can subsequently provide information on the most likely crystal structure a solid will adopt, which is the system with the lowest energy and therefore the highest E_{coh}.

6.2.1 Methodology

Periodic boundary conditions are inherent within the CASTEP code, therefore in order to determine the energy of an isolated atom, boundary effects need to be

Table 6.2: Calculated cohesive energies (eV) for divalent metal nitrates. Experimental results taken from [96].

Material	PBE	WC	LDA	exp.
$Ba(NO_3)_2$	19.62	20.49	21.21	20.49
$Sr(NO_3)_2$	19.48	20.46	21.66	21.70
$Ca(NO_3)_2$	19.43	20.20	21.69	21.44

carefully catered for. The isolated atom is placed in the centre of a cubic supercell, with lattice parameter a. To eliminate any interference from the atom's periodic image, finite energy calculations are performed across increasing cell sizes until the change in energy converges within a chosen tolerance. It is then possible to extrapolate the data to $a \to \infty$. The bulk material results are taken from section 5.3. Appropriate plane wave cutoff energies and k-point sampling calculations were performed before the calculations, in accordance to section 5.2.

6.2.2 Results and discussion

The change in energy as a function of supercell size for the isolated atoms of Ba, Sr, N, and O can be found in figure 6.1. All atoms converged within 1 meV/atom with a supercell of 14 Å. The calulated cohesive energies of $Ba(NO_3)_2$, $Sr(NO_3)_2$, and $Ca(NO_3)_2$ can be found in table 6.2, along with experimental results for comparison.

The overbinding of LDA is evident in the results, with it producing the largest cohesive energy for all nitrates. What is also interesting is that both the GGA functionals estimate increasing cohesive energies as ionic radii increase, Ca > Sr > Ba. Whereas LDA shows the opposite trend but with larger differences between the materials. This may be due to the larger electron density gradient present in $Ca(NO_3)_2$ due to the atoms being closer together.

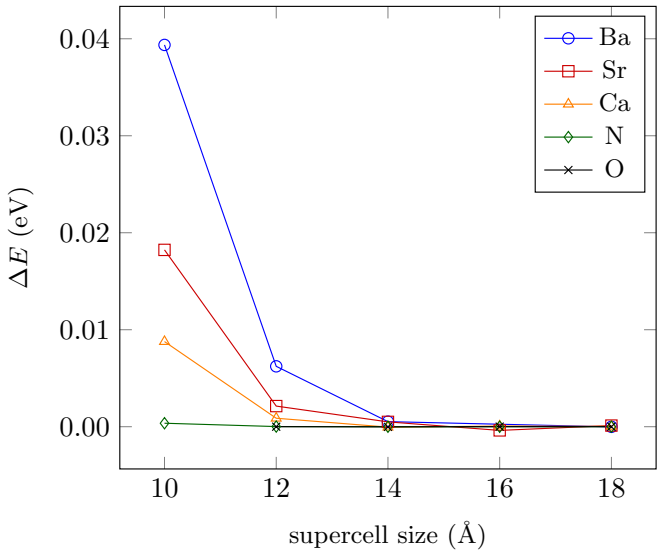

Figure 6.1: The change in energy (ΔE) between successive total energy calculations of a single atom in a cubic supercell. Calculated with the WC functional.

6.3 Point defects of $Ba(NO_3)_2$

Defects can play a major role in a material's properties and have been studied using DFT across a broad range of applications. The main types of point defects can be found in figure 6.2. With regards to $Ba(NO_3)_2$, only the cationic substitution and vacancy defects will be studied in this body of work. Specifically, the defect formation energy of single cationic substitution was calculated for both Sr^{2+} and Ca^{2+}, as well as for a Ba^{2+} neutral vacancy.

There is much greater scope for work if surface adsorptions are considered as well as edge effects and defect diffusion. However, these are beyond the scope of this current report, which will focus on defects within bulk materials.

6.3.1 Defect formation energy

The defect formation energy E_f of a crystal is defined as

$$E_f = E_{\text{defect}} - E_0 + \sum_i n_i \mu_i - q(\epsilon_v + \epsilon_F) \tag{6.2}$$

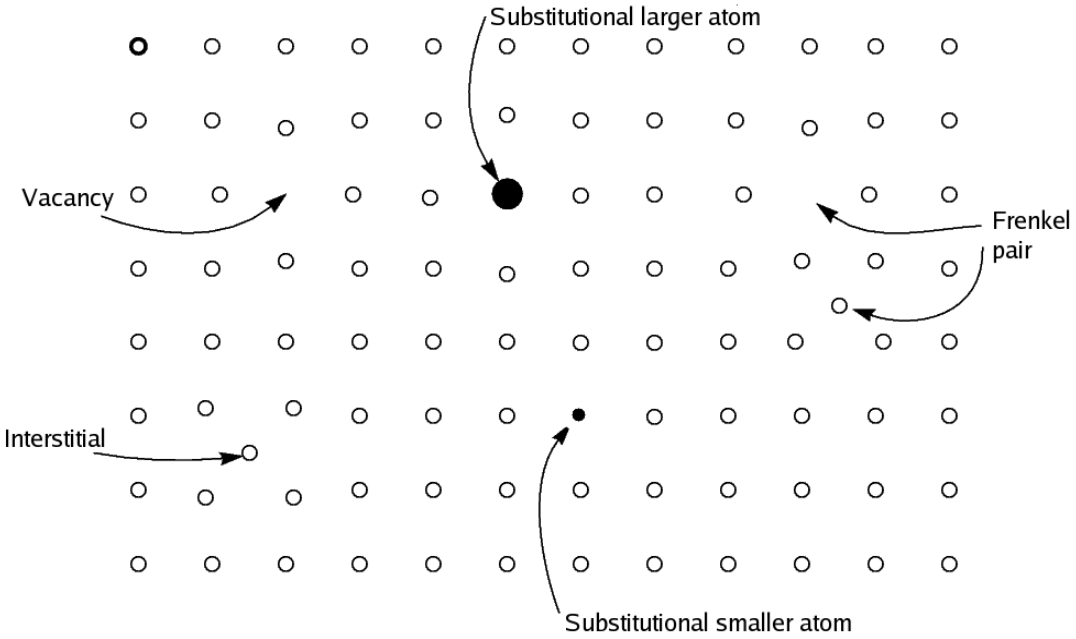

Figure 6.2: Schematic of the main types of point defects (taken from [97]).

where E_{defect} is the total energy of the crystal with the defect, E_0 is the total energy of the pure crystal without a defect, and n_i is the number of particles, of species i, added or removed from the supercell to make the defect. For atoms removed $n_i < 0$, whereas for atoms added $n_i > 0$. Furthermore, μ_i is the chemical potential of the particle reservoir of species i, and ϵ_F is the Fermi level, referenced to the valence-band maximum ϵ_v in the bulk. Finally, q represents the charge state of the created defect (if one electron is removed, $q = +1$; if one electron is added, $q =$ -1, etc).

The defects of interest in this work are neutral vacancies and cationic substitutions (e.g. one Ba^{2+} substituted with one Sr^{2+}) which also produce neutral defects, therefore $q = 0$ is used for all calculations throughout this work. Following from equation 6.2, we now have the neutral defect formation energy in a supercell, defined as

$$E_f = E_{\text{defect}} - E_0 + \sum_i n_i \mu_i. \tag{6.3}$$

Specifically, with regards to a single cation substitution of Ba^{2+} with Sr^{2+}, the

equation reduces to

$$E_f = E_{\text{defect } Ba(NO_3)_2} - E_{\text{pure } Ba(NO_3)_2} + \mu_{Sr} - \mu_{Ba}. \tag{6.4}$$

Chemical potentials

The next important step is defining what the chemical potentials μ_{Sr} and μ_{Ba} actually are, which is a non-trivial consideration. With regards to experimental work, elementary phases at standard conditions are usually employed (temperature = 273.15 or 298.15 K, and pressure = 100 or 101.325 kPa). Typically, in electronic structure calculations, the chemical potentials are referenced to the total energy of the elementary phases at T = 0 K, often neglecting zero-point vibrational effects [98].

Freysoldt *et al.* used DFT to investigate charged vacancy defects in GaAs, defining the chemical potential μ_{Ga} as being equal to *that of Ga metal* [99]. Castleton *et al.* calculated defects in InP and GaP and chose the chemical potential (μ_{In}, μ_P, and μ_{Ga}) corresponding to stoichiometric conditions [100]. Li *et al.* performed calculations of vacancy defect formation energies in graphite. In their work, the chemical potential was simply that of carbon and it was taken as *the total energy of graphite* [101]. Sun *et al.* took a more rigorous approach when investigating MoS_2 and calculated the defect formation energies as a function of the chemical potential, in which the range of μ was determined by the *richness* of Mo and S availabilities [102].

In the specific case of the HASTs at Sellafield, the composition of the waste sludge is highly complex due to the range of materials, changing over time due to radioactive decay, and with variations from one tank to the next. A precise description, or estimation, of the chemical composition throughout the HASTs is beyond the scope of this body of work. That being said, the range of conditions investigated were barium and strontium rich environments and oxygen rich.

In this study the chemical potential was deduced in two conditions, in barium

and strontium rich environments, in which

$$\mu_{\mathrm{Ba}} = \mu_{\mathrm{Ba(bulk)}}. \tag{6.5}$$

The other environment is in oxygen rich environments, in which BaO and SrO are used as sources. In this case we have

$$\mu_{\mathrm{BaO(bulk)}} = \mu_{\mathrm{Ba}} + \frac{1}{2}\mu_{\mathrm{O_2(gas)}} \tag{6.6}$$

where $\mu_{\mathrm{BaO(bulk)}}$ is the formula unit energy of BaO solid and $\mu_{\mathrm{O_2(gas)}}$ is the total energy of a O_2 molecule in gaseous form. In oxygen rich environments the value of μ_{Ba} is simple equated as

$$\mu_{\mathrm{Ba}} = \mu_{\mathrm{BaO(bulk)}} - \frac{1}{2}\mu_{\mathrm{O_2(gas)}}. \tag{6.7}$$

For the substitutional defects μ_{Sr} and μ_{Ca} the sources were assumed to be from bulk metal, $\mu_{\mathrm{Sr(bulk)}}$ and $\mu_{\mathrm{Ca(bulk)}}$, respectively.

Kröger-Vink notation [103] will be used to illustrate the defects, where for M_S, M corresponds to the species and S indicates the lattice site that the species occupies. For example, Sr_{Ba} represents a strontium atom on a barium lattice site and V_{Ba} represents a vacancy on a barium lattice site. All defects within this study are neutral so charge notation has been omitted.

6.3.2 Finite size scaling

Now all the terms in the formation energy (equation 6.3) have been defined, the next step is to deduce an appropriate method of calculating them. Calculations of the defect crystal fall victim to the same periodic boundary issues that the isolated particles in a box in the cohesive energy calculations had. Namely, that defect-defect interactions between repeating cells may lead to spurious energy

errors.

One solution to this issue is to incorporate finite size scaling, which is the method of calculating defect formation energies in a range of supercell sizes and then extrapolating the data to an infinity sized supercell. To do this, the same defect formation energy must be calculated for at least three symmetrical, yet varying in the number of atoms, supercells. To then determine what the defect formation energy would be for an infinite sized supercell, a fit as a function of the inverse supercell size must be performed [100].

According to Castleton *et al.* [104], the two main sources of errors of the finite size scaling method are; elastic errors which arise from using a supercell that does not contain all the elastic effects, giving overestimates of the formation energy, and errors which arise from the defect interacting (via both elastic and electrostatic interactions) through an infinite array of spurious images of itself. They claim it is possible to truncate the direct elastic interactions by freezing all atoms lying on the surface of the cell at their ideal lattice positions.

6.3.3 Non-fixed cell shapes

A practical limitation with using finite size scaling methods is that for systems with large unit cells the number of atoms required for successive supercell sizes quickly runs into scaling issues. For the case of barium nitrate, the $1 \times 1 \times 1$ unit cell contains 36 atoms, therefore a $3 \times 3 \times 3$ supercell requires 972 atoms per calculation, which would be a very computationally and time expensive calculation to perform. With this being the case, it was not possible to perform converged $3 \times 3 \times 3$ supercell calculations within the scope of this work. This unfortunately limits the possibility of extrapolating the data. However, Hine *et al.* [105] argued that it is not necessary to restrict calculations to a fixed cell shape. They have shown that using a suitable correction, it is possible to use alternative shapes ($a \neq b \neq c$) to allow access to a much larger range of cells. Table 6.3 shows

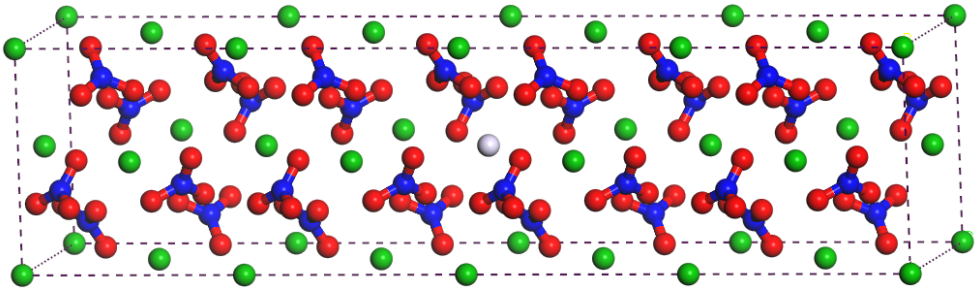

Figure 6.3: Schematc of the defect $4 \times 1 \times 1$ supercell. Where light blue represents the defect atom, green barium, blue nitrogen, and red oxygen.

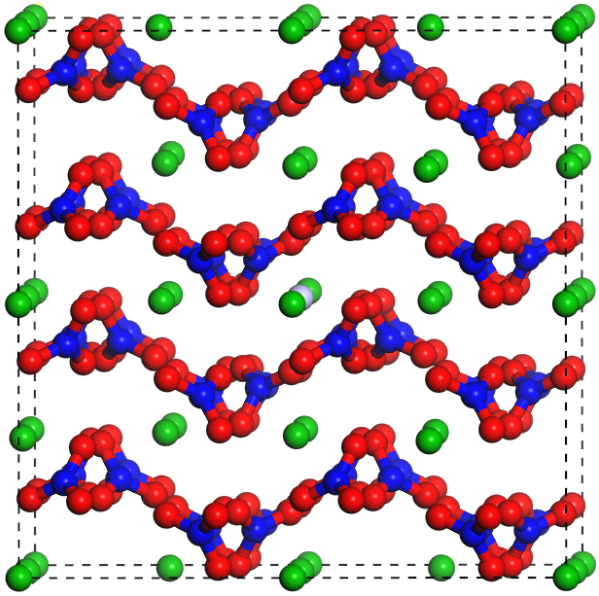

Figure 6.4: Schematic of the defect $2 \times 2 \times 2$ supercell. Where light blue represents the defect, green the barium atoms, blue nitrogen, and red oxygen.

the number of atoms needed for various supercell sizes that could be used for $Ba(NO_3)_2$.

6.3.4 Methodology

For a summary of the number of atoms in a supercell and the corresponding concentrations that can be calculated, see table 6.3. As mentioned previously, the large number of atoms (36) in a unit cell a $3 \times 3 \times 3$ supercell (972 atoms) unfortunately proved to be too large for the available resources within this study.

Table 6.3: Summary of supercell sizes and number of atoms for $Ba_xSr_{1-x}(NO_3)_2$ (and therefore also $Ba_xCa_{1-x}(NO_3)_2$).

Supercell size	No. of molecules	Total no. of atoms	Defect-defect spacing (Å)
$1 \times 1 \times 1$	4	36	8.14
$2 \times 2 \times 2$	32	288	16.27
$3 \times 3 \times 3$	108	972	24.41
$4 \times 4 \times 4$	256	2304	32.54
$2 \times 1 \times 1$	8	72	-
$3 \times 1 \times 1$	12	108	-
$4 \times 1 \times 1$	16	144	-
$2 \times 2 \times 1$	16	144	-
$3 \times 3 \times 1$	36	324	-
$4 \times 4 \times 1$	64	576	-

Therefore, supercells of $2 \times 1 \times 1$, $3 \times 1 \times 1$, and $4 \times 1 \times 1$ were used, along with a $2 \times 2 \times 2$ supercell. Figure 6.3 shows a schematic of the $4 \times 1 \times 1$ supercell.

For the case of a $2 \times 2 \times 2$ $Ba(NO_3)_2$ supercell, the central Ba atom was replaced by a Sr atom (and in another calculation by a Ca atom), as well as simply removed for the vacancy defect. See figure 6.4 for a schematic of this supercell. Defect energies for both the unrelaxed and relaxed structure were calculated, and similar to Castleton *et al.* [100], the atoms located on the boundary of the cell were not allowed to relax.

The same plane wave cutoff energy was used throughout all supercell calculations, in order to take advantage of the cancellation of errors [100]. Similarly, for the k-point sampling, a Monkhorst-Pack grid of $12 \times 12 \times 12$ was used for the unit cell. This satisfied the convergence criteria and also ensured that all supercells could have identical k-point spacing of $0.010\,24\,\text{Å}^{-1}$. For example, the $3 \times 1 \times 1$ cell had a k-point grid of $4 \times 12 \times 12$ which produces $0.010\,24\,\text{Å}^{-1}$ spacing throughout. All calculations were performed using the WC functional, as this was determined to be the most appropriate functional for the materials of interest in this study in chapter 5.

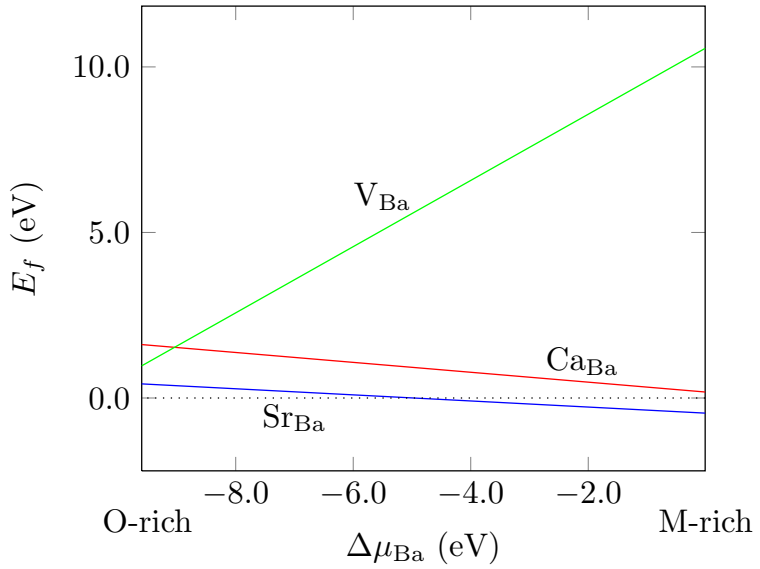

Figure 6.5: Defect formation energies as a function of the change in barium chemical potential, plotted is the range M-rich sources (where M = Ba, Sr, and Ca) and an O-rich source. Calculated using $2 \times 2 \times 2$ supercells.

6.3.5 Results

Figure 6.5 shows the formation energies for Sr_{Ba}, Ca_{Ba}, and V_{Ba} defects in $Ba(NO_3)_2$, calculated using a $2 \times 2 \times 2$ supercell, as a function of $\Delta\mu_{Ba}$. The range of chemical potential is from two conditions; oxygen rich (O-rich) and M-rich (where M = Ba, Sr, and Ca).

Figure 6.6 shows the formation energies calculated using the uneven supercells ($2 \times 1 \times 1$, $3 \times 1 \times 1$, and $4 \times 1 \times 1$). The defect formation energies are all positive which is consistent with the notion that the host crystal would be unstable otherwise. A table of the calculated defect formation energies can be found in table 6.4. It shows the raw data of the formation energy across varying supercell sizes.

Table 6.5 shows the relaxation distances of the atoms surrounding the defects. Both cationic substitution defects replace a barium atom with an atom of smaller ionic radius, therefore it is no surprise that the surrounding atoms relax towards the defect. The neutral vacancy shows a decrease in distance, relative to the pure

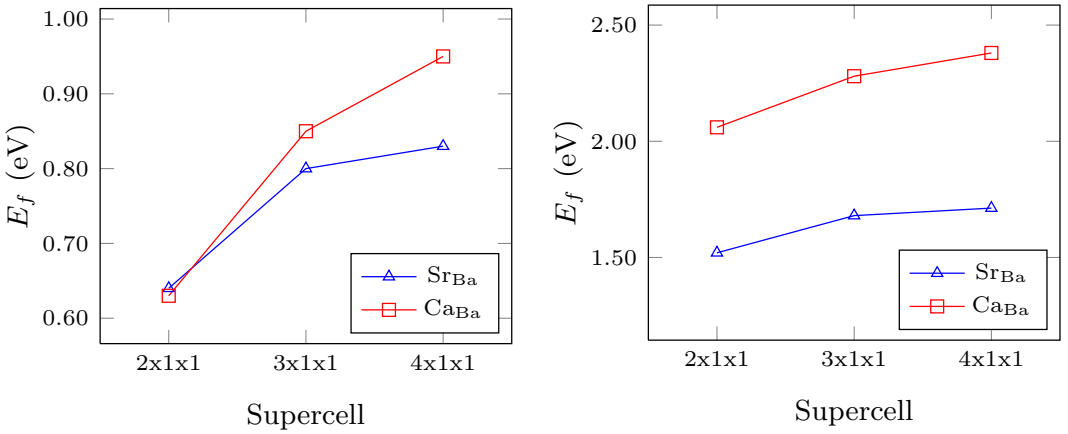

(a) M-rich (b) O-rich

Figure 6.6: Defect formation energies calculated from the non-fixed supercell shapes for cationic substitutions (where M = Ba, Sr, and Ca).

Table 6.4: Formation energy, E_f (eV), for point defects in $Ba(NO_3)_2$, calculated at various supercell sizes.

Defect	supercell size	E_f	
		M-rich	O-rich
Sr_{Ba}	$2 \times 2 \times 2$	-0.46	0.42
	$2 \times 1 \times 1$	0.64	1.52
	$3 \times 1 \times 1$	0.80	1.68
	$4 \times 1 \times 1$	0.83	1.71
Ca_{Ba}	$2 \times 2 \times 2$	0.18	1.61
	$2 \times 1 \times 1$	0.63	2.06
	$3 \times 1 \times 1$	0.85	2.28
	$4 \times 1 \times 1$	0.95	2.38
V_{Ba}	$2 \times 2 \times 2$	10.6	0.97

Table 6.5: Geometry change caused by point defect. Distances given in Å and angles in °, where *nn* stands for nearest neighbours with respect to the defect (2*nn* is next nearest neighbours, and so fourth). M represents the cations and in the case of the vacancy defect M represents the site of the defect.

Atoms	Type	Pure	Defects		
		$Ba(NO_3)_2$	V_{Ba}	Sr_{Ba}	Ca_{Ba}
M−Ba					
	nn	5.75	5.76	5.67	5.67
	2*nn*	5.75	5.80	5.67	5.67
M−N					
	nn	3.33	3.42	3.16	3.10
	2*nn*	4.94	4.91	4.77	4.84
	3*nn*	5.55	5.63	5.61	5.59
	4*nn*	6.65	6.63	6.61	6.64
	furthest	11.10	11.07	11.05	11.14
O−N−O					
	nn a	120.0	121.8	119.9	119.7
	nn b	120.0	119.2	119.9	120.2
	nn c	120.0	119.2	120.2	120.1

structure, for the *nn* and 3*nn*, whereas the 2*nn* and 4*nn* nitrates are actually further away than they are in the pure system.

The O−N−O angles of the *nn* nitrate group are also presented in table 6.5. With respect to the defect atom, the oxygen and nitrogen atoms all lie in the same 2-dimensional plane, in which the elastic effects were contained. For all three point defects, the *nn* O−N−O angles were affected, with a decrease in angle between the two oxygen atoms that are equidistant to the defect for both Sr and Ca. For the vacancy defect the angle between the two oxygen atoms increased. This shows that the oxygen are attracted to the former and repelled from the later. A schematic of the *nn* nitrate to the Sr defect can be seen in figure 6.7.

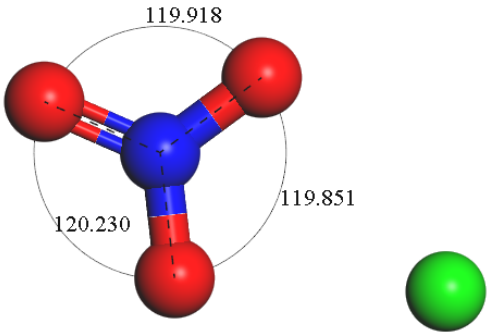

Figure 6.7: Schematic of the nearest NO_3 to the Sr atom defect in a $2\times2\times2$ $Ba(NO_3)_2$ supercell. The nearest two oxygen are equidistant from the strontium.

6.3.6 Discussion

The results calculated in this study give smaller formation energies for structures with a strontium atom than the structure with the calcium defect, in both conditions investigated, which indicates that the synthesis of the former structure is relatively easier. This is likely due to the smaller difference in ion radius between strontium atoms (1.27 Å) and barium atoms (1.43 Å) compared with calcium atoms (1.12 Å) and barium atoms. This is in agreement with similar studies [106; 107] which also found that the relative atomic radii, between the original and the defect atom, is related to the defect formation energy.

Similarly, with respect to the changes in position of the surrounding nitrates, as seen in table 6.4, calcium atoms have a smaller ionic radius than strontium, therefore shorter distances between the defect and surrounding atoms are expected for calcium.

For all defects, all atoms (apart from those fixed at the boundaries) change position during the relaxation calculations and therefore they are affected by the elastic effects of the defect. This means that $2\times2\times2$ supercells are not substantial enough to contain all the elastic effects, and thus the associated errors will need to be considered.

The formation energy for a barium vacancy is 10.6 eV for a barium rich conditions compared with 0.97 eV is the O-rich conditions, which show that the defect

is more favourable in the oxygen rich conditions. The formation energies are relatively small, indicating that the formation of defects is likely to occur. In the case of Sr_{Ba} calculated from the $2 \times 2 \times 2$ supercell, in the M-rich environment, the formation energy is negative which indicates that a strontium defect within $Ba(NO_3)_2$ is energetically more favourable. However, this is not the case for the uneven supercell calculations.

6.4 Mixed nitrates

The following piece of work aims to investigate the properties of $Ba_xSr_{1-x}(NO_3)_2$ and $Ba_xCa_{1-x}(NO_3)_2$. The relationship between the composition of $Ba_xSr_{1-x}(NO_3)_2$ (and also $Ba_xCa_{1-x}(NO_3)_2$) and the lattice parameter of the unit cell was calculated.

6.4.1 Theory

For two compounds, A and B, with identical crystal structures in their pure form, Vegard's law states that, at a constant temperature, the volume of an alloy can be determined from a linear interpolation of the constituent's volume through the equation

$$a_{A_{1-x}B_z} = (1-x)a_A + xa_B \tag{6.8}$$

where $a_{A_xB_{(1-x)}}$ is the lattice parameter of the solution, a_A and a_B are the lattice constants for A and B, respectively. Finally, x is the molar fraction of B in the solution. In reality, Vegard's law is seldom perfectly obeyed, however it usually acts as a good approximation to draw comparison to.

6.4.2 Methodology

The $Ba_xSr_{1-x}(NO_3)_2$ structure was created by replacing a Ba^{2+} ion in the optimised $Ba(NO_3)_2$ unit cell with a Sr^{2+} ion. The initial lattice parameter was then

changed assuming Vegard's law is followed. This may not be the fully relaxed, realistic, atomic positioning for the new structure, however with regards to these convergence calculations any error will be negligible.

A single cubic unit cell for $Ba_xSr_{1-x}(NO_3)_2$ contains four molecules, therefore x can only have the value of $x = 0$, 0.25, 0.5, 0.75, and 1. Furthermore, due to the cubic symmetry (x plane = y plane = z plane) the number of unique arrangements for the different compositions is simply one, therefore there are no further considerations required with regards to determining the correct substitution site.

The pure nitrate structures ($x = 0$, 1) are the geometry optimised results from section 5.3 and the preliminary convergence criteria for the plane wave cutoff energy and k-point spacing are as determined in section 5.2.

Calculation procedure

The calculation procedure was as follows: Perform a geometry optimisation for all mixed compositions of $Ba_xSr_{1-x}(NO_3)_2$ achievable with a unit cell ($x = 0.25$, 0.5, 0.75). The substitution of the Sr atoms break the $Pa3$ symmetry, therefore $P1$ symmetry was used. The lattice constants were allowed to relax but set to be consistent with each other (a = b = c). The cell angles where set to be identical ($\alpha = \beta = \gamma = 90°$). The calculations were repeated with increased plane wave cutoff energy and k-point grid to ensure correct convergence.

6.4.3 Benchmarking

Benchmarking calculations were also performed to test how well these calculations reproduce results for similar materials, such as $Ba_xSr_{1-x}O$. The lattice parameter of $Ba_xSr_{1-x}O$ as a function of x was calculated (see figure 6.8a). This is in good agreement with the results published in a study by Ghebouli *et al.* who used similar DFT methodologies (see figure 6.8b) [108]. Both sets of results were based on unit cell calculations, performed using the PBE functional.

6.4.4 Results

See figures 6.9, 6.10, and 6.11 for the lattice parameters for $Ba_xSr_{1-x}(NO_3)_2$ calculated using the PBE, WC, and LDA functionals, respectively. The lattice parameters as a functional of x were also calculated for $Ba_xCa_{1-x}(NO_3)_2$ using the WC functional, which can be seen in figure 6.12.

For $Ba_xSr_{1-x}(NO_3)_2$ both the PBE and WC functionals produced a negative bowing, with respective to Vegard's law, in which the percent differences are all within 0.2 %. Whereas, the LDA functional predicts a near perfect agreement, in which all three lattice constants for $x = 0.25$, 0.5, and 0.75 are within 0.01 %. Experimental results (see figure 3.6) have shown that the lattice parameters of various structures $Ba_xSr_{1-x}(NO_3)_2$ produce values above and below the Vegard's law. This could be explained by imperfections through the grown crystals or due to the miscibility gap which has been show to exist in the $0.3 < x < 0.6$ region, which will be investigated in the following section.

6.4.5 Discussion

Comparing the results for $Ba_xSr_{1-x}(NO_3)_2$ and $Ba_xCa_{1-x}(NO_3)_2$ from WC, both show negative bowing, with the $Ba_xCa_{1-x}(NO_3)_2$ results showing greater departure from the linear fit. This is likely due to the larger difference in sizes of the Ca and Ba cations (compared to Sr and Ba). This is consistent with findings in similar studies of similar structures [108; 109].

Multiple defects

The scope of this study was only with regards to individual point defects. However, to gain a even greater understanding of strontium incorporation in $Ba(NO_3)_2$, multiple defects would be a worthwhile investigation. This would require larger supercells (such as $3\times3\times3$) and greater computational resources. A larger supercell would introduce more options for a greater range of different defect sites for

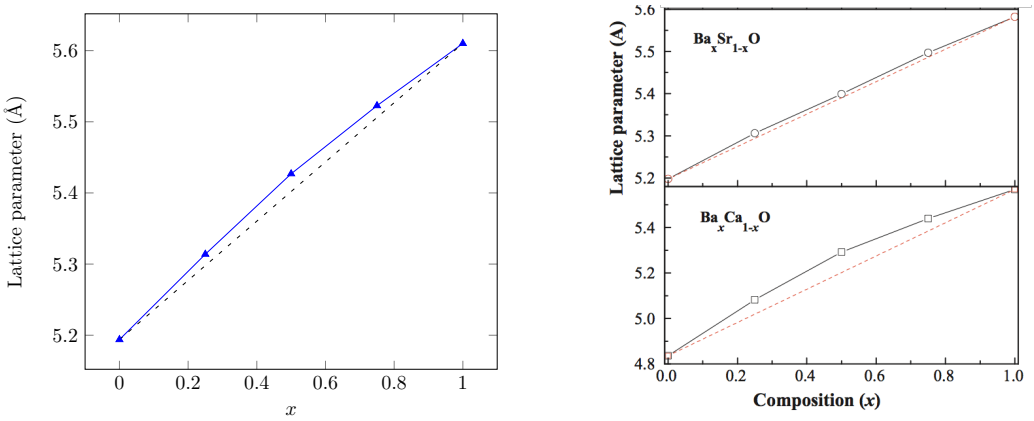

(a) (b)

Figure 6.8: (a) Composition dependency of the lattice parameter for $Ba_xSr_{1-x}O$, compared alongside Vegard's law (dashed line). (b) Taken from [108].

the same value of x. This would allow a wider range of defect arrangements and provide insight into strontium mixing, such as whether it is energetically more favourable for the atoms to clump together or be dispersed evenly throughout the lattice, for example. Furthermore, these calculations could be used to judge the reliability of classical computational methods (such as molecular dynamics (MD)). If the MD calculations were consistent with the DFT results then these could be used for much larger systems to investigate further characteristics of the crystals.

6.5 Thermodynamics

The aim of this piece of work was to determine the thermodynamic properties of $Ba_xSr_{1-x}(NO_3)_2$ and $Ba_xCa_{1-x}(NO_3)_2$, to see which states are the most favourable. The thermodynamics of materials provide information on properties such as phase mixing, which has implications on crystal size and morphology (as discussed in chapter 3). There have been a wealth of studies performed using DFT which again demonstrates the appropriateness of this method for these calculations [108; 110; 109; 111].

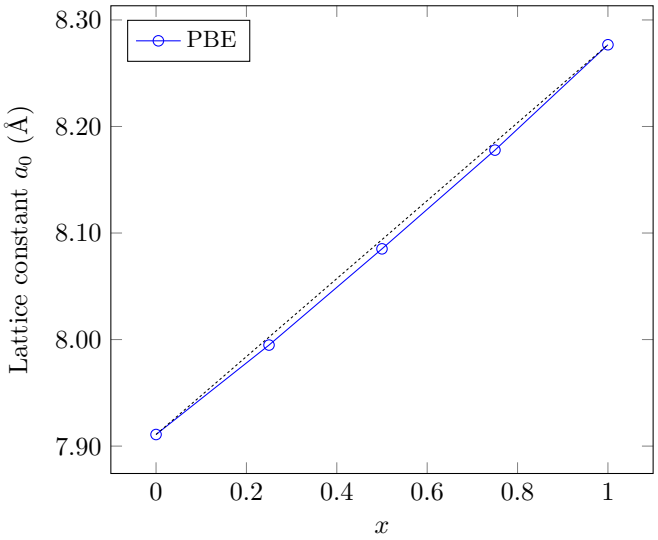

Figure 6.9: Composition dependency of the lattice constant of $Ba_xSr_{1-x}(NO_3)_2$, compared alongside Vegard's law (dashed line). Calculated using the PBE functional.

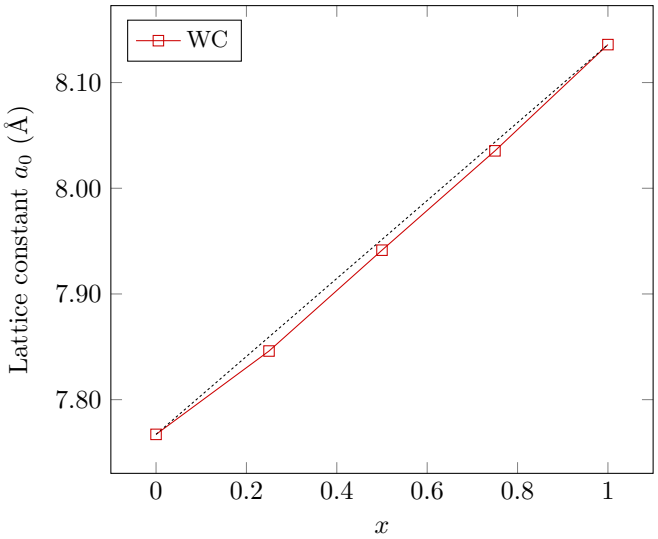

Figure 6.10: Composition dependency of the lattice constant of $Ba_xSr_{1-x}(NO_3)_2$, compared alongside Vegard's law (dashed line). Calculated using the WC functional.

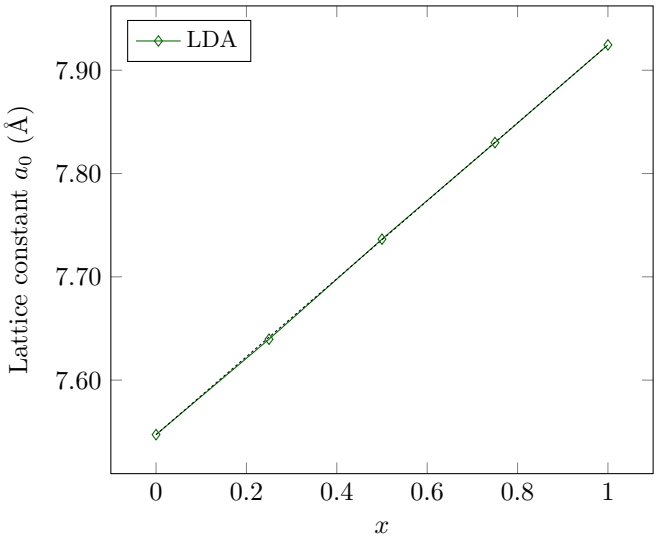

Figure 6.11: Composition dependency of the lattice constant of $Ba_xSr_{1-x}(NO_3)_2$, compared alongside Vegard's law (dashed line). Calculated using the LDA functional.

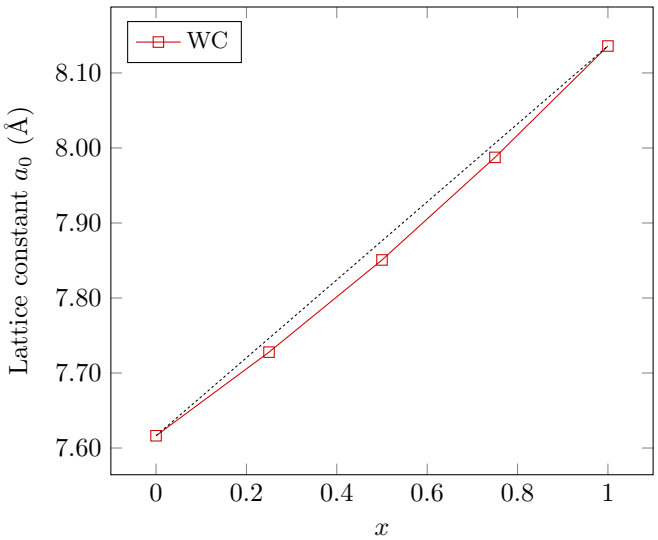

Figure 6.12: Composition dependency of the lattice constant of $Ba_xCa_{1-x}(NO_3)_2$, compared alongside Vegard's law (dashed line). Calculated using the WC functional.

6.5.1 Gibbs free energy

The phase stabilities of the $Ba_xSr_{1-x}(NO_3)_2$ and the $Ba_xCa_{1-x}(NO_3)_2$ solid solutions, at ambient pressure, were determined by use of the Gibbs free energy of mixing. In a regular solution model the Gibbs free energy can be expressed as

$$\Delta G(x,T) = \Delta H(x,T) - T\Delta S(x,T) \tag{6.9}$$

where ΔH is the mixing energy (also known as the formation enthalpy), T is the absolute temperature, and ΔS is the mixing entropy, which can be further expressed as

$$\Delta S = -k_B[x\ln x + (1-x)\ln(1-x)] \tag{6.10}$$

in which k_B is the Boltzmann constant. The mixing energy of $Ba_xSr_{1-x}(NO_3)_2$ can be calculated using the equation

$$\Delta H_{Ba_xSr_{1-x}(NO_3)_2} = E_{Ba_xSr_{1-x}(NO_3)_2} - xE_{Ba(NO_3)_2} - (1-x)E_{Sr(NO_3)_2} \tag{6.11}$$

where $E_{Ba_xSr_{1-x}(NO_3)_2}$ is the total energy per molecule of the mixed nitrate complex, and $E_{Ba(NO_3)_2}$ and $E_{Sr(NO_3)_2}$ are the energy per molecule of $Ba(NO_3)_2$ and $Sr(NO_3)_2$ in the $Pa3$ structure, respectively. The mixing energy can also be expressed as

$$\Delta H = \Omega x(1-x) \tag{6.12}$$

where Ω is the interaction parameter, which depends upon the material and has the form $\Omega = \alpha x + \beta$.

6.5.2 Methodology: phase diagram

The DFT calculations required for this piece are the same used to determine the lattice parameter as a function of x for $Ba_xSr_{1-x}(NO_3)_2$. But rather than being interested in the size of the unit cell we just need the ground state energy.

After calculating the ground state energy for $Ba_xSr_{1-x}(NO_3)_2$ as a function of x, it is possible to determine ΔH by substituting the results into equation 6.11. The values of ΔH can now be plotting as a function of x. A third order polynomial can then be fitted and rearranged to solve

$$\Delta H = (\alpha x + \beta)x(1 - x) \tag{6.13}$$

giving material specific values for the constants α and β. Using the trend for ΔH, and equation 6.12, it is now possible to predict the value of ΔH at any value of x. With regards to ΔS, equation 6.10 can simply be determined by using k_B ($8.6217 \times 10^{-5}\,\mathrm{eV\,K^{-1}}$). With the values for ΔH and ΔS it is then possible to calculate ΔG for any given value of x at a given temperature (T).

The trend of Gibbs free energy as a function of x changes with respect to T. It is possible to use this relationship to extract values for the spinodal and binodal trends of T against x as follows. The spinodal curve can be determined by plotting the values of x that produce $\delta^2(\Delta G)/\delta x^2 = 0$ on the Gibbs free energy plot across a range of temperatures. The binodal curve is determined by deducing the points of common tangent for x on the Gibbs free energy curve across a range of temperatures. The value of the two x values for the T value can be plotted on the $T-x$ graph to get the binodal curve.

6.5.3 Results and discussion

The enthalpy of mixing as a function of x for $Ba_xSr_{1-x}(NO_3)_2$ can be found in figure 6.13. The ΔH curve is asymmetric, being slightly skewed to the lower concentration of Sr, suggesting that concentrations above 0.5 are energetically more favourable.

Figure 6.14 shows the Gibbs free energy as a function of Sr at $T = 400\,\mathrm{K}$. Figure 6.15 shows Gibbs free energy across a range of temperatures. The value of ΔG governs whether mixing will occur or not. In the case of a positive Gibbs

free energy of mixing, the components are immiscible and will result in a two phase dispersion (of a pure A phase and pure B phase mixed together), rather than forming a solution when brought together. Alternatively, in the case of a negative Gibbs free energy of mixing, when the pure components are brought together, they will form a solution, due to the thermodynamic driving force for mixing.

Finally, figure 6.16 shows the $T-x$ phase diagram, with both the spinodal and binodal curves. The formation energies are all positive, which indicates that the systems will have a tendency to segregate into their constituents at low temperatures. The region between the binodal and spinodal curve is where the system becomes metastable and phase separation *can* take place. The spinodal curve marks the equilibrium solubility limit, i.e. the miscibility gap. This is the region in which the system is *unstable*, and phase separation *must* take place.

The critical temperature for $Ba_xSr_{1-x}(NO_3)_2$ was estimated to be 660 K, this value is relatively low (compared to what have been predicted for similar structures such as $Ba_xSr_{1-x}O$ [108]), and suggests that the mixing of $Ba(NO_3)_2$ and $Sr(NO_3)_2$ is not difficult to achieve. For temperatures and compositions above this curve a homogeneous mix is predicted.

6.6 Conclusions

In this chapter, the cohesive energies of $Ba(NO_3)_2$, $Sr(NO_3)_2$, and $Ca(NO_3)_2$ were calculated using *ab initio* DFT methods and were shown to be in good agreement with experimental results. Following this, the defect formation energies were calculated for the point defects Sr_{Ba}, Ca_{Ba}, and V_{Ba} in the barium nitrate crystal. These were determined across a range of conditions, from oxygen-rich to metal-rich, and the results revealed that a strontium defect on a barium site is more favourable than calcium or a barium vacancy.

The lattice parameters of mixed $Ba_xSr_{1-x}(NO_3)_2$ (and $Ba_xCa_{1-x}(NO_3)_2$) were

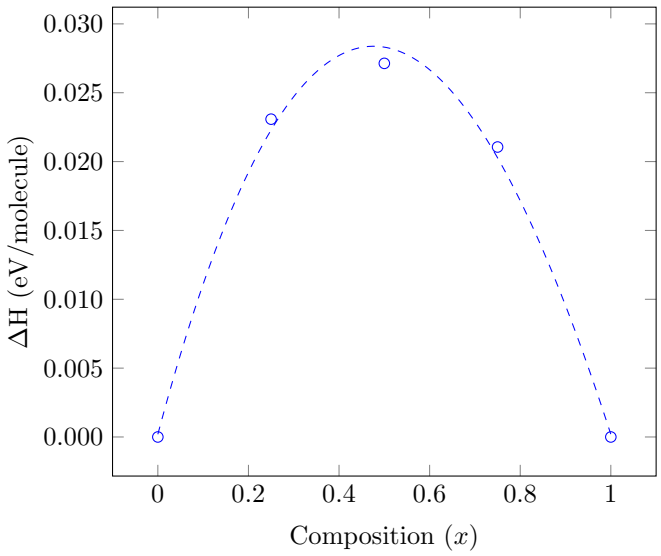

Figure 6.13: The enthalpy of mixing (ΔH) as a function of composition for $Ba_xSr_{1\text{-}x}(NO_3)_2$. Calculated using the WC functional.

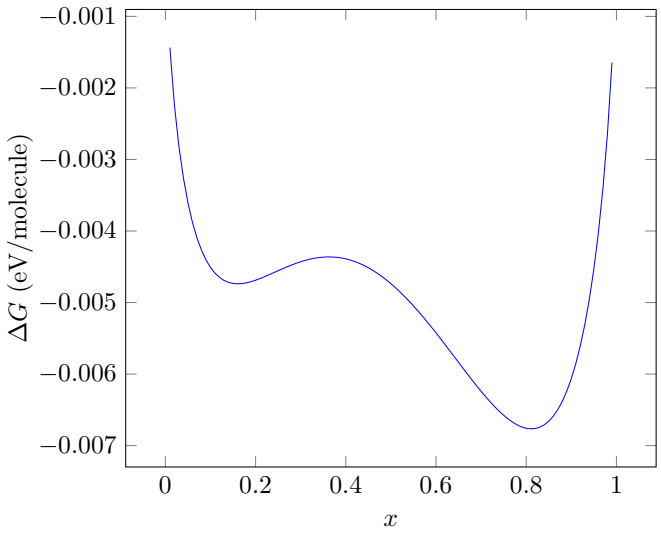

Figure 6.14: Gibbs free energy (ΔG) as a function x for the $Ba_xSr_{1\text{-}x}(NO_3)_2$ complex at $T = 400\,\mathrm{K}$.

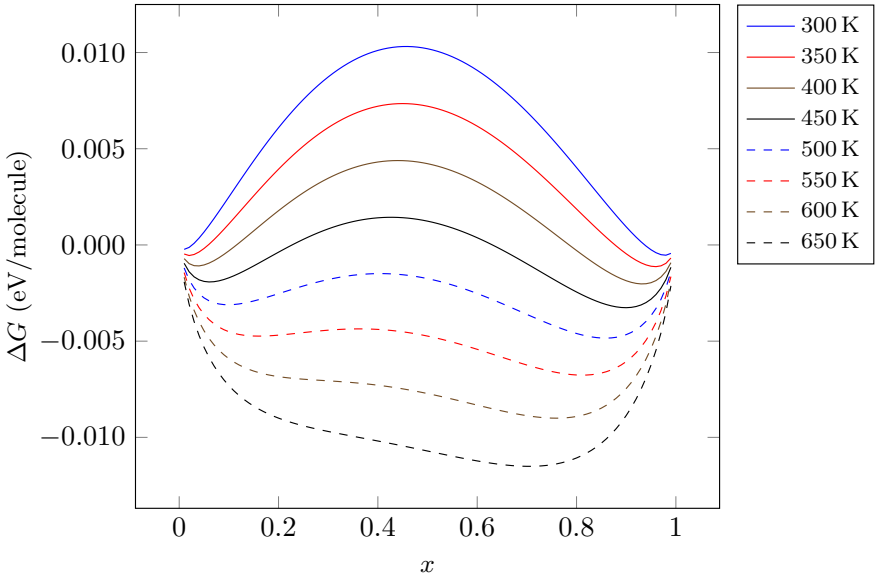

Figure 6.15: Gibbs free energy (ΔG) as a function of x for $Ba_xSr_{1-x}(NO_3)_2$, for temperatures ranging from 300 to 650 K.

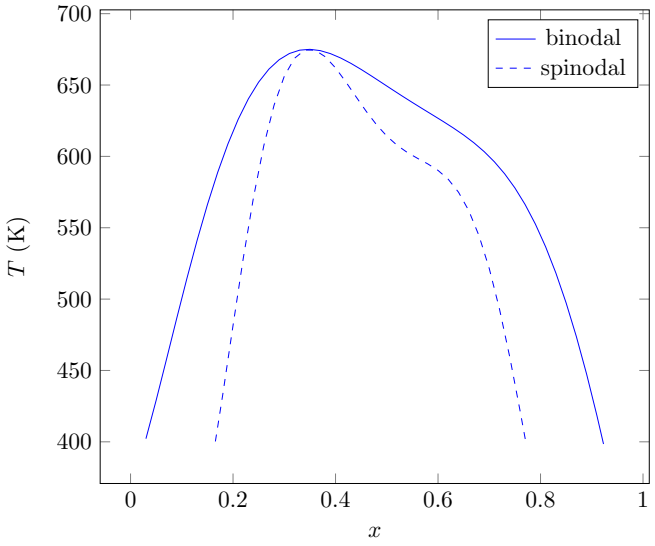

Figure 6.16: Calculated $T-x$ phase diagram of $Ba_xSr_{1-x}(NO_3)_2$, showing both the spinodal and binodal curves.

also calculated, with the results agreeing with experimental results. The lattice constant as a function of composition calculations shows that the WC is more appropriate than the GGA and LDA, which is similar to what Labidi *et al.* found for the $Sr_xCd_{1-x}O$ [112]. The thermodynamics of $Ba_xSr_{1-x}(NO_3)_2$ were investigated by calculating Gibbs free energy and subsequently determining the $T-x$ phase diagram, which in turn shows the range of the miscibility gap and also the critical temperature for $Ba_xSr_{1-x}(NO_3)_2$, which was estimated to be 660 K.

Chapter 7

Interatomic potential fitting

7.1 Introduction

This section will cover and explain the procedure and results for fitting a new interatomic force field for $Ba_xSr_{1-x}(NO_3)_2$. The observables used for the fitting procedure were the *ab initio* results calculated in chapter 5 and chapter 6. The derived interatomic forcefield will allow for calculations to be performed with a significantly larger number of atoms to examine a larger range of mixed phases and atomic arrangements. The emphasis of this potential is firstly fitting to *ab initio* (the benefits of which were discussed in section 4.4.6), but also the introduction of a shell parameter for the oxygen atom which has been proved to improve defect calculations [28]. The fitting, and calculations in the chapter, were all performed using the GULP program.

7.2 Examples in the literature

Many studies have been performed to successfully fit a shell model for titanates such as $BaTiO_3$ and $SrTiO_3$, as well as a shell model fitting of (Ba,Sr)TiO3 for solid solutions, which was done by adding $Sr-O$ interactions to a pre-existing

$BaTiO_3$ force field [113]. Starting with an already developed anisotropic shell model of $BaTiO_3$, which they show is unsuitable for transition temperatures, they developed an isotropic shell model.

7.3 Theory

The basic principles and underlying theory of classical forcefields have been previously discussed in section 4.4. However, the shell model potential will be explained here in further detail.

7.3.1 The shell model

The shell model was first introduced by Dick and Overhauser in 1958 [114]. The idea behind the shell model is that atoms are described as a massive charged core surrounded by a massless charged shell, which are attached by a spring, see figure 7.1. The original expression of the shell model was given as

$$\alpha = \frac{1}{4\pi\epsilon_0}\left(\frac{Y^2}{k}\right) \tag{7.1}$$

where Y is the charge of the shell, k is the harmonic force constant ($\mathrm{eV\,\AA^{-2}}$), ϵ_0 is the permittivity of free space, and α is the polarisability. However, in this body of work we have opted for the more modern expression, which describes the relationship of the core and shell through the harmonic spring equation

$$V^{ij}_{\text{core-shell}}(r) = \frac{1}{2}k_2 r_{ij}^2 + \frac{1}{24}k_4 r_{ij}^4 \tag{7.2}$$

where k_2 and k_4 are the spring constants, r_{ij} is the distance between the core and the shell.

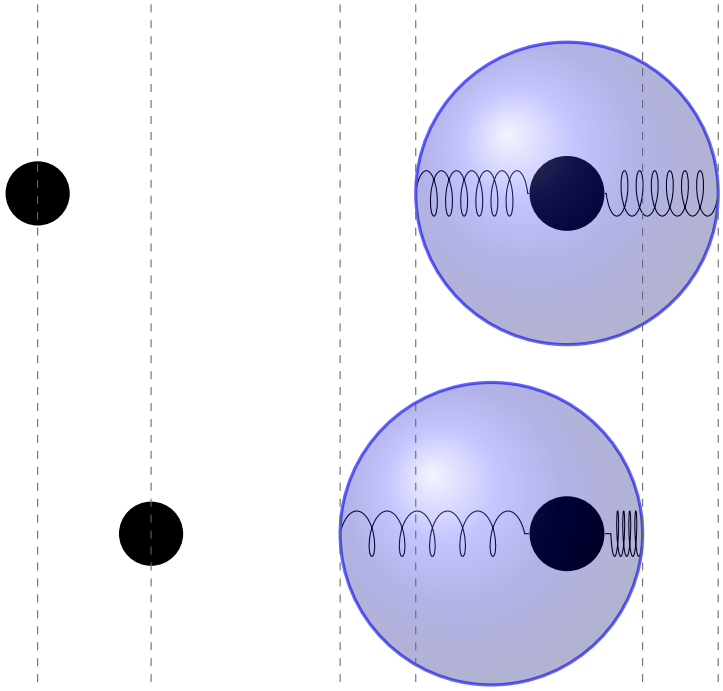

Figure 7.1: A schematic of the shell model. Where the black circles represent positive charges and the blue circle depicts the massless shell, with negative charge. The two images represent the response of the shell-core spring to an external body.

7.4 Methodology

The interatomic potential chosen for the force field were the two-body Buckingham potential, to govern the coulomb forces between atoms, the harmonic potential to describe the covalent characteristics of the nitrogen and oxygen atoms (which requires a cut off radius). The three-body potential to govern the angle and interactions of the O−N−O bond. And finally the shell potential will will be adapted for the O_{core}−O_{shell} interactive. The starting parameters for the fitting of the potentials was taken from Hammond *et al.* [26], apart from the shell model which was adapted from [115].

The fitting was performed using the *sum of squares* (F) equation, which is defined as

$$F = \sum_{i=1}^{N_{obs}} w_i (f_{obs,i} - f_{calc,i})^2 \tag{7.3}$$

where w is a weighting factor, and f_{obs} and f_{calc} are the observed and calculated quantities, respectively. The BFGS algorithm [54] was used to minimise F.

Many potentials are infinite and so it is important to define a cutoff function for the potentials. There are two main reasons to have a cutoff radius r_{max}

1 Save computational cost. The number of pair interactions grows as N^2n

2 Periodic boundary conditions. We do not want an atom interacting with itself.

Weighting factors were chosen to normalise the magnitude of the observables, with these final values slightly altered further to represent uncertainties in the given observable (for example the positioning of the atoms was given more weight then the elastic constants). The fitting process was iterative, fitting one potential constant at a time.

7.5 Results and discussion

7.5.1 Force field testing

The fitted force field for $Ba_xSr_{1-x}(NO_3)_2$ can be found in table 7.1. The developed force field in this study has been used for static calculations of pure barium and strontium nitrate, as well as for preliminary defect calculations using a $2 \times 2 \times 2$ supercell (similar to that performed in section 6.3). The lattice parameters for $Ba(NO_3)_2$ and $Sr(NO_3)_2$ nitrate were calculated to be 8.11 and 7.73 Å which are within 1 % of the observable parameters used for the fitting. The point defect calculation was performed with a Sr defect in the centre of barium nitrate supercell and the elastic response of the defect was consistent to the findings within chapter 6. Unfortunately, it has not been possible to perform large scale molecular dynamics calculations with the potential within this study.

Table 7.1: Fitted interatomic potentials for $Ba_xSr_{1-x}(NO_3)_2$. Where M = Ba, Sr.

Buckingham potential	A (eV)	rho (Å)	C (eV Å^6)
$Ba_{core}-O_{shell}$	3566.14	0.288	0
$Sr_{core}-O_{shell}$	4982.74	0.269	0
$N_{core}-O_{shell}$	5042.82	0.113	0
$O_{shell}-O_{shell}$	35186.62	0.197	24
Harmonic potential	**k (eV Å^{-2})**	**r_0 (Å)**	
$N_{core}-O_{shell}$	50.00	1.24	
Three-body potential	**k_3 (eV)**	**θ_0 (°)**	
$O_{shell}-N_{core}-O_{shell}$	14.582	120.0	
Ionic charges	**Core charge (eV)**	**Shell charge (eV)**	
M_{core}	2	n/a	
N_{core}	0.6392	n/a	
O_{core}	0.91	-1.45	
Shell potential	**k_2 (eV Å^{-2})**	**k_4 (eV Å^{-4})**	
$O_{core}-O_{shell}$	28.4	3932	

7.6 Conclusions

In this chapter an interatomic force field was derived for the solid solution mix of $Ba_xSr_{1-x}(NO_3)_2$. This was developed by fitting the parameters for the Buckingham potential, Harmonic potential, three-body potential, as well as the shell potential to *observables* calculated using *ab initio* DFT (calculated in previous chapters of this thesis). A description of the shell model potential was also presented, along with the overall fitting procedure for the force field.

Chapter 8

Summary and outlook

8.1 Chapter summary

In depth discussions related to the individual studies have been provided in each previous chapter. This chapter aims to bring all of the findings together in a summary and relates them back to the original aims of the thesis. General reflections, limitations, and strengths of the thesis are also discussed, along with suggestions for future research.

8.2 Thesis aims and summary

Before nuclear waste can be safely transported from temporary to long-term storage, there are various issues that must first be properly investigated and understood. One such issue is the formation of a barium-strontium nitrate crystal in the highly active liquor (HAL), also referred to as 'waste sludge'. This nitrate complex may settle within the Highly Active Storage Tanks at Sellafield and has the potential to lead to corrosion hotspots. This may subsequently result in nuclear waste leakages. It is evident that a thorough understanding of the properties of this nitrate is needed, to ensure safe and effective handling of this

material for long-term storage. Whilst experimental methods have been previously used to investigate the properties of barium and strontium nitrates, and the barium-strontium nitrate complex, they are unable to investigate the properties occurring on an atomic scale. As such, the aims of this thesis were to:

1. Synthesize existing experimental research that has investigated the properties of barium and strontium nitrate
2. Investigate the fundamental properties of barium and strontium nitrate using computational methods
3. determine the reliability of computational methods through comparison to existing experimental results
4. Investigate cationic substitutional point defects within barium nitrate
5. Investigate the structural and thermodynamic properties of the mixed barium-strontium nitrate complex
6. Use the above findings to develop a new force field of interatomic potentials.

To address these aims, a literature review, ab initio DFT calculations were performed, and a new interatomic potential was fitted. In chapter 2, an overview of the scientific and technological background was given, to set the context for studying the materials in question and highlight the origin of the interest in these materials. In chapter 3, a literature review was conducted to explore what has been done experimentally, and dissect the limitations of experimental methods. Additionally, *ab initio* calculations that have been performed on similar materials were reviewed, to gather an understanding of the methodologies used for performing DFT. In chapter 4, the theory behind the computational methods was given and discussed. In chapter 5 the structural and elastic properties for $Ba(NO_3)_2$, $Sr(NO_3)_2$, and $Ca(NO_3)_2$ were calculated through *ab initio* methods, with in

depth study of different functionals and also different methodologies available for calculating the elastic properties. Benchmark calculations were also performed to develop a greater understanding of the accuracy and precision of the methods and to compare the reliability and quality of the different results. In chapter 6, following on from the groundwork laid out in preceding chapter, the mechanical and thermodynamic properties of $Ba_xSr_{1-x}(NO_3)_2$ were calculated. Firstly, point defects within the $Ba(NO_3)_2$ crystal were examined and then lattice parameters as a functional of strontium-barium concentration were calculated, drawing comparison with the literature. Finally a $T-x$ phase diagram was calculated and examined. Each of the above aims are addressed in turn, below. Finally, in chapter 7 an interatomic force field was fitted and developed to enable large scale static calculations and the possibility of molecular dynamic calculations in future work.

8.3 Thesis reflections and limitations

Here I will discuss the limitations and possible extensions of this work and include the overall picture and relevance as well.

8.3.1 Supercells

One unfortunate limitation of this body of work is the size of the supercells used for the $Ba_xSr_{1-x}(NO_3)_2$ calculations. An obvious improvement would be to incorporate larger supercells (such as $3 \times 3 \times 3$). This would provide a greater number of concentrations (x) providing greater detail for the mixing energy and therefore thermodynamics. A large supercell would also introduce multiple options for cationic substitutions for the same value of x. Which particular site the substitution should occur is a non-trivial issue and there are a number of techniques that have been developed to solve this.

Two of the main methods are special quasirandom structures (SQS) and coherent potential approximation (CPA) [111]. Many papers have cited special quasirandom structures (SQS) as a successful way of determining the mix of two cations within an alloy. One particular way of determining the position of the mixed atoms is to use the Alloy Theoretic Automated Toolkit (ATAT). This approach has been used for solid solutions as well.

There also exist variations such as the Quasirandom Structure method (QRS) which searching various arrangements to find structures in which the frequencies of the cation-cation, AB pairs, deviate as little as possible from the product [116].

8.4 Future work

8.4.1 Calculations of phase diagrams

Another way of determining phase diagrams is through using the CALPHAD (CALculation of PHase Diagrams) method, [117], which relies on Gibbs energy database which typically consists of experimental work. This is an approach, which typically combines experimental information on phase equilibria and creates a mathematical model, with adjustable parameters, to describe the thermodynamic properties of each phase. There have been numerous studies that compare DFT results alongside CALPHAD [118; 119], the results from this body of work could be used to help improve or verify CALPHAD calculations, which may in turn provide a greater understanding of the solid solution.

8.4.2 Interatomic potentials for radioactive environments

Chen *et al.* developed further modifications to the shell model to accommodate radiation effects in $BaTiO_3$ [120]. Such effects caused by radiation bombardment on the system of interest may force unusual particle interactions. Using the

anharmonic spring expression

$$V^{ij}_{\text{core-shell}}(r) = \frac{1}{2}k_2 r_{ij}^2 + \frac{1}{24}k_4 r_{ij}^4 \tag{8.1}$$

they defined the distance-dependent spring constant k_2 as

$$k_2 = 0.99 + 1000 r_{ij}^5 \tag{8.2}$$

this prevents unstable dynamics by inhibiting unphysical separation of the core and the shell. For shorter separations ($< 0.1\,\text{Å}$), the core-shell interaction is considered harmonic.

8.4.3 Breathing shell model

One drawback from the use of the shell model is that it violates the Cauchy relationship, which states that (for cubic crystals) the elastic constants C_{12} and C_{44} are equal. It has been shown in previous sections of this work that the nitrates of interest violate this relationship and the C_{12} is less than C_{44}. A breathing shell model has been introduced to help overcome this [121]. The breathing shell model has been compared to the shell model for calculating defect energies for MgO [122] with specific interest in the large Cauchy violation found in MgO. Their results were insensitive to the choice of model, stating only small changes in the defects energies were found, as long as the model reproduces the dielectric behaviour correctly.

The main drawback with the breathing shell model is that it is notoriously difficult to derive and requires significantly more computational power. Therefore, it is only recommended if a specific scenario arises which the shell model is known to not work well.

References

[1] World Nuclear Transport Institute, "Nuclear fuel cycle." https://www.wnti.co.uk/media/1171/nuclear-fuel-cycle.png. [Online; accessed 20-Oct-2018]. vi, 7

[2] P. Colgan, D. Pollard, C. Hone, C. McMahon, and A. McGarry, *Report of the RPII Visit to BNFL Sellafield*. Radiological Protection Institute of Ireland, 2005. 8

[3] Office for Nuclear Regulation, *Project Assessment Report ONR-SDFW-PAR-17-002 - HAL Stocks*. Office for Nuclear Regulation, 2017. 8, 9, 10

[4] F. J. Turvey and C. Hone, "Storage of liquid high level radioactive waste at sellafield," vol. RPII - 00, p. 19, 2000. vi, 8

[5] M. J. Edmondson, L. J. Maxwell, and T. R. Ward, "A methodology for post operational clean out of a highly active facility including solids behaviour - 12386," WM Symposia, 1628 E. Southern Avenue, Suite 9-332, Tempe, AZ 85282 (United States), 2012. 9, 10

[6] A. Dobson and C. Phillips, "High level waste processing in the UK - hard won experience that can benefit US nuclear cleanup work," *Waste Management*, vol. 6, 2006. vi, 10, 11

[7] Sellafield Ltd., "Final Report to ONR on the application of the ENSREG Stress Tests to the Sellafield Site," no. April 2012, pp. 1–65, 2012. 11

[8] M. T. Harrison, "Vitrification of high level waste in the UK," *Procedia Materials Science*, vol. 7, pp. 10–15, 2014. 12

[9] B. Dunnett, T. Ward, R. Roberts, and J. Cheesewright, "Physical properties of highly active liquor containing molybdate solids," *Procedia Chemistry*, vol. 21, pp. 24–31, 2016. 12

[10] H. Nowotny and G. Heger, "Structure refinement of strontium nitrate, $Sr(NO_3)_2$, and barium nitrate, $Ba(NO_3)_2$," *Acta Crystallographica Section C*, vol. 39, pp. 952–956, Aug 1983. xi, 15, 16, 18, 47, 57, 58

[11] R. Birnstock, "Erneute strukturbestimmung von bariumnitrat mit neutronenbeugung," *Zeitschrift fur Kristallographie*, vol. 124, pp. 310–334, 1967. xi, 15, 57

[12] L. Vegard and L. Bilberg, "Structure of nitrates of divalent metals," *Skrifter utgitt av det Norske Videnskaps-Akademi i Oslo 1: Matematisk-Naturvidenskapelig Klasse*, vol. 31, no. 12, pp. 1–22, 1931. xi, 15, 16, 47, 57

[13] L. Vegard, "Die struktur der isomorphen. gruppe $Pb(NO_3)_2$, $Ba(NO_3)_2$, $Sr(NO_3)_2$, $Ca(NO_3)_2$," *Zeitschrift für Physik A Hadrons and Nuclei*, vol. 9, no. 1, pp. 395–410, 1922. xi, 15, 16, 57

[14] V. Trounov, E. Tserkovnaya, V. Gurin, M. Korsukova, L. Derkachenko, and S. Nikanorov, "Effect of centrifugation on the crystal structure of barium nitrate," *Technical Physics Letters*, vol. 28, no. 4, pp. 351–353, 2002. xi, 15, 57

[15] G. Lutz, "Strukturuntersuchung von $Ba(NO_3)_2$ mit neutronenbeugung," *Zeitschrift fur Kristallographie*, vol. 114, p. 232 244, 1960. xi, 15, 57

[16] B. El-Bali and M. Bolte, "$Sr(NO_3)_2$ at 173 K," *Acta Cryst*, vol. 54, 1998. xi, 16, 57

[17] F. Michard, F. Plicque, and A. Zarembowitch, "Elastic and thermoelastic properties of lead, barium, and strontium nitrates," *Journal of Applied Physics*, vol. 44, no. 2, pp. 572–576, 2003. vi, 16, 17, 57, 64, 78

[18] W. Chen, D. Liu, C. Zhang, L. Wu, and A. Xie, "Larger $Ba(NO_3)_2/Sr(NO_3)_2$ crystal growth and solubility determination," *Materials Research Bulletin*, vol. 39, pp. 309–316, Feb. 2004. vi, vii, 15, 18, 21, 22

[19] L. J. Wu, W. C. Chen, C. R. Li, A. Y. Xie, Y. C. Liu, and J. K. Liang, "Crystallization of $Ba_xSr_{1-x}(NO_3)_2$ solid solutions from aqueous solutions and the influence of Ba^{2+} ion on $Sr(NO_3)_2$ crystals," *Materials research bulletin*, vol. 35, no. 3, pp. 2145–2156, 2000. vi, 17, 19, 21

[20] N. E. Mishina, B. Y. Zilberman, A. A. Lumpov, T. I. Koltsova, E. A. Puzikov, and D. Y. Gavshina, "Coprecipitation of barium and strontium nitrates in the course of crystallization from nitric acid solutions and simulated high-level PUREX process raffinate," *Radiochemistry*, vol. 57, pp. 504–512, Oct. 2015. vi, 18, 21, 23

[21] K. Hussain, P. Kumar, A. Saritha, M. Murthy, and V. Ganesan, "Nanoscopic investigations on the surface topography, defect-substructure, dislocations and micromorphology of surfaces of $Ba_xSr_{1-x}(NO_3)_2$ mixed crystals," *Journal of Crystal Growth*, vol. 391, pp. 7–12, 2014. vi, 18, 20

[22] K. Hussain, K. PM, and S. A, "Thermal properties of $Ba_xSr_{1-x}(NO_3)_2$ mixed crystals," *International journal of innovative research in science, engineering and technology*, vol. 4, no. 11, 2015. 19, 21

[23] N. E. Mishina, A. A. Akhmatov, B. Y. Zilberman, A. Y. Shadrin, and E. I. Solyarskaya, "Solubility and coprecipitation of barium and strontium nitrates in HNO_3 solutions and multicomponent systems," *Radiochemistry*, vol. 52, pp. 523–529, Oct. 2010. xi, 22, 23

[24] N. E. Mishina, B. Y. Zilberman, A. A. Lumpov, T. I. Koltsova, E. A. Puzikov, and D. V. Ryabkov, "Nitric acid adduct formation during crystallization of barium and strontium nitrates and their co-precipitation from nitric acid media," *Journal of Radioanalytical and Nuclear Chemistry*, vol. 304, no. 1, pp. 387–393, 2015. vii, 23, 24

[25] C. Rao, R. Singh, and S. Hasan, "Cohesive and anharmonic properties of some fluorite structure nitrates," *physica status solidi (b)*, vol. 169, no. 1, pp. 51–55, 1992. 23

[26] R. B. Hammond, M. J. Orley, K. J. Roberts, R. A. Jackson, and M. J. Quayle, "An examination of the influence of divalent cationic dopants on the bulk and surface properties of $Ba(NO_3)_2$ associated with crystallization," *Crystal Growth and Design*, vol. 9, no. 6, pp. 2588–2594, 2009. 24, 25, 111

[27] K. Mort, P. Wilde, and R. Jackson, "Computer modelling of ammonium nitrate: I. development of potentials and calculation of lattice properties," *Journal of Physics: Condensed Matter*, vol. 11, no. 20, p. 3967, 1999. 24

[28] I. Faux and A. Lidiard, "The volumes of formation of schottky defects in ionic crystals," *Zeitschrift für Naturforschung A*, vol. 26, no. 1, pp. 62–68, 1971. 24, 109

[29] N. De Leeuw and S. Parker, "Molecular-dynamics simulation of MgO surfaces in liquid water using a shell-model potential for water," *Physical Review B*, vol. 58, no. 20, p. 13901, 1998. 25

[30] Y. N. Zhuravlev and D. Korabel'nikov, "Elastic and photoelastic properties of $M(NO3)_2$, MO (M= Mg, Ca, Sr, Ba)," *Russian Physics Journal*, vol. 60, no. 1, pp. 149–156, 2017. 25

[31] R. Dovesi, V. Saunders, C. Roetti, R. Orlando, C. Zicovich-Wilson, F. Pascale, B. Civalleri, K. Doll, N. Harrison, I. Bush, *et al.*, "Crystal14 user's manual; university of torino: Torino, italy, 2014," *There is no corresponding record for this reference*, 2014. 25

[32] S. J. Clark, M. D. Segall, C. J. Pickard, P. J. Hasnip, M. I. Probert, K. Refson, and M. C. Payne, "First principles methods using CASTEP," *Zeitschrift für Kristallographie*, vol. 220, no. 5/6/2005, pp. 567–570, 2005. 26

[33] J. D. Gale and A. L. Rohl, "The general utility lattice program (GULP)," *Molecular Simulation*, vol. 29, no. 5, pp. 291–341, 2003. 26

[34] M. Born and R. Oppenheimer, "Zur quantentheorie der molekeln," *Annalen der Physik*, vol. 389, no. 20, pp. 457–484, 1927. 28

[35] P. Hohenberg and W. Kohn, "Inhomogeneous electron gas," *Physical review*, vol. 136, no. 3B, p. B864, 1964. 30

[36] R. M. Martin, *Electronic structure: basic theory and practical methods*. Cambridge university press, 2004. 30

[37] W. Kohn and L. J. Sham, "Self-consistent equations including exchange and correlation effects," *Physical Review*, vol. 140, no. 4A, p. A1133, 1965. 31

[38] R. O. Jones and O. Gunnarsson, "The density functional formalism, its applications and prospects," *Reviews of Modern Physics*, vol. 61, no. 3, p. 689, 1989. 32, 55

[39] A. Marini, G. Onida, and R. Del Sole, "Plane-wave DFT-LDA calculation of the electronic structure and absorption spectrum of copper," *Physical Review B*, vol. 64, no. 19, p. 195125, 2001. 32

[40] J. P. Perdew and Y. Wang, "Pair-distribution function and its coupling-constant average for the spin-polarized electron gas," *Physical Review B*, vol. 46, no. 20, p. 12947, 1992. 33

[41] J. P. Perdew, K. Burke, and M. Ernzerhof, "Generalized gradient approximation made simple," *Physical review letters*, vol. 77, no. 18, p. 3865, 1996. 33

[42] Z. Wu and R. E. Cohen, "More accurate generalized gradient approximation for solids," *Physical Review B*, vol. 73, no. 23, p. 235116, 2006. 33

[43] Gang65, "Brillouin zone (for physics)." https://commons.wikimedia.org/wiki/File:Brillouin_zone.svg, 2007. [Online; accessed 20-Oct-2018]. vii, 34

[44] H. J. Monkhorst and J. D. Pack, "Special points for brillouin-zone integrations," *Physical Review B*, vol. 13, no. 12, p. 5188, 1976. 35

[45] W. Quester, "Sketch pseudopotentials." https://en.wikipedia.org/wiki/File:Sketch_Pseudopotentials.png, 2006. [Online; accessed 20-Oct-2018]. vii, 35

[46] D. Vanderbilt, "Soft self-consistent pseudopotentials in a generalized eigenvalue formalism," *Physical Review B*, vol. 41, no. 11, p. 7892, 1990. 35

[47] P. E. Blöchl, "Projector augmented-wave method," *Physical review B*, vol. 50, no. 24, p. 17953, 1994. 36

[48] G. Kresse and D. Joubert, "From ultrasoft pseudopotentials to the projector augmented-wave method," *Physical Review B*, vol. 59, no. 3, p. 1758, 1999. 36

[49] K. Lejaeghere, G. Bihlmayer, T. Björkman, P. Blaha, S. Blügel, V. Blum, D. Caliste, I. E. Castelli, S. J. Clark, A. Dal Corso, *et al.*, "Reproducibility in density functional theory calculations of solids," *Science*, vol. 351, no. 6280, p. aad3000, 2016. 36

[50] C.-K. Skylaris, "A benchmark for materials simulation," *Science*, vol. 351, no. 6280, pp. 1394–1395, 2016. 36

[51] R. T. Cygan, J.-J. Liang, and A. G. Kalinichev, "Molecular models of hydroxide, oxyhydroxide, and clay phases and the development of a general force field," *The Journal of Physical Chemistry B*, vol. 108, no. 4, pp. 1255–1266, 2004. 37

[52] R. Jackson, P. Meenan, G. D. Price, K. Roberts, G. Telfer, and P. Wilde, "Deriving empirical potentials for molecular ionic materials," *Mineralogical Magazine*, vol. 59, no. 397, pp. 617–622, 1995. 39

[53] R. Lynden-Bell, M. Ferrario, I. McDonald, and E. Salje, "A molecular dynamics study of orientational disordering in crystalline sodium nitrate," *Journal of Physics: Condensed Matter*, vol. 1, no. 37, p. 6523, 1989. 40

[54] J. D. Head and M. C. Zerner, "A broyden-fletcher-goldfarb-shanno optimization procedure for molecular geometries," *Chemical physics letters*, vol. 122, no. 3, pp. 264–270, 1985. 41, 52, 112

[55] T. S. Bush, J. D. Gale, C. R. A. Catlow, and P. D. Battle, "Self-consistent interatomic potentials for the simulation of binary and ternary oxides," *Journal of Materials Chemistry*, vol. 4, no. 6, pp. 831–837, 1994. xi, 42

[56] S. M. Woodley, P. D. Battle, J. D. Gale, C. Richard, and A. Catlow, "The prediction of inorganic crystal structures using a genetic algorithm and energy minimisation," *Physical Chemistry Chemical Physics*, vol. 1, no. 10, pp. 2535–2542, 1999. 42

[57] M. Islam and L. Winch, "Defect chemistry and oxygen diffusion in the $HgBa_2Ca_2Cu_3O_8^+\delta$ superconductor: A computer simulation study," *Physical Review B*, vol. 52, no. 14, p. 10510, 1995. 42

[58] G. Lewis and C. Catlow, "Potential models for ionic oxides," *Journal of Physics C: Solid State Physics*, vol. 18, no. 6, p. 1149, 1985. 42

[59] D. Marx and J. Hutter, "Ab initio molecular dynamics," *Parallel computing*, vol. 309, no. 309, p. 327, 2009. 43

[60] "National chemical database service." https://icsd.fiz-karlsruhe.de. [Online; accessed 12-July-2018]. 46

[61] M. Probert and M. Payne, "Improving the convergence of defect calculations in supercells: An ab initio study of the neutral silicon vacancy," *Physical Review B*, vol. 67, no. 7, p. 075204, 2003. 47, 48

[62] H. Nowotny and G. Heger, "Structure refinement of lead nitrate," *Acta Crystallographica Section C: Crystal Structure Communications*, vol. 42, no. 2, pp. 133–135, 1986. 47, 57

[63] J. A. Kaduk, "Chemical accuracy and precision in structural refinements from powder diffraction data," *Adv. X–Ray Anal*, vol. 40, pp. 352–370, 1996. 51, 55

[64] F. H. Herbstein, "How precise are measurements of unit-cell dimensions from single crystals?," *Acta Crystallographica Section B: Structural Science*, vol. 56, no. 4, pp. 547–557, 2000. 51, 55

[65] F. Michard, F. Plicque, and A. Zarembowitch, "Elastic and thermoelastic properties of lead, barium, and strontium nitrates," *Journal of Applied Physics*, vol. 44, no. 2, pp. 572–576, 1973. xi, xii, 54, 61, 82

[66] D. C. Green, U. Englich, and K. Ruhlandt-Senge, "Calcium, strontium, and barium acetylides - new evidence for bending in the structures of heavy alkaline earth metal derivatives," *Angewandte Chemie International Edition*, vol. 38, no. 3, pp. 354–357, 1999. 54

[67] H. Hesske, A. Urakawa, and A. Baiker, "Ab initio assignments of FIR, MIR, and raman bands of bulk ba species relevant in NO_x storage-reduction," *The Journal of Physical Chemistry C*, vol. 113, no. 28, pp. 12286–12292, 2009. 57

[68] B. Ribar and V. Divjaković, "A new crystal structure study of $Ca(NO_3)_2 \cdot 4\,H_2O$," *Acta Crystallographica Section B*, vol. 29, no. 7, pp. 1546–1548, 1973. 57

[69] F. Murnaghan, "The compressibility of media under extreme pressures," *Proceedings of the National Academy of Sciences of the United States of America*, vol. 30, no. 9, pp. 244–247, 1944. 56

[70] P. Vinet, J. H. Rose, J. Ferrante, and J. R. Smith, "Universal features of the equation of state of solids," *Journal of Physics: Condensed Matter*, vol. 1, no. 11, p. 1941, 1989. 56

[71] J.-P. Poirier and A. Tarantola, "A logarithmic equation of state," *Physics of the Earth and Planetary Interiors*, vol. 109, no. 1, pp. 1–8, 1998. 56

[72] R. E. Cohen, O. Gülseren, and R. J. Hemley, "Accuracy of equation-of-state formulations," *American Mineralogist*, vol. 85, no. 2, pp. 338–344, 2000. 56

[73] F. Birch, "Finite elastic strain of cubic crystals," *Physical Review*, vol. 71, no. 11, p. 809, 1947. 59

[74] R. Gaudoin and W. Foulkes, "Ab initio calculations of bulk moduli and comparison with experiment," *Physical Review B*, vol. 66, no. 5, p. 052104, 2002. 60, 68

[75] E. Ziambaras and E. Schröder, "Theory for structure and bulk modulus determination," *Physical Review B*, vol. 68, no. 6, p. 064112, 2003. 60

[76] V. Tyuterev and N. Vast, "Murnaghan's equation of state for the electronic ground state energy," *Computational materials science*, vol. 38, no. 2, pp. 350–353, 2006. 60

[77] D. Gerlich, M. Wolf, and S. Haussühl, "Pressure derivatives of the elastic moduli of strontium, barium and lead nitrate," *Journal of Physics and Chemistry of Solids*, vol. 39, no. 10, pp. 1089–1093, 1978. xi, xii, 61, 76, 78, 82

[78] Y. Le Page and P. Saxe, "Symmetry-general least-squares extraction of elastic coefficients from ab initio total energy calculations," *Physical Review B*, vol. 63, no. 17, p. 174103, 2001. 63

[79] V. Levitin, *Interatomic bonding in solids: fundamentals, simulation, applications*. John Wiley & Sons, 2013. 68, 73, 75

[80] M. J. Mehl, "Pressure dependence of the elastic moduli in aluminum-rich Al−Li compounds," *Physical Review B*, vol. 47, no. 5, p. 2493, 1993. 68

[81] P. Lazar, *Ab initio modelling of mechanical and elastic properties of solids*. University of Vienna, 2006. 75

[82] G. Sin'Ko and N. Smirnov, "Ab initio calculations of elastic constants and thermodynamic properties of bcc, fcc, and hcp Al crystals under pressure," *Journal of Physics: Condensed Matter*, vol. 14, no. 29, p. 6989, 2002. 75

[83] Y. Sun and E. Kaxiras, "Slip energy barriers in aluminium and implications for ductile-brittle behaviour," *Philosophical Magazine A*, vol. 75, no. 4, pp. 1117–1127, 1997. 75

[84] M. J. Mehl, B. M. Klein, and D. A. Papaconstantopoulos, *First principles calculations of elastic properties of metals*, vol. 1. Wiley, London, 1994. 75

[85] P. M. Sutton, "The variation of the elastic constants of crystalline aluminum with temperature between 63 K and 773 K," *Physical Review*, vol. 91, no. 4, p. 816, 1953. 75

[86] C. Kittel, "Introduction to solid state physics 8th ed, (2005)," 2005. 75, 83

[87] H. Yao, L. Ouyang, and W.-Y. Ching, "Ab initio calculation of elastic constants of ceramic crystals," *Journal of the American Ceramic Society*, vol. 90, no. 10, pp. 3194–3204, 2007. 75

[88] A. R. Oganov and P. I. Dorogokupets, "All-electron and pseudopotential study of MgO: equation of state, anharmonicity, and stability," *Physical Review B*, vol. 67, no. 22, p. 224110, 2003. 75

[89] P. Carrez, P. Cordier, *et al.*, "Peierls-nabarro modelling of dislocations in MgO from ambient pressure to 100 GPa," *Modelling and Simulation in Materials Science and Engineering*, vol. 17, no. 3, p. 035010, 2009. 75

[90] B. Karki, L. Stixrude, S. Clark, M. Warren, G. Ackland, and J. Crain, "Structure and elasticity of MgO at high pressure," *American Mineralogist*, vol. 82, no. 1-2, pp. 51–60, 1997. 75

[91] E. Bogardus, "Third-order elastic constants of Ge, MgO, and fused SiO_2," *Journal of Applied Physics*, vol. 36, no. 8, pp. 2504–2513, 1965. 75

[92] M. A. Durand, "The temperature variation of the elastic moduli of NaCl, KCl and MgO," *Physical Review*, vol. 50, no. 5, p. 449, 1936. 75

[93] Z. Chang and E. Graham, "Elastic properties of oxides in the NaCl-structure," *Journal of Physics and Chemistry of Solids*, vol. 38, no. 12, pp. 1355–1362, 1977. 75

[94] R. Mota, S. Costa, P. Pizani, and J. Rino, "Molecular dynamics simulation of the structural and dynamical properties of crystalline BaO," *Physical Review B*, vol. 71, no. 22, p. 224114, 2005. 75

[95] L. Glasser and D. A. Sheppard, "Cohesive energies and enthalpies: Complexities, confusions, and corrections," *Inorganic chemistry*, vol. 55, no. 14, pp. 7103–7110, 2016. 84

[96] D. R. Lide and H. Frederikse, "Handbook of chemistry and physics 78th," 1997. xii, 84, 85

[97] K. Nordlund, "Schematic illustration of some simple point defect types in a monatomic solid." https://commons.wikimedia.org/wiki/File:Defecttypes.png, 1993. [Online; accessed 20-Oct-2018]. viii, 87

[98] C. Freysoldt, B. Grabowski, T. Hickel, J. Neugebauer, G. Kresse, A. Janotti, and C. G. Van de Walle, "First-principles calculations for point defects in solids," *Reviews of Modern Physics*, vol. 86, pp. 253–305, Mar. 2014. 88

[99] C. Freysoldt, J. Neugebauer, and C. Van de Walle, "Fully ab initio finite-size corrections for charged-defect supercell calculations," *Physical Review Letters*, vol. 102, p. 016402, Jan. 2009. 88

[100] C. W. M. Castleton, A. Höglund, and S. Mirbt, "Density functional theory calculations of defect energies using supercells," *Modelling and Simulation in Materials Science and Engineering*, vol. 17, p. 084003, Dec. 2009. 88, 90, 92

[101] L. Li, S. Reich, and J. Robertson, "Defect energies of graphite: Density-functional calculations," *Physical Review B*, vol. 72, p. 184109, Nov. 2005. 88

[102] X. Sun, Z. Wang, and Y. Q. Fu, "Defect-mediated lithium adsorption and diffusion on monolayer molybdenum disulfide," *Scientific reports*, vol. 5, p. 18712, 2015. 88

[103] F. Kröger and H. Vink, "Relations between the concentrations of imperfections in crystalline solids," in *Solid state physics*, vol. 3, pp. 307–435, Elsevier, 1956. 89

[104] C. Castleton and S. Mirbt, "Finite-size scaling as a cure for supercell approximation errors in calculations of neutral native defects in InP," *Physical Review B*, vol. 70, p. 195202, Nov. 2004. 90

[105] N. Hine, K. Frensch, W. Foulkes, and M. Finnis, "Supercell size scaling of density functional theory formation energies of charged defects," *Physical Review B*, vol. 79, p. 024112, Jan. 2009. 90

[106] J. Wang, A. Ma, Z. Li, J. Jiang, J. Feng, and Z. Zou, "Effects of Ba−O codoping on the photocatalytic activities of Ta_3N_5 photocatalyst: a dft study," *RSC Advances*, vol. 4, no. 98, pp. 55615–55621, 2014. 96

[107] M. Choi, F. Oba, and I. Tanaka, "First-principles study of native defects and lanthanum impurities in $NaTaO_3$," *Physical Review B*, vol. 78, no. 1, p. 014115, 2008. 96

[108] M. Ghebouli, B. Ghebouli, A. Bouhemadou, M. Fatmi, and K. Bouamama, "Structural, electronic, optical and thermodynamic properties of $Sr_xCa_{1-x}O$, $Ba_xSr_{1-x}O$ and $Ba_xCa_{1-x}O$ alloys," *Journal of Alloys and Compounds*, vol. 509, no. 5, pp. 1440–1447, 2011. ix, 98, 99, 100, 105

[109] F. E. H. Hassan and H. Akbarzadeh, "First-principles investigation of BN_xP_{1-x}, BN_xAs_{1-x} and BP_xAs_{1-x} ternary alloys," *Materials Science and Engineering: B*, vol. 121, no. 1-2, pp. 170–177, 2005. 99, 100

[110] L. Teles, J. Furthmüller, L. Scolfaro, J. Leite, and F. Bechstedt, "First-principles calculations of the thermodynamic and structural properties of strained $In_xGa_{1-x}N$ and $Al_xGa_{1-x}N$ alloys," *Physical Review B*, vol. 62, no. 4, p. 2475, 2000. 100

[111] L.-Y. Tian, Q.-M. Hu, R. Yang, J. Zhao, B. Johansson, and L. Vitos, "Elastic constants of random solid solutions by SQS and CPA approaches: the case of fcc Ti−Al," *Journal of Physics: Condensed Matter*, vol. 27, no. 31, p. 315702, 2015. 100, 118

[112] M. Labidi, S. Labidi, F. E. H. Hassan, M. Boudjendlia, and R. Bensalem, "Structural, electronic and thermodynamic properties of $Sr_xCd_{1-x}O$: A first-principles study," *Materials Science in Semiconductor Processing*, vol. 16, no. 6, pp. 1853–1858, 2013. 108

[113] S. Tinte, M. Stachiotti, S. Phillpot, M. Sepliarsky, D. Wolf, and R. Migoni, "Ferroelectric properties of $Ba_xSr_{1-x}TiO_3$ solid solutions obtained by molecular dynamics simulation," *Journal of Physics: Condensed Matter*, vol. 16, no. 20, p. 3495, 2004. 110

[114] B. Dick Jr and A. Overhauser, "Theory of the dielectric constants of alkali halide crystals," *Physical Review*, vol. 112, no. 1, p. 90, 1958. 110

[115] M. Sepliarsky, A. Asthagiri, S. Phillpot, M. Stachiotti, and R. Migoni, "Atomic-level simulation of ferroelectricity in oxide materials," *Current Opinion in Solid State and Materials Science*, vol. 9, no. 3, pp. 107–113, 2005. 111

[116] Y. Li, P. M. Kowalski, A. Blanca-Romero, V. Vinograd, and D. Bosbach, "Ab initio calculation of excess properties of $La_{1-x}(Ln,An)_xPO_4$ solid solutions," *Journal of solid state chemistry*, vol. 220, pp. 137–141, 2014. 118

[117] H. Lukas, S. G. Fries, and B. Sundman, *Computational thermodynamics: the Calphad method*. Cambridge university press, 2007. 118

[118] Y. Wang, S. Curtarolo, C. Jiang, R. Arroyave, T. Wang, G. Ceder, L.-Q. Chen, and Z.-K. Liu, "Ab initio lattice stability in comparison with CALPHAD lattice stability," *Calphad*, vol. 28, no. 1, pp. 79–90, 2004. 118

[119] F. Körmann, A. A. H. Breidi, S. L. Dudarev, N. Dupin, G. Ghosh, T. Hickel, P. Korzhavyi, J. A. Muñoz, and I. Ohnuma, "Lambda transitions in materials science: Recent advances in CALPHAD and first-principles modelling," *physica status solidi (b)*, vol. 251, no. 1, pp. 53–80, 2014. 118

[120] Y. Chen, B. Liu, Y. Ma, and Y. Zhou, "Modification of a shell model for the study of the radiation effects in $BaTiO_3$," *Nuclear Instruments and Methods in Physics Research Section B: Beam Interactions with Materials and Atoms*, vol. 267, no. 18, pp. 3090–3093, 2009. 118

[121] U. Schröder, "A new model for lattice dynamics ("breathing shell model")," *Solid State Communications*, vol. 4, no. 7, pp. 347–349, 1966. 119

[122] C. Catlow, I. Faux, and M. Norgett, "Shell and breathing shell model calculations for defect formation energies and volumes in magnesium oxide," *Journal of Physics C: Solid State Physics*, vol. 9, no. 3, p. 419, 1976. 119

Appendix

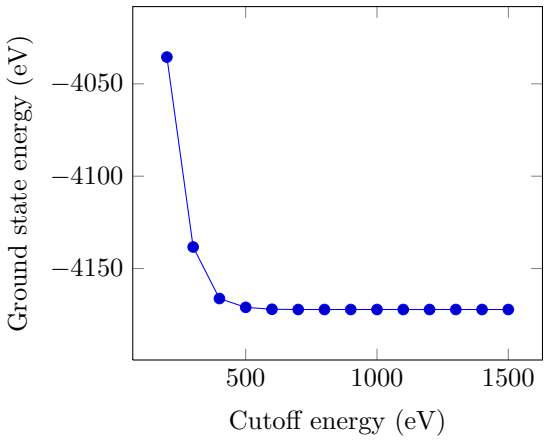

Figure 1: Plane wave cutoff energy as a function of electronic ground state energy for $Ca(NO_3)_2$.

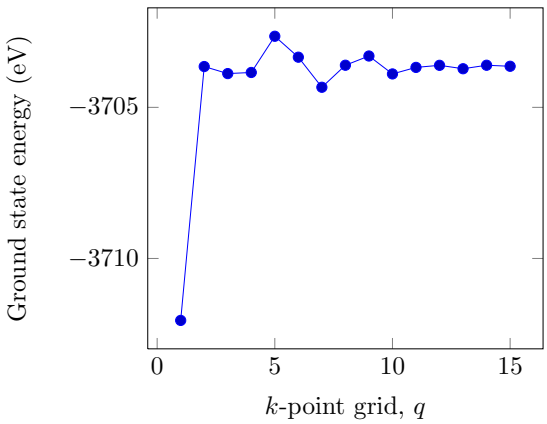

Figure 2: k-point sampling grid for $Ca(NO_3)_2$.

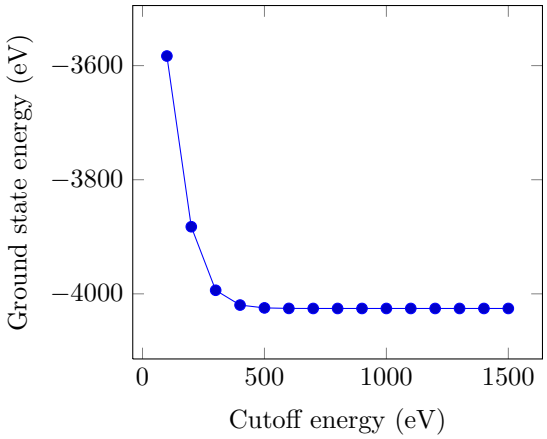

Figure 3: Plane wave cutoff energy as a function of electronic ground state energy for $Ba_xCa_{1-x}(NO_3)_2$.

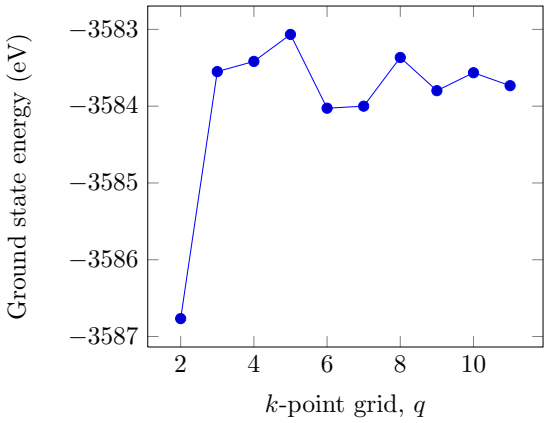

Figure 4: k-point sampling grid for $Ba_xCa_{1-x}(NO_3)_2$.

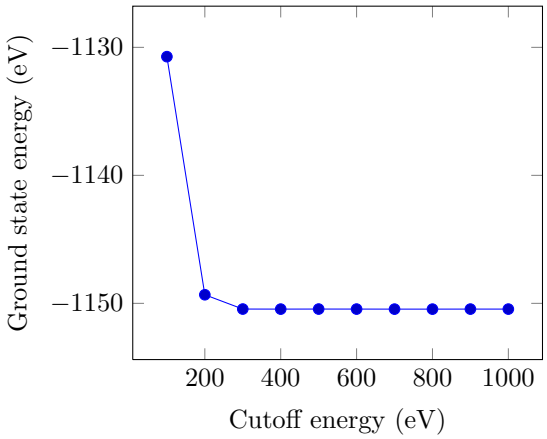

Figure 5: Plane wave cutoff energy as a function of electronic ground state energy for BaO.

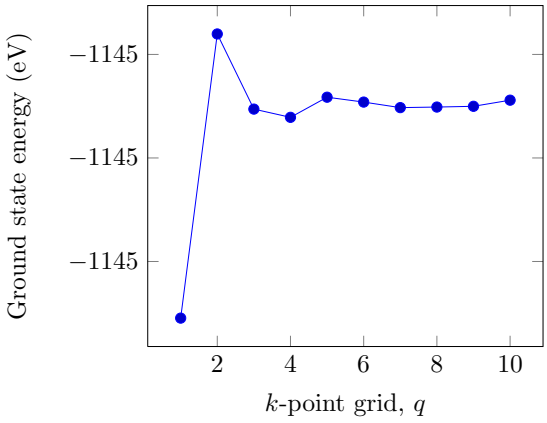

Figure 6: k-point sampling grid for BaO.

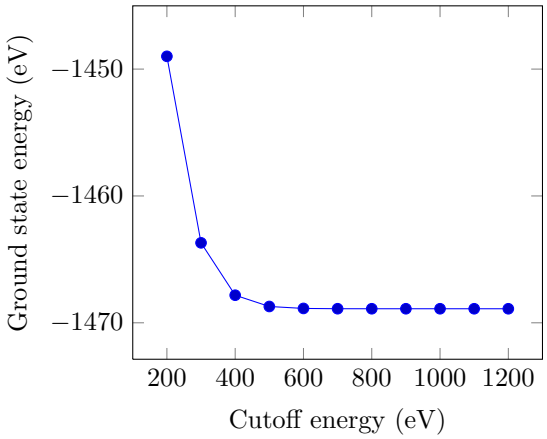

Figure 7: Plane wave cutoff energy as a function of electronic ground state energy for MgO.

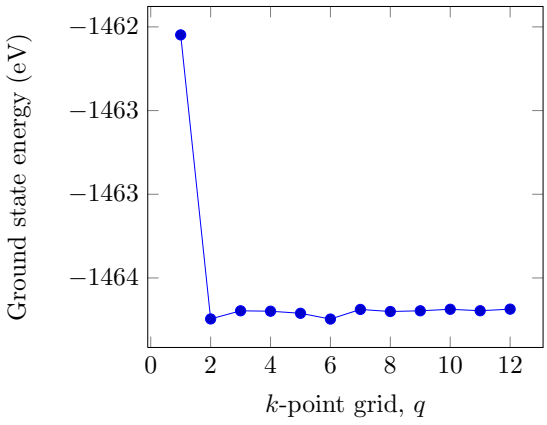

Figure 8: k-point sampling grid for MgO.

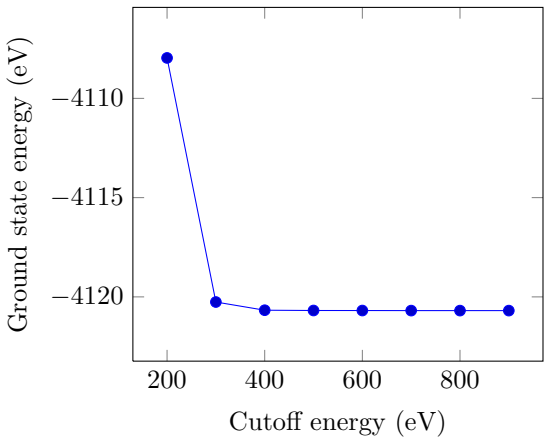

Figure 9: Plane wave cutoff energy as a function of electronic ground state energy for Ni_3Al.

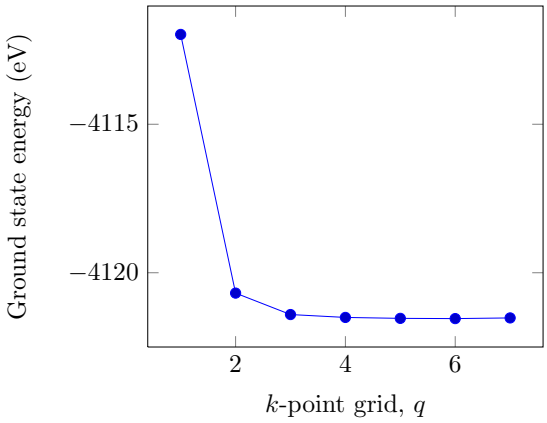

Figure 10: k-point sampling grid for Ni_3Al.

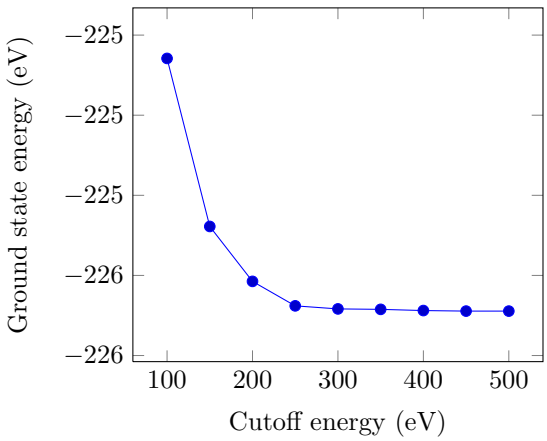

Figure 11: Plane wave cutoff energy as a function of electronic ground state energy for Al.

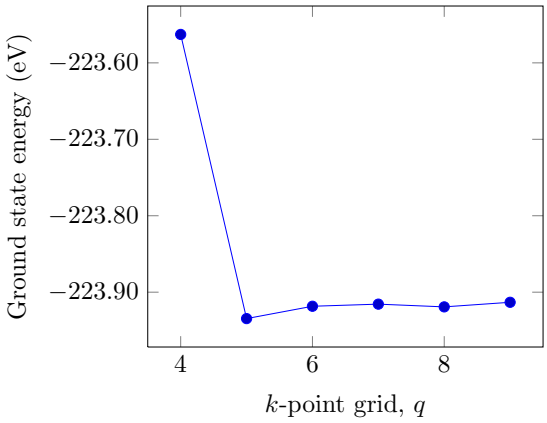

Figure 12: k-point sampling grid for Al.